WARSAW UNIVERSITY OF TECHNOLOGY

FACULTY OF PHYSICS

Ph.D. Thesis

Justyna Cybowska, M.Sc. Eng.

Multiplicity and net-electric charge fluctuations in central Ar+Sc interactions at SPS energies measured in the NA61/SHINE experiment

Field:
Natural Sciences
Discipline:
Physical Sciences

Supervisor:
Prof. Katarzyna Grebieszkow, Ph.D. D.Sc.

Auxiliary Supervisor:
Ph.D. Eng. Maja Maćkowiak-Pawłowska

WARSAW 2023

Acknowledgments

I don't think this thesis was ever created if not for my auxiliary supervisor, dr inż. Maja Maćkowiak-Pawłowska. Her input is impossible to estimate. Not only she shared her valuable knowledge with me, but also was always available for discussions, clearing my doubts, giving ideas, and pushing me forward. I will forever be grateful for that.

There are many people who helped me along the way in many different ways. I want to express my endless gratitude to:

- prof. dr hab. Katarzyna Grebieszkow, my supervisor, for patience and perfectionism,
- prof. dr hab. Marek Gaździcki, the spokesperson of NA61/SHINE, for watching the quality of the analysis, asking the right questions, and providing the right answers,
- dr Evgeny Andronov and Andrey Seryakov, the pioneers of Ar+Sc analysis, for their work on establishing the data selection procedure and being available for discussion every time I needed,
- Daria Prokhorova, for her great work in introducing the *Unfolding* procedure to NA61/SHINE,
- Wojciech Bryliński, for sharing the struggle of grad school.

In addition, I would like to thank all NA61/SHINE members for a warm welcome and for sharing their knowledge and experience with me. All time I spent at CERN has a special place in my heart. It was a pleasure to meet you and work with you.

I also have to mention all my family and friends who continuously asked me "When will you finish your PhD?". I heard it so often that it became a great motivation to finalize this project.
I did it.

For the past self

Streszczenie

(abstract in Polish)

„Fluktuacje krotności cząstek naładowanych oraz netto-ładunku elektrycznego w centralnych zderzeniach Ar+Sc przy energiach SPS mierzone w eksperymencie NA61/SHINE”

Słowa kluczowe: fluktuacje, ładunek elektryczny, punkt krytyczny, zderzenia ciężkich jonów, fizyka, NA61/SHINE, CERN

Analiza fluktuacji ładunku i netto-ładunku elektrycznego jest potężnym narzędziem do badania diagramu silnie oddziałującej materii, stosowanym w wielu eksperymentach na całym świecie, takich jak ALICE (LHC, CERN), STAR (RHIC, BNL) lub NA61/SHINE (SPS, CERN). Niniejsza rozprawa doktorska jest częścią programu NA61/SHINE, który obejmuje badanie przejścia fazowego między gazem hadronowym i plazmą kwarkowo-gluonową oraz poszukiwanie punktu krytycznego między tymi dwoma stanami. Dokonuje się tego poprzez przeprowadzenie dwuwymiarowego skanu, zmieniając rozmiar zderzanego systemu i energię kolizji w celu zmapowania diagramu silnie oddziałującej materii.

W pracy zaprezentowano wyniki dotyczące momentów wyższego rzędu krotności[(a)] cząstek o ładunku dodatnim i ujemnym oraz netto-ładunku w zderzeniach ^{40}Ar+^{45}Sc przy sześciu różnych pędach wiązki, tj. 13A, 19A, 30A, 40A, 75A i 150A GeV/c, o centralności 0 – 1%. Badano następujące intensywne wielkości rozkładów krotności cząstek dodatnich i ujemnych oraz netto-ładunku elektrycznego: κ_2/κ_1, κ_3/κ_2, κ_4/κ_2. Dodatkowo obliczono $\kappa_2/(\kappa_1^+ + \kappa_1^-)$ i κ_3/κ_1 tylko dla rozkładów netto-ładunku elektrycznego. Po raz pierwszy w NA61/SHINE zastosowano procedurę *Unfolding* do naniesienia poprawek w analizie zderzeń ciężkich jonów, w tym przypadku ^{40}Ar+^{45}Sc. Ta pionierska praca otworzyła drzwi do analizy fluktuacji w innych zderzeniach jon-jon badanych w NA61/SHINE: ^{7}Be+^{9}Be, ^{132}Xe+^{139}La i ^{208}Pb+^{208}Pb. Wprowadzone poprawki obejmują różne efekty detektorowe i niedoskonałości procedury rekonstrukcji. W pracy zaprezentowano badane rozkłady krotności i netto-ładunku, zarówno zmierzone, jak i poprawione. Oceniono również niepewności systematyczne i statystyczne.

Wartości wyższego rzędu zostały porównane z odpowiadającymi wynikami dla zderzeń p+p i ^{7}Be+^{9}Be, także zmierzonymi przez NA61/SHINE, oraz z przewidywaniami modelu EPOS. Zaobserwowano efekty, które mogą być sygnałem bliskości punktu krytycznego, takie jak niemonotoniczne zachowanie κ_4/κ_2 dla krotności ładunku ujemnego i κ_3/κ_2, κ_4/κ_2 oraz κ_3/κ_1 dla netto-ładunku. Znaczne niepewności statystyczne sugerują konieczność powtórzenia tego pomiaru w planowanych zderzeniach po 2023 roku.

[(a)] krotność - liczba wyprodukowanych cząstek w pojedynczym zderzeniu (przypadku)

Abstract

(abstract in English)

„Multiplicity and net-electric charge fluctuations in central Ar+Sc interactions at SPS energies measured in the NA61/SHINE experiment”

Keywords: fluctuations, electric charge, critical point, heavy-ion collisions, physics, NA61/SHINE, CERN

The analysis of charge and net-electric charge fluctuations is a powerful tool for studying the diagram of strongly interacting matter, implemented by many experiments worldwide, e.g. ALICE (LHC, CERN), STAR (RHIC, BNL) or NA61/SHINE (SPS, CERN). This thesis is a part of the NA61/SHINE program which contains the study of the onset of deconfinement and the search for the critical point between the hadron gas and the quark-gluon plasma. It is done by performing a two-dimensional scan in the system size and collision energy to map the strongly interacting matter diagram.

This thesis presents results on higher-order moments of positively and negatively charged particle multiplicity[(b)] and net-charge in 0 − 1% central ^{40}Ar+^{45}Sc collisions at six different beam momenta, i.e. 13*A*, 19*A*, 30*A*, 40*A*, 75*A*, and 150*A* GeV/*c*. The following intensive quantities of positively and negatively charged particle multiplicity and net-charge distributions were studied: κ_2/κ_1, κ_3/κ_2, κ_4/κ_2. Additionally $\kappa_2/(\kappa_1^+ + \kappa_1^-)$, and κ_3/κ_1 of only net-charge distributions were calculated. For the first time in NA61/SHINE, the *Unfolding* procedure for corrections was introduced for heavy system collisions, in this case, ^{40}Ar+^{45}Sc. This pioneering work opened the door for the analysis of other ion-ion collisions in NA61/SHINE: ^{7}Be+^{9}Be, ^{132}Xe+^{139}La, and ^{208}Pb+^{208}Pb. Introduced corrections include various detector effects and imperfections of the reconstruction procedure. The studied distributions, both measured and corrected, are presented accordingly. The systematic and statistical uncertainties estimation was also included.

The higher-order quantities were compared to the corresponding results in *p*+*p* and ^{7}Be+^{9}Be collisions, also measured by NA61/SHINE, and to the EPOS model predictions. Some effects which may be a sign of the critical behavior, like the non-monotonic behavior of κ_4/κ_2 of negatively charged particle multiplicity and κ_3/κ_2, κ_4/κ_2, and κ_3/κ_1 of net-charge were observed. Significant statistical uncertainties suggest the need to repeat this measurement in the planned collisions after 2023.

[(b)] multiplicity - number of produced particles per single collision (event)

Contents

Chapter 1

Introduction

1.1 Standard Model

The best description of the matter and its interactions so far is provided by The Standard Model. The Standard Model consists of a set of elementary particles and the description of mechanisms of their interactions [1]. According to the Standard Model, there are three fundamental forces that describe all possible interactions between constituents of matter: **strong force**, **electromagnetic force**, and **weak force**. The **gravity** is another fundamental force, however, no satisfying description of gravity (and its postulated carrier - graviton), which would allow the unification with other fundamental forces, has been proposed so far. Each force originates from different particle charges (color charge, electric charge, weak charge) and has different strength, time, and range of impact. Each fundamental force can be described mathematically as a vector or tensor field and is carried by particles called gauge bosons (see below). At the energy range 10^2 – 10^3 GeV the unification of electromagnetic and weak force into electroweak is observed. Another fundamental process described by the Standard Model is the mass generation and the constituents responsible for it are the Higgs field (a scalar field, thus it can not be considered as a force) and its carrier – the Higgs boson.
The particles considered by the Standard Model as elementary are the following:

- **Quarks**
  Quarks are particles that interact with each other via a strong force. There are six following types of quarks: **up** (u), **down** (d), **strange** (s), **charm** (c), **bottom** (b, sometimes called also "beauty"), **top** (t, sometimes called "true"). They differ in mass, electric charge, isospin, and the quantum number called flavor, however, they all have the same spin number equal to $1/2$ which makes them fermions. Among all quarks, only u and d are stable particles thus the matter in a normal state contains only them. Each quark has its corresponding antiquark with different signs of quantum numbers but the same mass, spin, and isospin. The quarks' properties mentioned above are summarized in Fig. 1.1. Particles made of quarks are called *hadrons*. They are divided into two following subgroups depending on how many quarks or antiquarks they contain: *mesons* – one quark and one antiquark, e.g. π, ρ, K and *baryons* – 3 quarks or antiquarks, e.g. p, n, Σ. In recent twenty years, several particles outside this classification have been observed: exotic hadrons made of four (tetraquarks) and five (pentaquarks) [2, 3, 4]. Apart from quarks and antiquarks, hadrons contain so-called "sea quarks" - virtual, high-energy pairs of quark and antiquark whose existence

is determined by the Heisenberg's uncertainty principle. Annihilation of the "sea" quarks produces a gluon.

- **Leptons**

  Same as quarks, there are six leptons in the Standard Model: **electron** (e), **muon** (μ), **taon** (τ), **electron/muon/taon neutrino** (ν_e, ν_μ, ν_τ). Leptons are fermions (have a spin number equal to $1/2$). They do not undergo strong interactions. Each lepton, similar to quarks, also has its antiparticle. The leptons' properties such as mass, charge, and spin are also listed in Fig. 1.1. Only e is a stable particle. Both μ and τ decay into lighter particles while neutrinos, contrary to the assumptions of the Standard Model, can undergo oscillations and change the lepton quantum number [1].

- **Gauge and Higgs bosons**

  Gauge bosons are vector bosons (have a spin number equal to 1) and are the carriers of the interactions between constituents of matter. There are four gauge bosons carrying the following forces: **gluon** (g) – the strong force, **photon** (γ) – the electromagnetic force, **W bosons** and **Z boson** – weak force. The last piece of the Standart Model is the **Higgs Boson**. It is a scalar boson (has a spin number equal to 0) and it is a product of the excitation of the Higgs field. Through interaction with the Higgs field, elementary particles gain mass via spontaneous symmetry breaking.

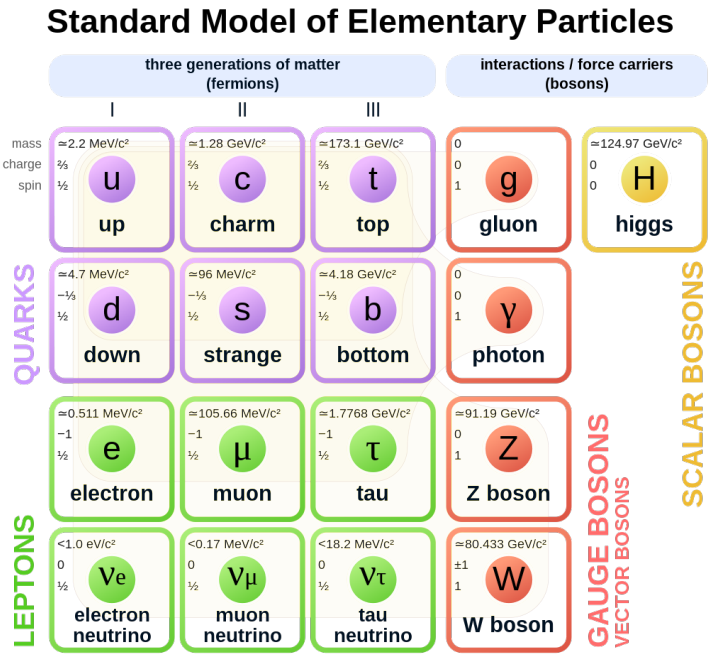

Figure 1.1: Elementary particles in the Standard Model [5], based on Ref. [1].

1.2 Strongly Interacting Matter (SIM)

As stated above, elementary particles can interact with three different fundamental forces. The subject of this dissertation is a behavior of Strongly Interacting Matter (SIM) – particles interact-

ing via the strong force – that is quarks and particles made of quarks – hadrons. The interaction potential between quarks consists of two parts. First, a coulomb-like potential, repulsive, infinitesimal at a distance $\rightarrow \infty$ and goes to ∞ at a distance $\rightarrow 0$. Second, the potential increasing linearly with the distance, responsible for the quark confinement. It means that quarks can not move freely and an attempt to break the confinement by adding energy to the system ends with the creation of another, confined pair of quarks. The example formula of the strong potential for quark-antiquark pair in a nucleon, is shown in Eq. 1.1.

$$V = -\frac{4}{3}\frac{\alpha_s}{r} + kr\,, \tag{1.1}$$

where r – distance between quarks, α_s – strong coupling constant, k – constant of the linear term. The α_s, although called "constant", is changing its value depending on particles' distance and momentum transfer due to the possible creation of virtual particles (particles with short lifetime and high energy resulting from Heisenberg's uncertainty principle) in the quantum vacuum. These virtual particles can cause two phenomena: color screening and antiscreening. The α_s decreases with momentum transfer (increases with distance) [6].

1.2.1 Phase-space diagram of SIM

The SIM, similar to all substances we know, like water, metals, etc., can be observed in different states, depending on various parameters. Thus it can be also described using thermodynamic ensembles like Canonical Ensemble or Grand Canonical Ensemble. The most convenient parameters to the description of SIM phases are temperature (T) and baryon chemical potential (μ_B), which is the energy needed to add or remove one baryon from the system. Qualitative predictions of SIM in $T - \mu_B$ phase space are shown in Fig. 1.2.

There are still more questions than answers regarding the final form of the SIM phase-space diagram. Following Ref. [8], a state called QCD vacuum is present at $T = 0$ and $\mu_B = 0$ and it is the lowest energy state of the strong interaction field. The hadronic matter is situated at approximately $\mu_B \approx 940$ MeV which is the mass of a nucleon. At this point, the hadronic matter density changes discontinuously from $\rho_B = 0$ to $\rho_B \approx 0.15$ fm^{-3}. Starting there, with decreasing μ_B and increasing T, the discontinuity decreases as there is a first-order phase transition between hadron liquid and hadron gas which ends with the critical point at $T \approx 18$ MeV (marked with blue point and letter "M" in Fig. 1.2).
Quark-gluon plasma (QGP), another SIM state, can be produced by increasing the temperature and/or the density of the matter. A more detailed description of QGP, its production and its properties, are described in Sec. 1.3. The mechanism of QGP creation is still the subject of research. Theoretical calculations on multidimensional lattices (Lattice QCD calculations) are most reliable only at vanishing baryon potential. Those calculations indicate that, at $\mu_B = 0$, the transition between the hadron gas and QGP is not a phase transition but a crossover and the temperature of this transition is approximately equal $T \approx 157$ [9, 10]. At $\mu_B \neq 0$ the strict

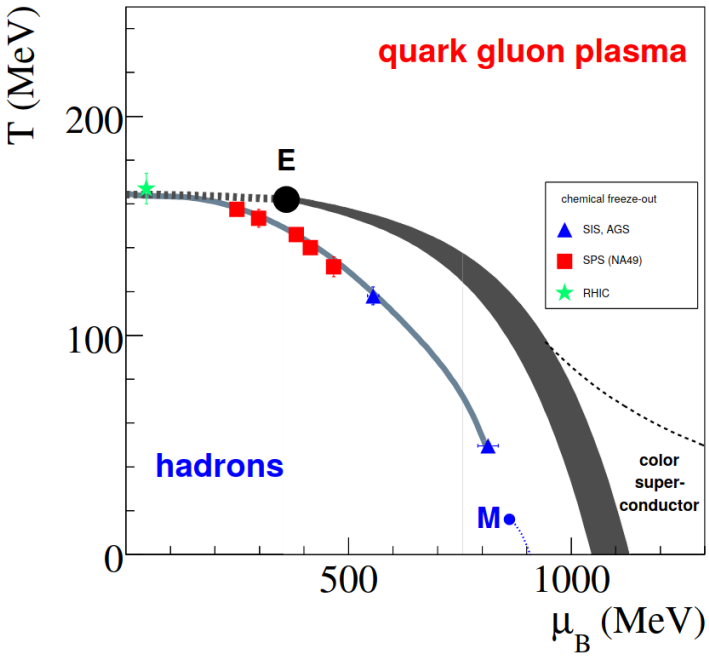

Figure 1.2: T – μ_B phase space diagram of SIM [7].

Lattice QCD calculations are hindered by the "sign problem" [11, 12] (the probability of different configurations of quarks and gluons becomes complex, which leads to oscillations in Monte Carlo sampling used for the path integral computation). Different approximations are used in, so-called, QCD-inspired calculations, to predict the shape of the SIM phase-space diagram as well as thermodynamical models are built. So far, the first-order phase transition between the hadron gas and QGP is predicted by models [13, 14] and denoted in Fig. 1.2 with a wide, grey band. Experimental results also suggest the presence of the phase transition in this region [15]. The subject of great discussion among researchers is the presence of the critical point (second-order phase transition) between the hadron gas and the QGP. There are models which predict the presence of the critical point [14] as well as models which deny its existence [16]. Predictions of the models which assume the presence of the critical point are inconclusive since the calculations depend on many parameters, e.g. quark masses in QCD-inspired calculations. An example of the theoretical prediction of the critical point position is within $T \in (135 - 140)$ MeV and $\mu_B > 300$ MeV [17]. So far there is no convincing experimental evidence of the existence of the critical point.

At high μ_B and low T, the presence of a state called color superconductor is predicted. The only place in the Universe where the baryon density is high enough and the temperature low enough to create the color superconductor seems to be neutron stars [8].

1.3 Quark-gluon plasma creation and properties

The first concept of the existence of QGP was formulated in 1975 [18]. Since then many experiments and discoveries were made to study this state. It is predicted that the QGP appeared at the very beginning of the creation of the Universe [19]. According to the Big Bang Theory, the QGP was present up to 10^{-5} s [20] after the Big Bang before the hadrons were formed. Studying QGP is an important step in understanding the very beginning of our Universe. But how do we define the QGP state?

The QGP is a hot and dense state where quarks are no longer confined in hadrons, thus the free color charges are allowed to propagate in the whole system. As mentioned earlier, the strong potential (Eq. 1.1) keeps quarks confined, however, when the distances between quarks are small enough (and thus momentum transfers large enough), they can gain asymptotic freedom – a state when quarks can propagate freely through the whole system. It is possible for high T (T $\gg$ 200 MeV) or high μ_B. It needs to be underlined that quarks in QGP do not always gain asymptotic freedom. The Lattice QCD calculations for $\mu_B = 0$ suggest that the QGP can be formed at temperature T $\approx$ 157 MeV, which is smaller than 200 MeV. Quarks in this region are not confined in hadrons anymore – they form QGP, but they do not gain asymptotic freedom.

Nowadays, QGP can be created and experimentally studied only via high-energy heavy-ion collisions. Scheme of two possible scenarios during such collision: without and with QGP creation, is shown in Fig. 1.3.

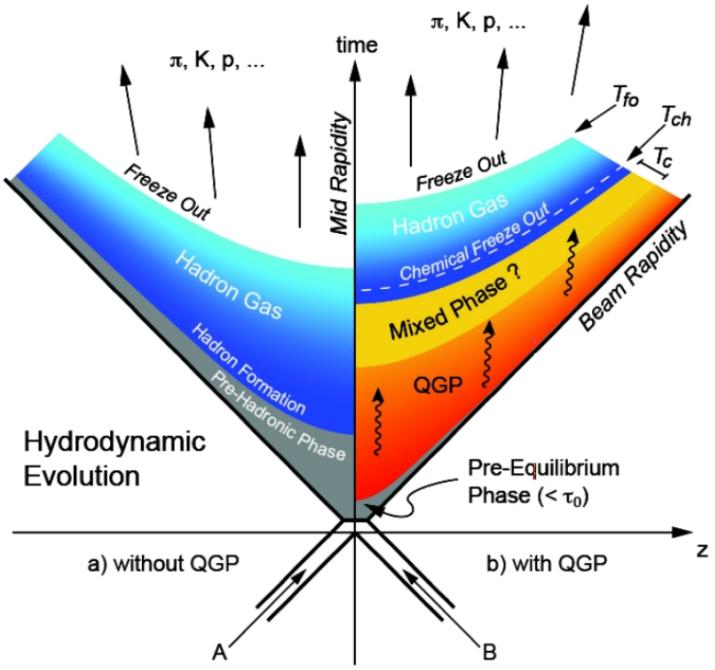

Figure 1.3: Scheme of the time-space evolution of the heavy-ion collision [21].

During the first scenario, without the creation of QGP, the energy density (ϵ) and the temperature is not high enough to free quarks and gluons from hardons. The second scenario, with the creation of QGP, is the subject of our interest. At the very early stage of the collision, there is the

so-called *pre-equilibrium phase*. This is a phase when the system is not at thermal equilibrium and thus it can not be described using thermodynamical variables. The system is in this state for the time called *plasma formation time* (τ_0) which is equal $\tau_0 \approx 1$ fm/c[(a)] according to the Bjorken Model [22]. Next, the volume with high energy density called a fireball is formed and within it, the QGP is created. The temperature and the energy density of created QGP depend on the size of the collided system and the center-of-mass energy of the collision. Different accelerators provide different values of these parameters, so e.g. in the SPS (Super Proton Synchrotron at top energy), T $\approx$ 230 MeV and $\epsilon \approx 3$ GeV/fm^3 while in the LHC (Large Hadron Collider), T $\approx$ 700 MeV and $\epsilon > 15$ GeV/fm^3 [23]. Although a fireball is not a system staying in global thermal equilibrium since it expands very quickly, it can be described using local thermal equilibrium. Moreover, the number of interacting nucleons is large and thousands of particles are produced inside of the fireball are interacting in both an elastic and an inelastic manner. Another argument for thermalization comes from the experimental data showing that different particles are emitted from a source of the same temperature [24]. The expansion of the fireball in all directions is followed by the cooldown of the matter. As the QGP expands and cools, the energy density decreases, and the system undergoes a phase transition called hadronization. This phase transition involves the transition of the deconfined quarks and gluons into color-neutral bound states known as hadrons. Created hadrons may interact with each other inelastically, producing new particles till the phase reaches the temperature of chemical freeze-out (T_{ch}). The T_{ch} depends on the collision energy and the centrality of the collision, however, $T_{ch} \approx 150$ MeV for central collisions at energies $\sqrt{s_{NN}}$[(b)]> 10 GeV [25]. After the chemical freeze-out, no new particles are produced or destroyed and the chemical composition of matter is fixed (however the decays are still possible). Further fireball expansion and cooling cause kinetic (thermal) freeze-out. The temperature of kinetic freeze-out (T_k) also depends on the collision energy and the centrality of the collision. For central collisions at energies $\sqrt{s_{NN}} > 10$ GeV, $T_k \approx (90 - 110)$ MeV [26, 23]. At this point, particles do not interact with each other and their momenta do not change. Particles after kinetic freeze-out are those registered by the detectors. The information the particles provide can be used to reconstruct the properties of the collision: Was the QGP created or not? What was the chemical and kinetic freeze-out temperature?

The T_k can be extracted using the transverse mass[(c)] distributions of different particle species, fitted within the Blast-Wave models (for example see Ref. [27]). The T_{ch} can be estimated using the total multiplicities or multiplicity ratios and fitting them with the Statistcal Hadron Gas Model (with the condition of chemical equilibrium or almost chemical equilibrium), for example, see Refs. [28, 29]. Both freeze-out temperatures are sensitive to collision energy, system size, and centrality of the collision.

[(a)] 1 fm/c $\approx 3.3 \cdot 10^{-24}$ s

[(b)] $\sqrt{s_{NN}}$ - the available center-of-mass energy per nucleon pair

[(c)] $m_T = \sqrt{p_T^2 + m_0^2}$, where p_T – transverse momentum of the particle, m_0 – the rest mass of the particle

1.3.1 Heavy-ion collision experiments

Currently, there are several accelerator and detector setups that are capable to accelerate heavy ions and register the data from the collisions. Those are:

- LHC, located at CERN (The European Organisation for Nuclear Research) in Switzerland and France, is currently the most powerful accelerator in the world, capable of colliding lead ions, currently at 5.36 TeV per nucleon pair, and protons at 13.6 TeV. There are four main experimental setups in the beamline: ALICE, ATLAS, CMS and LHCb, each operating a detector dedicated to studying the different phenomena. The QGP research and study of the diagram of strongly interacting matter is currently performed by all four experiments.
- SPS is also located at CERN and accelerates particles before injecting the beam into LHC. However, it is not its only function. SPS also provides a beam for experiments e.g. NA61/SHINE, NA60, COMPASS. It can accelerate the lead ions up to 158A GeV/c beam momentum ($\sqrt{s_{NN}}$ = 17.3 GeV) and protons up to 450 GeV/c beam momentum ($\sqrt{s_{NN}}$ = 28.1 GeV).
- RHIC (Relativistic Heavy Ion Collider) is located at BNL (Brookhaven National Laboratory) in the United States of America and it provided the beam for, among others, the STAR (Solenoidal Tracker at RHIC) and PHENIX (Pioneering High Energy Nuclear Interaction eXperiment) experiment. It can accelerate gold ions up to $\sqrt{s_{NN}}$ = 200 GeV.
- FAIR (Facility for Antiproton and Ion Research) is currently under construction at GSI Helmholtz for Heavy Ion Research in Germany. The planned maximum center-of-mass energy per nucleon pair is 7.5 GeV for p+p collisions and 4.7 GeV for heavy-ion collisions.

1.3.2 Quark-gluon plasma signatures

The possible creation of the QGP in the collision can be studied via several QGP signatures:

- Strangeness enhancement

  Several properties make the strangeness enhancement a very promising observable of QGP production. First, the initial strangeness before the collision is approximately equal to zero, so all observed strangeness is produced during the collision. Second, the energy threshold for strangeness production in QGP is lower than in hadron gas and the produced strangeness survives the hadronization since the weak decay processes are slower than the process of hadronization. The enhancement factor for strangeness in A+A[(d)] systems compared to p+p or p+A is at the level of 2 or more, depending on the particles and their constituents. The strangeness enhancement was observed at SPS, RHIC, and LHC [30, 31, 32] energies. The above studies suggest that strangeness enhancement increases with the number of collision participants. Due to the threshold on strangeness production, strangeness enhancement decreases with the collision energy, which makes strangeness enhancement the evidence necessary but not sufficient itself to confirm the QGP production [33].
- Charmonium suppression

[(d)] A+A stands for "nucleus-nucleus"

In the presence of QGP, the color charge of quarks, similar to electric charge, is screened due to the phenomenon called "Debye screening". Its impact can be studied via J/ψ meson production whose constituents are c quark and $\bar{c}$ antiquark. Due to the color screening the interaction between c and $\bar{c}$ becomes weaker which finally leads to the dissociation of the $c\bar{c}$ pair and prevents the creation of J/ψ meson. Experimental results confirm charmonium suppression in *A*+*A* collisions [34], where it is the most expected. However, several anomalies occur which can not be explained by the above mechanism, for example, the same level of suppression at SPS and RHIC energies [35].

- Electromagnetic probes
  Electromagnetic probes state for two observables: direct photon production and low-mass dilepton production. Since photons and leptons do not interact via strong force, they carry information about the stage of the collision they were produced in, e.g. QGP. Direct photons are defined as the prompt photons from the first stage of collision and the thermal photons are photons produced in a hot phase. The momentum spectra of photons, in particular, the thermal photons to prompt photons ratio, may provide information about the QGP temperature. Experimental data shows thermal photon enhancement at low p_T in Au+Au collisions at RHIC energies [36]. The measurements of enhanced low-mass dilepton production at SPS and RHIC energies suggest enlarged resonance width of the ρ meson which may be the signature of chiral symmetry restoration and thus a creation of QGP [37, 38, 39, 40].
- Jet quenching
  Jets are "sprays" of high-energy hadrons propagating in a common direction which originate from parton (quark or gluon) fragmentation. They are present in high-energy collisions where the probability of hard scattering (interaction with large momentum transfer) on single partons is relatively high. It is expected that, when QGP is created, the jets may lose their energy in the process of propagating through a dense medium (braking radiation and elastic collisions with other partons). Jet quenching can be studied using, among others, a variable called nuclear modification factor (R_{AA}) which is usually defined as a ratio of the particle yield in *A*+*A* collisions to the corresponding yield in *p*+*p* collisions. It is expected that for high p_T, R_{AA} should saturate at 1 if no nuclear effects (like QGP production) occur. Experimental results at RHIC and LHC energies show R_{AA} suppression at high p_T for collision energy higher than 39 GeV [41, 42]. Jet quenching may be the signature of the presence of QGP, however, it is difficult to determine the exact collision energy at which QGP is created due to significant contributions from other nuclear effects.

A very interesting prediction of the energy threshold of the first-order phase transition between the hadron gas and the QGP is given by the Statistical Model of the Early Stage (SMES) proposed in 1999 by M. Gaździcki and M. Gorenstein [43]. As every model, it has several assumptions and conditions to simplify this multidimensional problem. Those are mainly:

(a) the first-order phase transition in the whole range of μ_B – no critical point neither cross-over between two phases,

(b) only three phases exist: confined, mixed and deconfined

(c) hadronization temperature (the temperature of the mixed phase) is a model parameter and it is set to T = 200 MeV,

(d) quarks and gluons are thermalized at the early stage of the collision,

(e) the number of degrees of freedom of the system increases during deconfinement due to the activation of partonic degrees of freedom,

(f) the total entropy and the total number of strange quarks are not changing during hadronization,

(g) the total entropy is proportional to the number of pions since they are the biggest fraction of the newly produced particles (≈ 90%).

The SMES predicts three structures which can be probed experimentally, so-called: "kink", "horn" and "step". They are shown in Fig. 1.4.

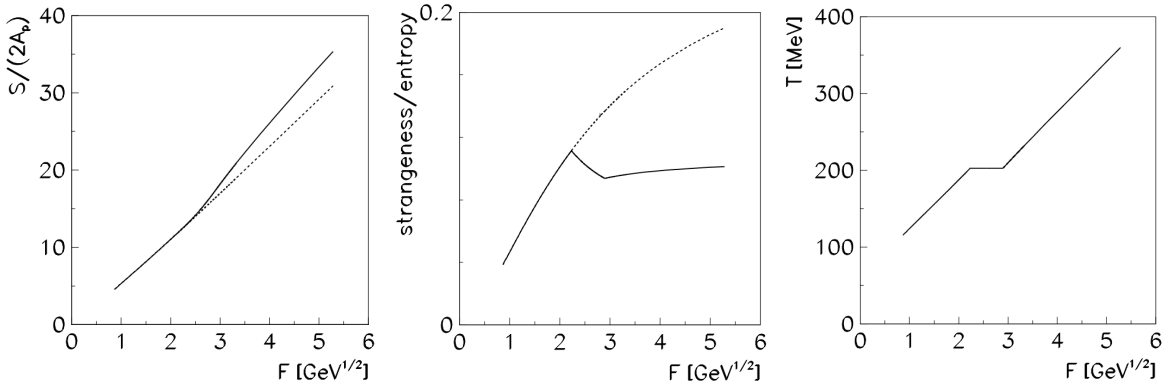

Figure 1.4: From the left: "kink", "horn" and "step" structures predicted by the SMES [43] as a function of F = $(\sqrt{s_{NN}})^{1/2}$. For the description see Sec. 1.3.2.

The first one, "kink", is a prediction of the ratio of the total entropy to the total number of nucleons participating in the collision as the function of collision energy. If there is no phase transition, the linear increase with the collision energy should be observed. The slope of this growth should be proportional to the number of degrees of freedom of the system and since the number of degrees is expected to increase during the deconfinement, the slope also increases. The second structure, "horn", shows the total strangeness produced in the collision to the total entropy as the function of collision energy. It predicts an increase at low energies which stops when the deconfinement starts (mixed phase appears), decrease with the increasing QGP fraction to the point when the phase contains only QGP and then approximate saturation or weak increase with the energy. The last structure, "step", shows temperature as the function of collision energy. It predicts the linear increase of the temperature with energy when only one phase is present (confined or deconfined matter) and plateau during the mixed phase. Those structures are visible in Pb+Pb and Au+Au collisions by NA49 and STAR experiments, see Fig. 1.5, and are the subject of further studies in NA61/SHINE [44].

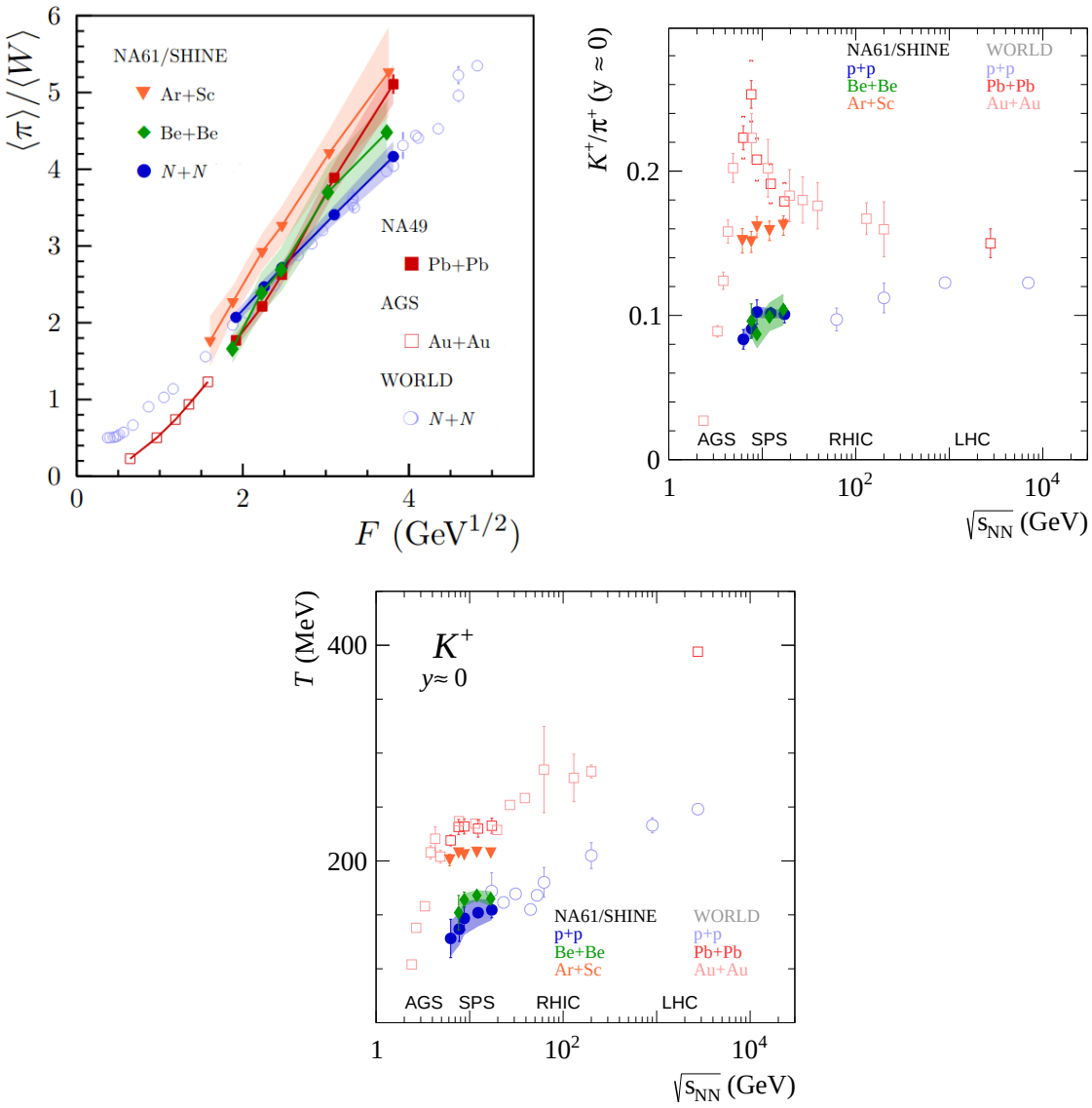

Figure 1.5: Top, left: "kink" (the mean multiplicity of pions by the mean number of wounded nucleons[(e)]); Top, right: "horn" (the ratio of the production of the positively charged kaons to positively charged pions at the central rapidity[(f)]region – midrapidity); Bottom: "step" (the inverse slope parameter of exponentially shaped transverse mass spectra of K^+, which may be connected to the temperature of the early stage) structures in the experimental data from, among others, NA49, NA61/SHINE, and STAR [45, 46, 47].

[(e)]wounded nucleon – nucleon from colliding nuclei that interacted inelastically (a measure of the centrality of the collision)

[(f)]rapidity – kinematic characteristics of produced particles defined as $y = \frac{1}{2}\ln\frac{E+p_l}{E-p_l}$, where E – total energy of the particle ($E = \sqrt{p^2 + m_0^2}$ assuming $c \equiv 1$, p – total momentum of the particle, m_0 – invariant mass of the particle), p_l – particle longitudinal momentum (momentum in the direction of the beam).

Chapter 2

Event-by-event fluctuations

In a colliding system, two types of fluctuations may occur: statistical and non-statistical. Statistical fluctuations come from the finite size of the colliding system and thus, the finite produced particle multiplicity. The non-statistical fluctuations are often called the dynamical fluctuations and originate from the physical processes occurring during the collision. The dynamical fluctuations may come from:

- different event classes of different properties, like the events when QGP was created and the events when QGP was not created,
- fluctuations in the initial energy density for particle production,
- two-particle correlations due to decays of short-lived resonances, quantum properties of the particles, and Coulomb interactions, the number of which can fluctuate in an event-by-event manner,
- multi-particle correlations due to collective flow of particles and jet production,
- the presence of the critical point,
- impact parameter[(a)] fluctuations,
- detector acceptance,
- conservation laws.

The quantities which have been used to measure the multiplicity fluctuations in ^{40}Ar+^{45}Sc collisions are defined in Sec. 2.1. The influence of different physical phenomena on fluctuations is discussed in detail in Sec. 2.2.

2.1 Measures of event-by-event fluctuations

Fluctuations are defined by moments of a given distribution higher than the first moment. In this thesis, only the multiplicity and net-electric charge[(b)] fluctuations are studied, but a similar methodology can be used to study any event variable.

One of the obstacles in fluctuation measurement in heavy-ion collisions is the inability to fix the size of the colliding system. It can be partially controlled by choosing a specific centrality of the collision, which is defined by the impact parameter. The impact parameter is the distance between the centers of the colliding nuclei, so the smaller the impact parameter, the more central the collision, and the more nucleons will participate in the collision (such nucleons are called

[(a)] impact parameter – the distance between the centers of colliding nuclei

[(b)] "Net-electric charge" is called further in the text "net-charge", for better readability.

participants). Experimentally, one can obtain events in centrality classes defined in %, where 0% means the most central collisions and 100% means so-called *minimum bias* events where all centralities are accepted. The centrality selection is obtained in different manners in different experiments. A more detailed description of the centrality selection of events used in this analysis is provided in Chap. 4. Nevertheless, the number of participants varies from event to event, and this fact needs to be taken into account during the data analysis. In order to compare fluctuations measured in different systems (e.g. *p*+*p*, ^{7}Be+^{9}Be, ^{40}Ar+^{45}Sc), one requires using quantities independent of the system size. Such quantities are called intensive quantities, and they are introduced below.

Intensive quantities are the quantities independent of the system size but still dependent on the system size fluctuations. They can be used to compare fluctuations in different systems; however, their sensitivity to the system size fluctuations should be taken into account. This effect can be minimized by selecting the narrowest centrality bin possible while preserving sufficient data statistics which does not introduce large statistical fluctuations. The intensive quantities are obtained by dividing two extensive quantities (which depend on the system size), e.g. algebraic $\langle N^n \rangle$ (Eq. 2.1) or central μ_n (Eq. 2.2) moments of the distribution of the N quantity:

$$\langle N^n \rangle = \sum_N N^n P(N) \ , \tag{2.1}$$

$$\mu_n = \sum_N (N - \langle N \rangle)^n P(N) \ , \tag{2.2}$$

where P(N) is the probability distribution of N. The moments can also be described in terms of cumulants κ_n (Eq. 2.3), as

$$\kappa_1 = \langle N \rangle, \quad \kappa_2 = \mu_2, \quad \kappa_3 = \mu_3, \quad \kappa_4 = \mu_4 - 3\mu_2^2 \ , \ \dots \ . \tag{2.3}$$

As stated in Ref. [48], cumulants have several properties which make them convenient for fluctuation analysis in heavy-ion collisions. First, cumulants of the probability distribution of the sum of two uncorrelated stochastic variables are given by the sum of the cumulants of those variables. From this property, one can draw the conclusion important for the statistical mechanics, that in the Grand Canonical Ensemble, if the volume of the system is large enough, the cumulants of extensive variables are extensive variables themselves. Second, higher-order cumulants vanish for the Gauss distribution, thus they are a good measure of the deviations from it. The deviation from other probability distributions can also be easily obtained by looking at the ratios of cumulants (intensive quantities) which scale to 1. Such quantities are used in this research to study the deviation from Poisson and Skellam distributions[(c)] and are presented below.

For multiplicity fluctuations, which are expected to obey the Poisson distribution in case of independent particle production following the ideal Boltzmann gas model in Grand Canonical Ensemble formulation, the following quantities were used:

[(c)] The detailed description of the Poisson and Skellam distributions is presented in Appendix A.

- scaled variance: $\kappa_2[N]/\kappa_1[N]$,
- scaled skewness: $\kappa_3[N]/\kappa_2[N]$,
- scaled kurtosis: $\kappa_4[N]/\kappa_2[N]$,

where N is further noted as h^+ in case of positively charged particles and h^- in case of negatively charged particles. The quantities for net-charge ("net" is defined as "$h^+ - h^-$") have to be defined differently since net-charge is not a variable following the Poisson distribution but a Skellam one. Skellam distribution is a distribution defined as the difference of two independent random variables, each of them Poisson distributed. The intensive quantities which keep the same reference values for net-charge are defined as:

- scaled variance: $\kappa_2[net]/(\kappa_1[h^+] + \kappa_1[h^-])$,
- scaled skewness: $\kappa_3[net]/\kappa_1[net]$,
- scaled kurtosis: $\kappa_4[net]/\kappa_2[net]$.

It is expected that if there are no fluctuations, the quantities are equal to zero. If the multiplicity distribution varies according to the Poisson distribution (or net-charge according to Skellam), the quantities are equal to one.
The properties introduced above can be derived from the Wounded Nucleon Model (WNM) proposed in Ref. [49]. It is one of the simplest models of ion-ion collision, which assumes that particle production in nucleon-nucleus and nucleus-nucleus collisions is an incoherent superposition of particle production from nucleons participating in the collisions. The WNM introduces two types of nucleons: N_W – wounded nucleons and N_{spec} – spectators. The N_W are nucleons which interacted inelastically during the collision and N_{spec} – nucleons which did not interact. Using WNM, it can be shown that if N_W varies, then intensive quantities are functions not only of particle production in a single wounded nucleon but also of the N_W. In this case, the intensive quantities are given by Eqs. 2.4 – 2.6 [50], as:

$$\omega[N] = \omega[n] + \langle n\rangle\omega[N_W] \,, \tag{2.4}$$

$$S\sigma[N] = \frac{\omega[n]S\sigma[n] + \langle n\rangle\omega[N_W](3\omega[n] + \langle n\rangle S\sigma[N_W])}{\omega[n] + \langle n\rangle\omega[N_W]} \,, \tag{2.5}$$

$$K\sigma^2[N] = \frac{\omega[n]K\sigma^2[n] + \omega[N_W]\left(\langle n\rangle^3 K\sigma^2[N_W] + \langle n\rangle\omega[n](3\omega[n] + 4S\sigma[n] + 6\langle n\rangle S\sigma[N_W])\right)}{\omega[n] + \langle n\rangle\omega[N_W]} \,, \tag{2.6}$$

where the quantities with index $[n]$ are the quantities obtained from a single wounded nucleon, $\langle n\rangle$ is a mean multiplicity of particles from a single wounded nucleon, and the quantities with

the index [N_W] characterize the system size change. For better readability, the following notation has been used: $\omega = \kappa_2/\kappa_1$, $S\sigma = \kappa_3/\kappa_2$, $K\sigma^2 = \kappa_4/\kappa_2$.

2.2 Influence of different physical phenomena on fluctuations

As it was mentioned above, the non-statistical fluctuations, which are the subject of interest, are a mixture of different effects, some of them being correlated to each other. The signal coming from the most desirable phenomena, the presence of the critical point (CP), may be shielded by the other. Several studies have been made with consideration of the multiplicity and net-charge distribution characteristics within different statistical ensembles and different gas models.
The nuclear matter is usually modeled within three following statistical ensembles: the Micro-canonical Ensemble (MCE), the Canonical Ensemble (CE), and the Grand Canonical Ensemble (GCE). Different ensembles should be used to describe the collisions of the systems of different sizes, more precisely the choice of the ensemble depends on the number of particles produced in the collision. The collisions of large *A*+*A* systems and high energies can be well described within the GCE while the small *N*+*N* systems or *A*+*A* systems at low energies should be modeled with CE or MCE due to the low statistics and the proper handling of the conservation laws.
The comparison of the fluctuations in the CE and in the GCE was made in Ref. [51] where the ideal gas model with two particle types: π^+ and π^- with total charge equal to 0, was considered. The example multiplicity distributions of π^+ or π^- at different z are shown in Fig. 2.1. The z argument is called the partition function and it is proportional to the volume of the system. The

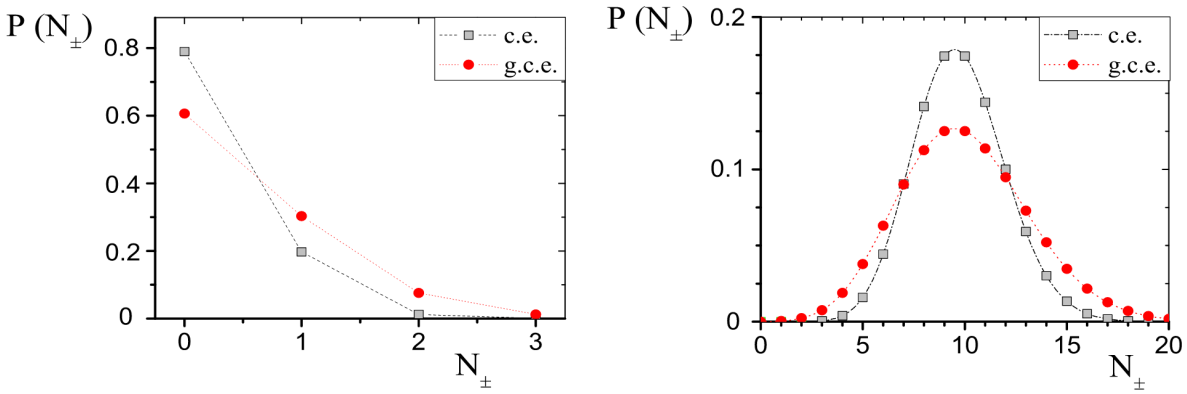

Figure 2.1: Multiplicities of positively or negatively charged pions calculated within CE and GCE at z=0.5 (on the left) and z=10 (on the right) [51].

z dependence of the ratio of the mean multiplicity in CE to GCE is shown in the left panel of Fig. 2.2. For the infinite system ($z \to \infty$) the results for CE and GCE converge to 1 which marks the equivalence of both ensembles. Going to the other side, for the ($z \ll 1$), the ratio decreases to zero. The difference is also seen in the scaled variance, see the right panel of Fig. 2.2. It was stated earlier in this chapter, that for the Poisson distribution, the scaled variance is equal to 1. The result is the same for the GCE calculations. However, it seems not to be the case for CE. For

small systems ($z \ll 1$) the scaled variance in CE is equal to the scaled variance in GCE but for large systems ($z \gg 1$) the scaled variance in CE saturates at 0.5, which makes it 2 times smaller than in GCE.

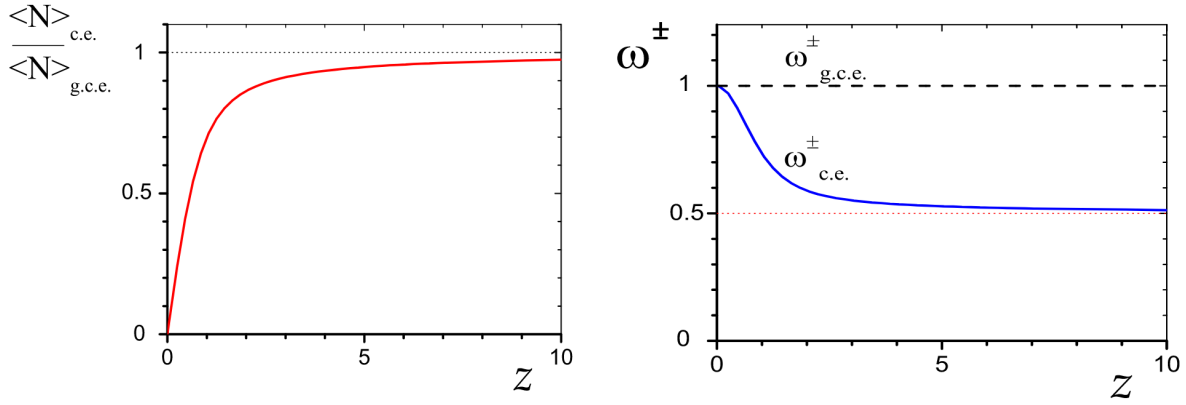

Figure 2.2: Left panel: z dependence of the ratio of positively or negatively charged pion mean multiplicity calculated within CE to GCE. Right panel: z dependence of the scaled variance of the positively or negatively charged pion multiplicity distribution [51].

The increase of the fluctuations may be observed when the chemical freeze-out and hadronization occur near the critical point. A maximum of this effect is shown when there is no hadron phase before the hadronization, which means the hadronization occurs at the freeze-out [52]. Near the critical point (which is the second-order phase transition), the fluctuations are enhanced, leading to a power-law behavior in the higher-order moments (or cumulants) of the distribution of the measured variable (e.g. multiplicity or transverse momentum distribution). This contribution of the critical fluctuations to the moments is proportional to a positive power of the correlation length, denoted by ξ. In a thermodynamic limit (with an infinite number of particles), ξ diverges at the critical point. However, in reality, the system spends only a finite time in the vicinity of the critical point, so the correlation length reaches a maximum value at the critical point but does not diverge to infinity. The finite size of the system also imposes a limitation on the growth of the correlation length. However, it turns out that the finite time is a more strict limitation on the growth of the correlation length than the finite size [53].
A very convenient method of the critical point search is a 2D scan in the T $-$ μ_B phase space, which can be done by changing the collision energy and the size of the colliding system. Such a scan is an essential part of the NA61/SHINE experiment physics program (see more details in Chap. 3). Depending on the quantity, e.g. for intensive measures of particle multiplicity (see Sec. 2.1), the critical behavior may be visualized as the "hill of fluctuations", which is expected to be seen in the vicinity of the critical point during the scan. The scheme of the "hill of fluctuations" is shown in Fig. 2.3.

Due to many physical phenomena occurring during the evolution of the collided system, it is very difficult to give quantitative predictions of the intensive quantities' behavior in the vicinity

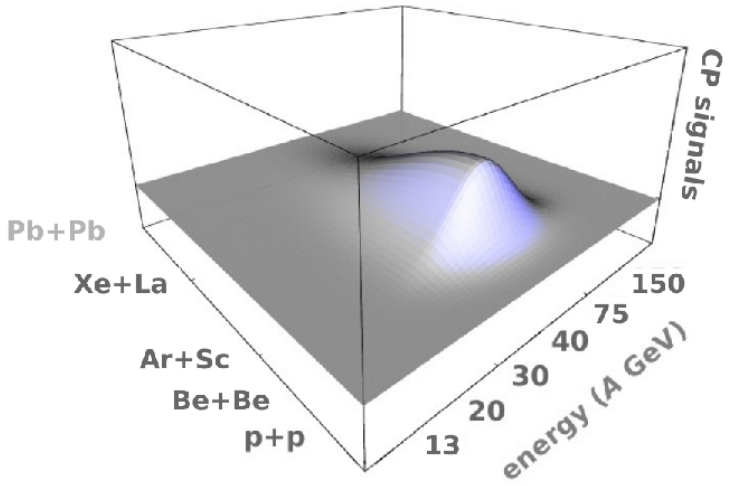

Figure 2.3: The "hill of fluctuations" – a schematic graph of the increase of fluctuations in the vicinity of the critical point while changing the collision energy and the size of the colliding system [54].

of the critical point. However, in the simplified situation, when the nuclear matter is described within the Van der Waals equation of state [55], the intensive quantities will follow the behavior shown in the Fig. 2.4 (for a more detailed discussion on net-baryon fluctuations, see Ref. [56]). This model shows that the higher-order quantity, the more sensitive it is to the second-order phase transition however their qualitative behavior is different. The scaled variance diverges at the critical point, while the scaled skewness and the scaled kurtosis seem to change their values rapidly depending on the location in the phase-space diagram. This model shows that studying the higher-order moments can bring new information about the phase transition between the QGP and the hadron gas.

2.3 Recent experimental results

Multiplicity and net-charge fluctuations at different energies and with varying sizes of the system have been studied by multiple experiments, among them NA49 [57, 58, 59], STAR [60, 61] and PHENIX [62, 63]. The summary of recent experimental results on multiplicity and net-charge fluctuations is shown in this section. So far, some indications of the CP have been observed, but they were not confirmed. A more detailed study of fluctuations of light and intermediate mass systems is needed.

2.3.1 NA49

Multiplicity fluctuations of positively, negatively and all charged particles were analyzed for Pb+Pb, Si+Si, C+C, and *p*+*p* collisions at different energies by NA49. The decrease of scaled variance of all charged particles and approximately constant behavior of the scaled variance of positively and negatively charged particles with increasing μ_B (what corresponds to decreasing collision energy) was shown in the analysis of Pb+Pb at two different rapidity intervals:

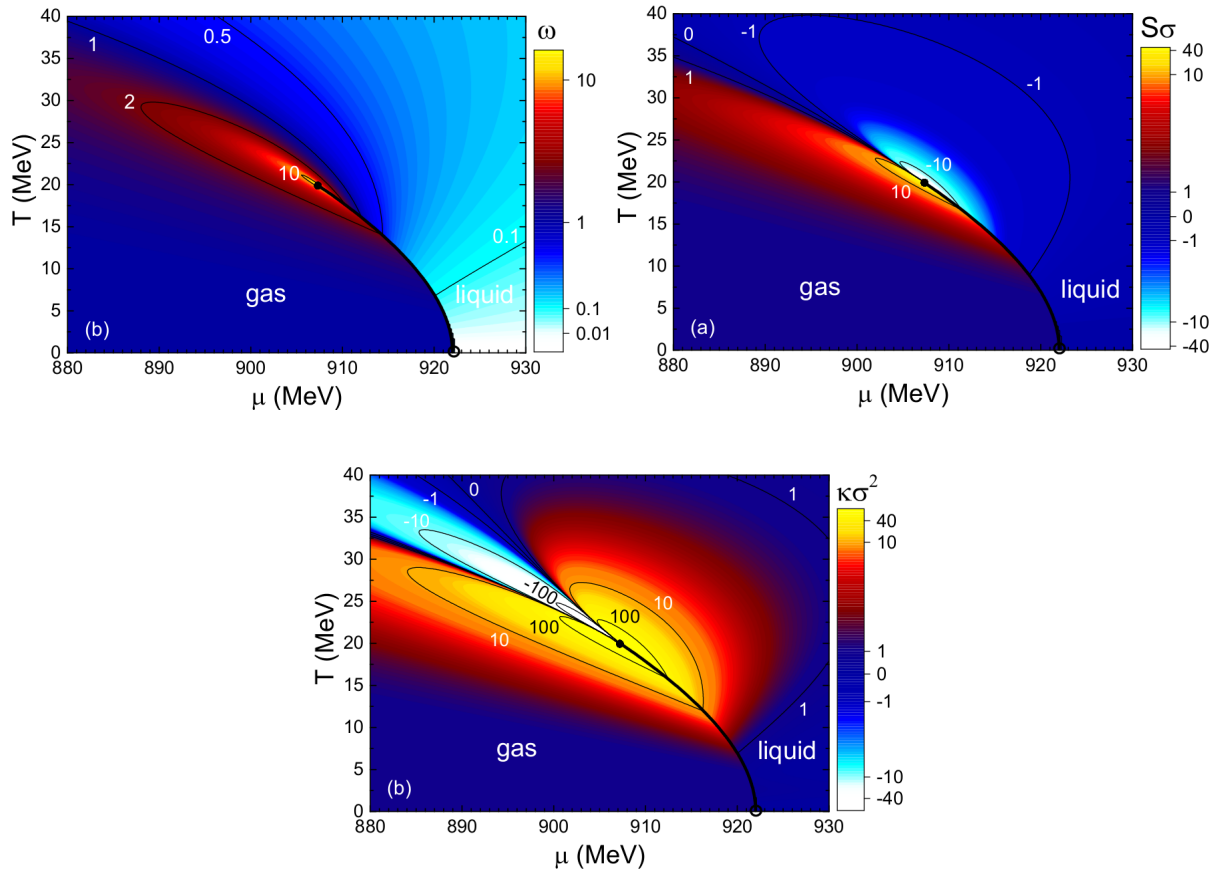

Figure 2.4: Scaled variance (top, left), scaled skewness (top, right) and scaled kurtosis (bottom) calculated in [T, μ_B] coordinates within van der Waals equation of state for fermions. The solid circle in the diagram corresponds to the critical point, and the open circle at T = 0 denotes the ground state of nuclear matter [55].

$0 < y_\pi < y_{beam}$ and $1 < y_\pi < y_{beam}$[(d)]. The results are presented in Fig. 2.5. The energy dependence of the scaled variance of multiplicity distributions in Pb+Pb collisions does not show any non-monotonic behavior and thus, it gives no information about the possible critical point presence. Further investigation of lighter nuclei collisions, i.e. *p*+*p*, C+C, and Si+Si, brought more promising results shown in Fig. 2.6. The system size dependence of the scaled variance of all charged particles shows a clear maximum for medium size nuclei.

The limited statistics make the measured signal difficult to interpret. To improve the quality of the data, the NA61/SHINE experiment was proposed. Its goal is to extend these measurements for a yet uncovered region of the phase diagram by performing the first system size and energy scan. Another extension is to add measurements of higher-order moments that were not measured by NA49.

[(d)] y_{beam} is the rapidity of the beam and y_π is the particle rapidity assuming pion mass; values are calculated in the center-of-mass reference system

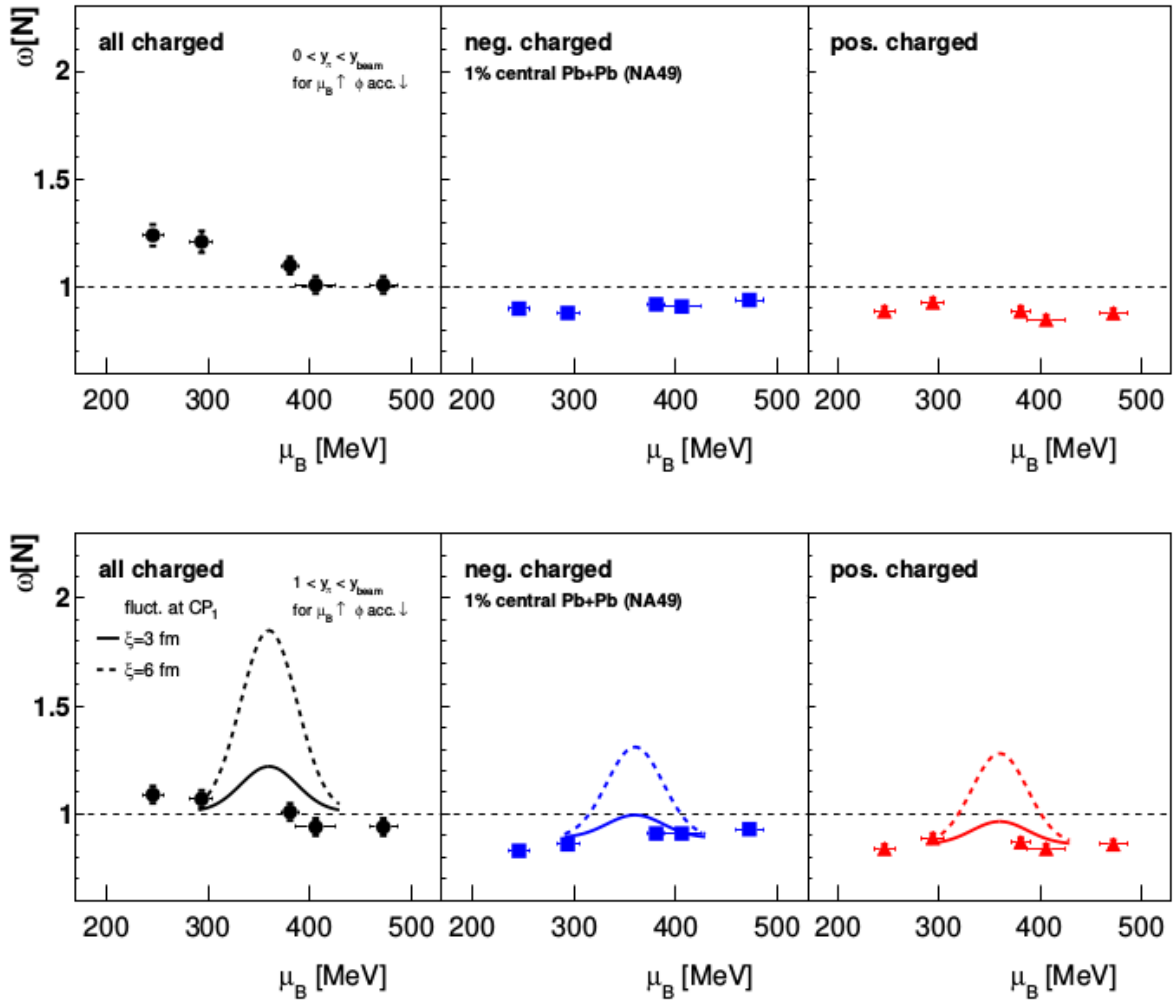

Figure 2.5: The μ_B dependence of the scaled variance of all charged, negatively charged and positively charged particles produced in the 1% most central Pb+Pb collisions at two different rapidity intervals: $0 < y_\pi < y_{beam}$ (top) and $1 < y_\pi < y_{beam}$ (bottom) [57]. Lines correspond to CP predictions [64].

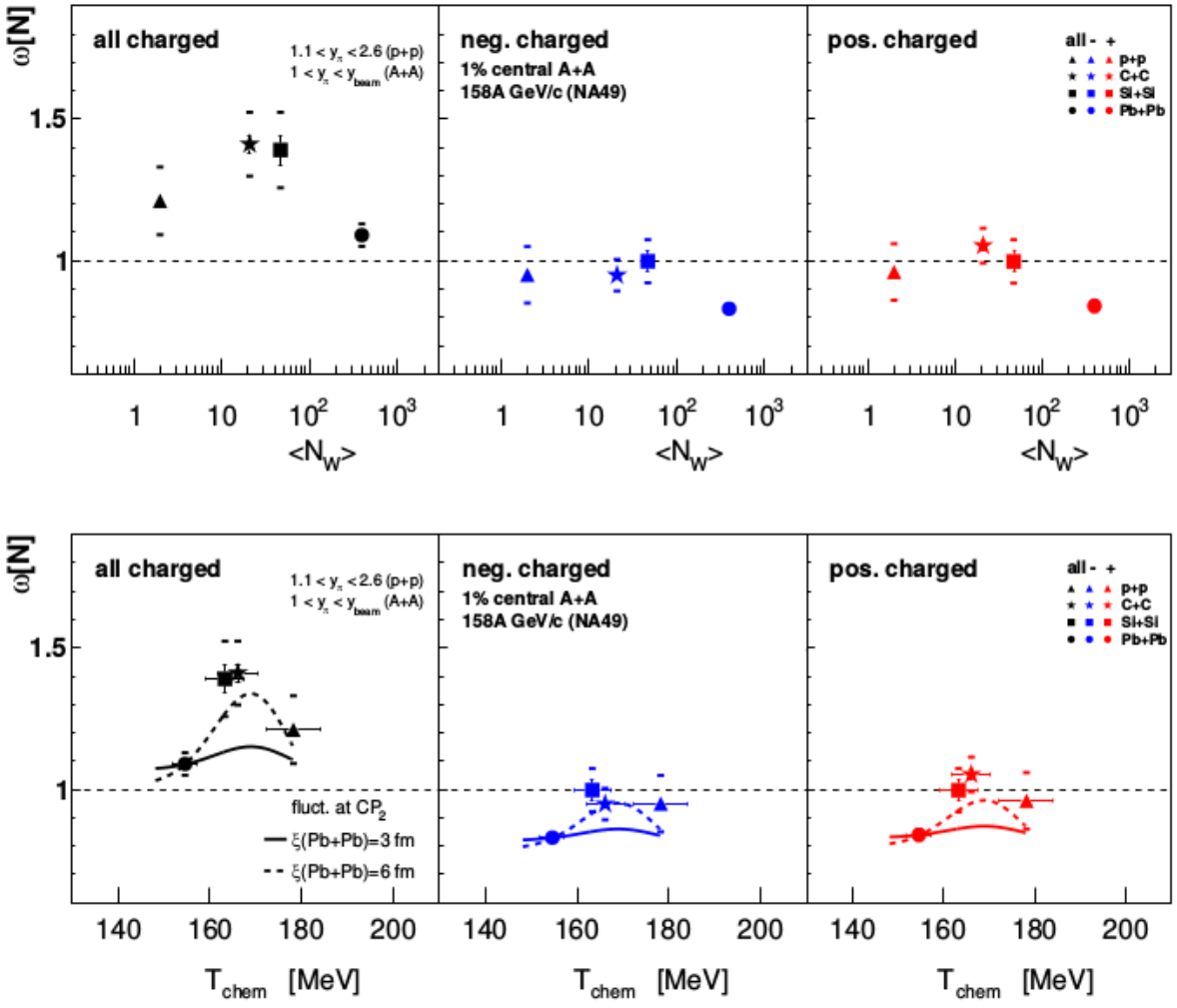

Figure 2.6: The System size (top) and chemical freeze-out temperature (down) dependence of the scaled variance of all charged, negatively charged and positively charged particles produced in the 1% most central Pb+Pb, Si+Si, C+C collisions and inelastic p+p interactions at 158A GeV/c [57, 58, 59]. Lines correspond to CP predictions [64].

2.3.2 STAR

The STAR experiment measures, among other quantities, the net-charge which is related to this study. Their most recent results are presented in Fig. 2.7. STAR is reporting the higher-order variables: σ^2/M, $S\sigma$/Skellam, and $\kappa\sigma^2$, of net-charge in Au+Au collisions at the energy range from 7.7 to 200 GeV. The interpretation of these results can be found below in the direct citation from Ref. [60]:

"No significant deviation from the Poisson expectation is observed within the uncertainties for ΔN_{Ch} *(...) cumulant ratios. Furthermore, the data are consistent within uncertainties with the UrQMD model calculations, which does not include a critical point. No energy dependence is observed for* $S\sigma$/Skellam*, and* $\kappa\sigma^2$*, as well as for the UrQMD calculations."*

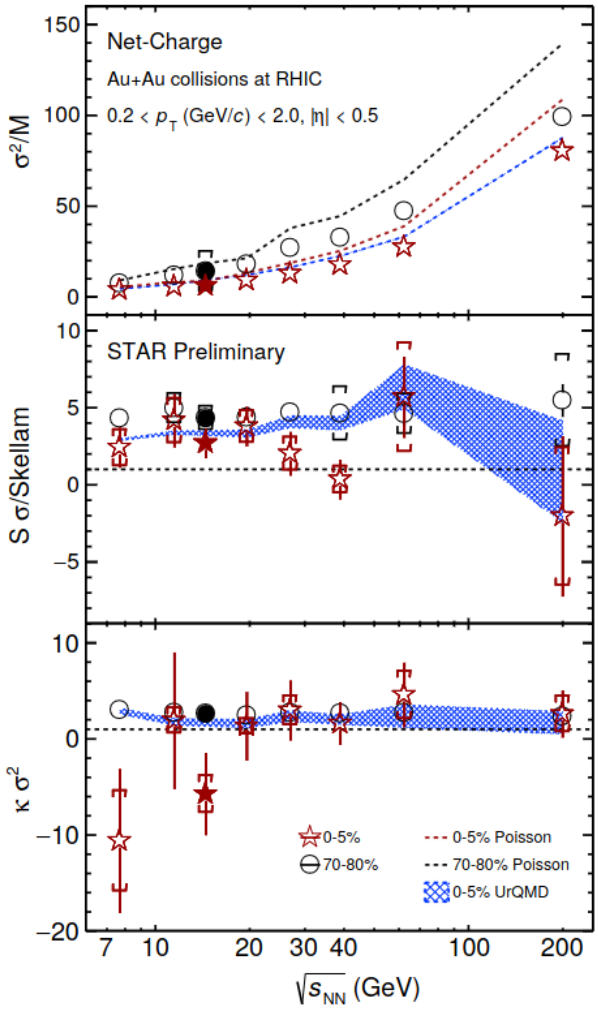

Figure 2.7: The energy dependence of the cumulant ratios of the net-charge distributions. The following quantities are shown: σ^2/M (top panel), $S\sigma$/Skellam (middle panel), and $\kappa\sigma^2$ (bottom panel) for different centrality collisions: 0-5% central (red stars), and 70-80% peripheral (black circles). The dotted lines denotes poisson expectations and the blue band - the URQMD calculations [60].

2.3.3 PHENIX

The PHENIX reports the scaled variance of all charged particle distributions (see Fig. 2.8, left) and the scaled skewness and scaled kurtosis of net-charge distributions (see Fig. 2.8, right) [62] in 0-5% central Au+Au collisions at energy range from 7.7 to 200 GeV. Citing authors of Ref. [62]:

"From the analyses completed to date, there is no significant indication of the presence of the QCD critical point."

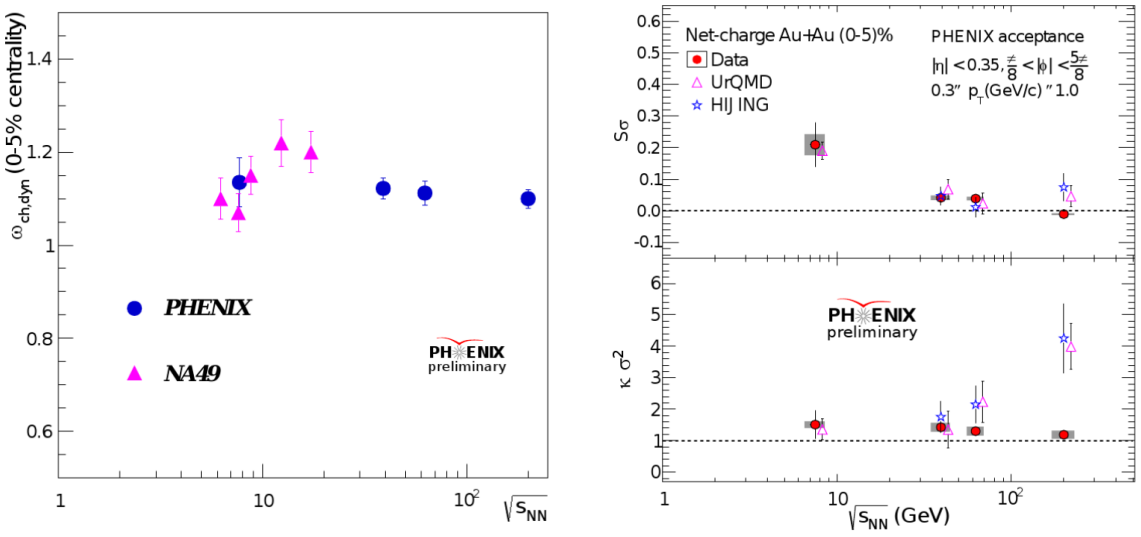

Figure 2.8: Left panel: The scaled variance of all charged particle multiplicity distributions in 0-5% central Au+Au collisions at energy range from 7.7 to 200 GeV (blue points). Compared with NA49 results (magenta points) [62]. Right panel: The scaled skewness (top) and scaled kurtosis (bottom) of net-charge distributions in 0-5% central Au+Au collisions at energy range from 7.7 to 200 GeV (red points). Compared with models: UrQMD (magenta points) and HIJING (blue points) [62].

Chapter 3

NA61/SHINE experiment

The NA61/SHINE [65] is a successor of the NA49 experiment, which was operated in 1994 – 2002, and uses an upgraded apparatus of NA49 [66]. It is a fixed-target experiment located at CERN in the North Area. The NA61/SHINE location with the relevant accelerator complex is shown in Fig. 3.1. The name SHINE stands for **S**PS **H**eavy **I**on and **N**eutrino **E**xperiment. In 2022, the NA61/SHINE detector was upgraded. Among other things, the data rate was increased from $\approx$ 80 Hz up to $\approx$ 1600 Hz, which in the future may highly improve the data-hungry analysis such as the study of fluctuations.

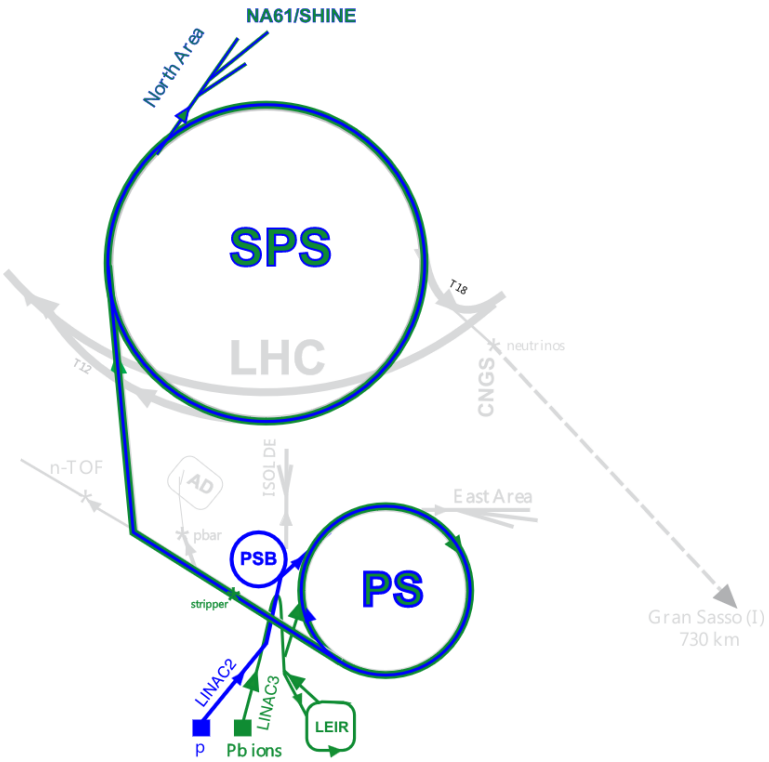

Figure 3.1: Schematic layout of the CERN accelerator complex relevant for the NA61/SHINE experiment (before the Long Shutdown 2 at CERN) [65].

3.1 Physics program

The main goal of the NA61/SHINE experiment is to study hadron production in different types of collisions within the three following programs [66]:

1) **The strong interactions program**.
   The properties of the transition between the QGP and the hadron gas are studied via colliding systems of different sizes at different energies (Fig. 3.2). The main focus of this program is the search for the critical point and the detailed study of the onset of deconfinement.
2) **The neutrino program**.
   The charged pions and kaons produced in the interactions of a proton beam in the thin carbon target or the several target replicas, e.g. T2K, NuMI are measured to help with the best possible estimation of neutrino fluxes and beam composition at the neutrino experiments. The neutrino program newest goal is the set up of the Low-Energy Beamline for more precise measurements such as the hadron-nucleus interaction measurements for flux calculations of atmospheric neutrinos and the flux calculation of accelerator-based short-baseline neutrino beams [67].
3) **The cosmic ray program**.
   The π+C interactions are measured in order to improve the modeling of cosmic ray showers and understanding of the nuclear cascades in the air showers. The measurements of nuclear fragmentation for Galactic Cosmic Rays are also performed [68].

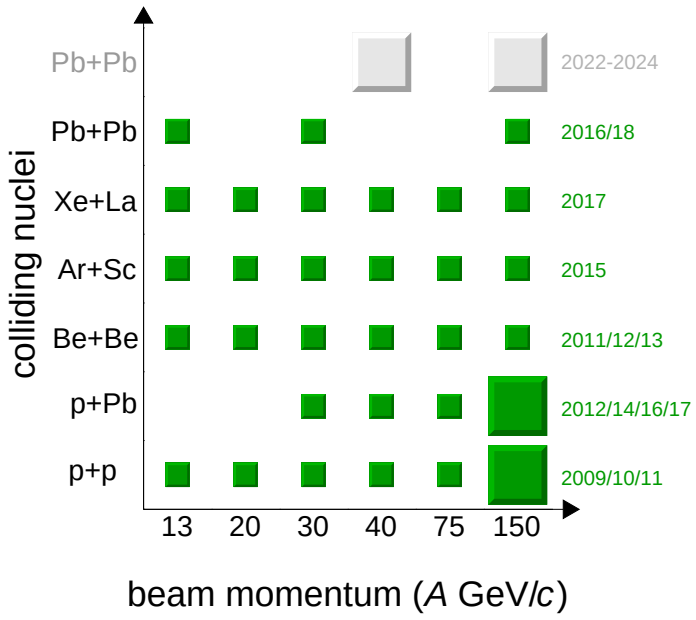

Figure 3.2: Collided systems and beam momenta in the strong interactions program [54]. The Pb+Pb data at 150A GeV/c were partially taken in 2022.

3.2 Experimental facility

The NA61/SHINE is a fixed-target experiment. The experimental setup is adapted for every dataset to assure maximal kinematic detector acceptance. The changes, like the target position, detector position, or magnetic field, depend on the studied interactions and beam momenta. The

setup shown in Fig. 3.3 and described further in this chapter was used during the ^{40}Ar+^{45}Sc data taking at different beam momenta, which are the topic of this thesis.

The argon ions, before they reached the experimental setup, were accelerated in the following CERN accelerators: Linac3 (The Linear accelerator 3), LEIR (The Low Energy Ion Ring), PS (The Proton Synchrotron), and SPS (The Super Proton Synchrotron) [69]. In SPS, ions are accelerated to the required energy, then the beam is de-bunched and extracted to the North Area where the NA61/SHINE experiment is located. Three Beam Position Detectors (BPDs) and a set of scintillation and Cherenkov counters are used for the beam position measurements. Behind the target, there are four large volume Time Projection Chambers (TPCs), which are the main components of the experimental setup used to track produced particles. The first two – vertex TPCs (VTPCs) – are placed in a magnetic field of two superconducting dipole magnets. The following two – main TPCs (MTPCs) – are installed behind the magnets on both sides of the beam. Behind MTPCs, the two modules of the Time-of-Flight (ToF) detectors were situated. Information collected by TPCs and ToF is used for particle identification. The most downstream detector in the setup is the Projectile Spectator Detector (PSD), which provides information about the energy deposited by projectile spectators and allows to determine the centrality of the collision. A more detailed description of the experimental facility can be found in Ref. [65].

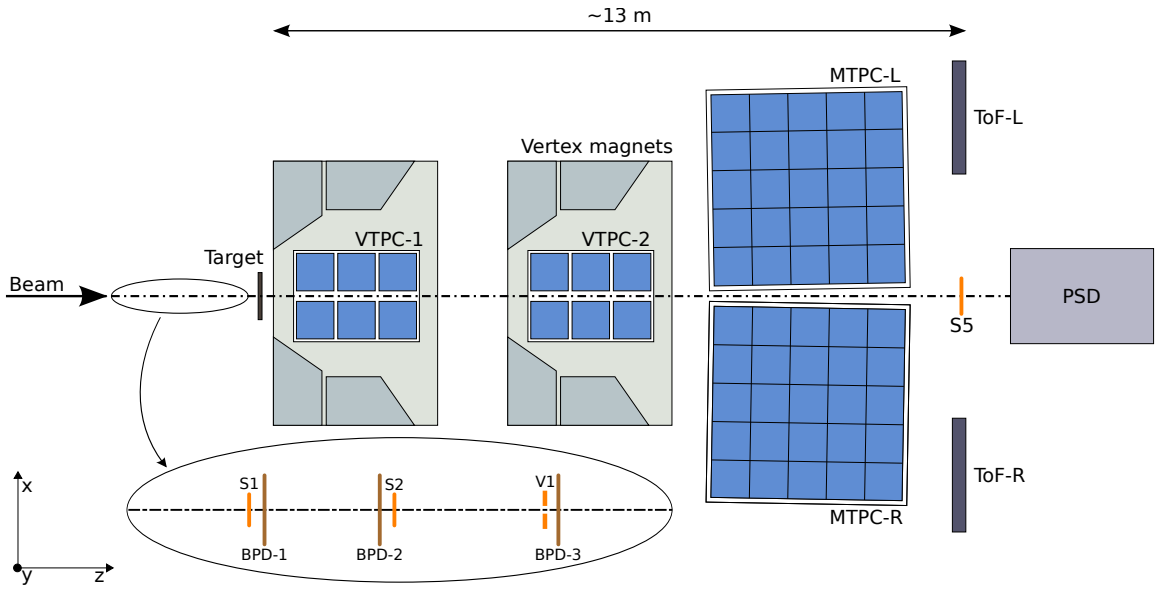

Figure 3.3: The schematic layout [54] of the NA61/SHINE experiment [65] at the CERN SPS showing the components used for the ^{40}Ar+^{45}Sc energy scan (horizontal cut, not in scale). The beam and trigger detector configuration is shown in the inset. The alignment of the chosen coordinate system is shown on the plot; its origin lies in the middle of VTPC-2 on the beam axis. The beam direction is along the z axis. The magnetic field bends charged particle trajectories in the x–y (horizontal) plane. The drift direction in the TPCs is along the y (vertical) axis.

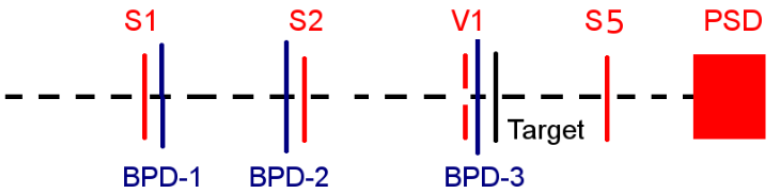

Figure 3.4: The scheme of the beam detectors (BPD-1, BPD-2 and BPD-3) and counters (S1, S2, S5) used as triggers during ^{40}Ar+^{45}Sc data taking.

3.2.1 Beam detectors, counters, and triggers

The beam detectors setup for ^{40}Ar+^{45}Sc data taking is presented in Fig. 3.4. Three BPDs are used for the online measurement of the position of beam particles in the transverse plane. They are placed along the beamline upstream of the target with BPD-3 located just before the target. The detectors are proportional ionization chambers containing Ar/CO_2 85/15 gas mixture. The position of the beam particle is measured in two orthogonal directions using two planes of orthogonal strips. Their time resolution is suitable for high-intensity beams and is equal to around 10^5 particles/second.

There are three scintillators: S1, S2, S5 and one veto counter, V1, mounted along the beamline. They provide timing information and are used to define the triggers. Four triggers were defined for the ^{40}Ar+^{45}Sc data taking. The trigger logic and their aim are presented in Tab. 3.1.

Table 3.1: Trigger logic in ^{40}Ar+^{45}Sc collisions data taking.

Trigger	Configuration	Description
T1	S1×S2×$\overline{\text{V1}}$	event with identified beam particles before the target
T2	S1×S2×$\overline{\text{V1}}$ × $\overline{\text{S5}}$ × $\overline{\text{PSD}}$	event recognized as the most central interactions by the condition of the presence of the beam before the target, no beam behind the target (anticoincidence of the S5 counter) and a threshold on PSD energy (see Tab. 3.2)
T3	S1×S2	beam halo
T4	S1×S2×$\overline{\text{V1}}$ × $\overline{\text{S5}}$	minimum bias trigger – all interactions with the target (no selection on centrality as in T2 trigger)

3.2.2 Target and beam

For ^{40}Ar+^{45}Sc collisions, targets produced in Stanford Advanced Materials were used. The targets were 2 × 2 cm plates of 2 and 4 mm thickness, containing (99.29 ± 1)% of Sc [70]. Both plates (2 + 4 mm) were used during the data taking. The target was positioned at $z \approx -580$ cm (upstream of the VTPC-1 front wall) in a special target holder. The target holder provides a helium atmosphere around the target, which minimizes the probability of off-target interactions when

the beam interacts with the air in the vicinity of the target.
NA61/SHINE can take measurements using both primary and secondary beams, which are derived by the SPS. The ^{40}Ar beam delivered by the SPS accelerator was the primary beam prepared specially for NA61/SHINE, which allowed to avoid the beam impurities visible in the datasets produced by using the secondary (fragmentation) beam (like ^{7}Be). Beams at six different momenta: 13A, 19A, 30A, 40A, 75A, 150A GeV/c were successfully collided with the Scandium target in the experiment.

3.2.3 Time Projection Chambers

Four large volume Time Projection Chambers are the main tracking devices in the NA61/SHINE experiment. There are two vertex TPCs (VTPC-1 and VTPC-2) and two main TPCs (MTPC-L and MTPC-R). They measure the energy deposit of charged particles in a 3-dimensional space. The VTPCs are located in the magnetic field of two superconducting dipole magnets VERTEX-1 and VERTEX $-$ 2, which provide a maximum total bending power up to 9 Tm at currents of 5000 A. The standard configuration for data taking at beam momentum per nucleon of 150 GeV/c and higher is nominally 1.5 T in the first magnet and 1.1 T in the second magnet. When the beam momentum is lower, the magnetic fields are proportionally reduced while keeping the ratio between them constant. This procedure is performed to optimize the geometrical acceptance of the detector for a given reaction. The magnetic field inhomogeneities at the VTPCs' edges are taken into account by using an appropriate magnetic field map in the NA61/SHINE tracking and reconstruction software. The orientation of the magnetic field along the y axis, pointing down, causes the bending of the particles' trajectories depending on their charge: positively charged particles towards +x direction and negatively charged particles towards -x direction. The TPCs are filled with a gas mixture Ar/CO^2 in proportion 90/10 and 95/5 for VTPCs and MTPCs, respectively. Charged particles reaching the TPCs cause gas ionization. Electrons, which come from the ionization, drift towards the read-out chambers of TPCs thanks to the electric field applied to the gas boxes.

3.2.4 Time-of-Flight detectors

Two Time-of-Flight detectors: ToF-L and ToF-R, were introduced to improve particle identification at mid-rapidity for the top considered energy. Two ToF walls are placed behind the MTPC-L and MTPC-R. Each ToF-L/R wall contains 891 individual, rectangular scintillation detectors with a single photomultiplier tube glued to the short side. The surface area of the Left and Right walls is, in total, 4.4 m^2. The particle's mass squared is obtained by combining the information about the particle's time of flight with the track length and momentum measured in the TPCs. It extends the kinematic region where charged particles are identified. The information from the ToF detector was not used in the analysis presented in this thesis.

beam momentum (A GeV/c)	13	19	30	40	75	150
PSD threshold (mV)	75	135	230	350	325	230
T2 centrality (%)	30	35	30	35	20	23

Table 3.2: Centrality of the ^{40}Ar+^{45}Sc interactions selected by the T2 trigger for different beam momenta [71].

3.2.5 Projectile Spectator Detector

The PSD is placed behind the ToF, and it is the most downstream detector in the experimental setup. It is a hadron calorimeter and it is built from 28 large (with the dimensions: 20×20 cm^2) and 16 small modules (with the dimensions: 10×10 cm^2), each of them consisting of 60 pairs of alternating lead (16 mm) and scintillator (4 mm) tiles sandwiched perpendicular to the beam. The PSD scheme and a single PSD module scheme are presented in Fig. 3.5. It fulfills two roles. First is the determination of the centrality of the collision at the trigger level (T2 trigger; see Tab. 3.2 for the PSD threshold and corresponding centrality selection). Second, is the measurement of projectile spectator energy in nucleus-nucleus collisions for offline centrality calculations (for details on centrality calculations see Sec. 4.2.3). The PSD measurement makes possible the extraction of the number of interacting nucleons from the projectile up to one nucleon precision. The high energy resolution is essential for the fluctuation analysis since it allows for a precise centrality selection of the most valuable events.

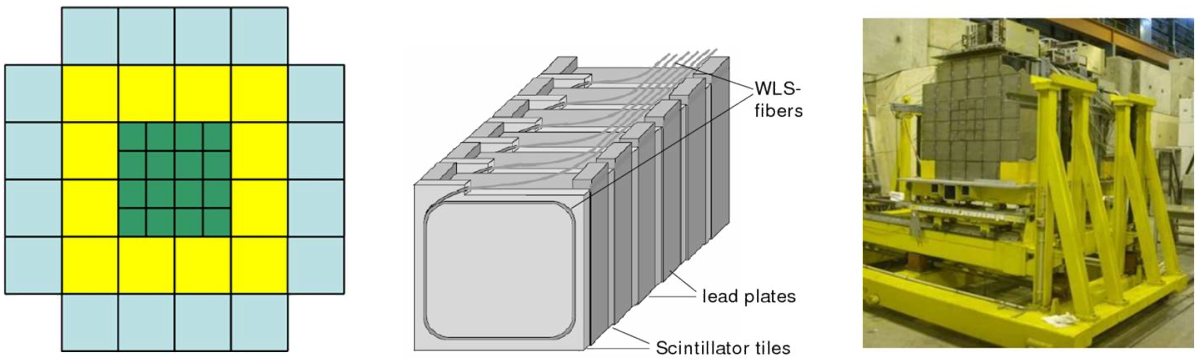

Figure 3.5: Left: PSD front scheme, middle: single module scheme, right: photo of the PSD [65].

3.2.6 Data reconstruction and calibration

Data reconstruction and calibration are crucial steps for obtaining good-quality data. It consists of several steps which lead to storing the measured data, called the *raw data*, into the format suitable for further analysis. The following steps are applied in the reconstruction procedure:

1) Beam position reconstruction
   It is based on the information from three BPDs along the beamline. The BPDs store the position of the beam particles and a dedicated algorithm is used to fit them with a straight line, marking the trajectory of the beam.
2) Track reconstruction

Track reconstruction is based on the information from VTPCs and MTPCs. The first step is searching for signals in TPC pads and *time slices* (*time slice* is defined as the charge collection window resulting from the sampling frequency of the TPC and is equal $t \simeq d/v_D$, where "d" is the length of the drift volume in *y* coordinate and "v_D" is the electron drift velocity). Signals in the adjacent pads and *time slices* are grouped in clusters. The clusters positions and their total charge are saved for the tracking procedure. First, local tracking is performed. The algorithm merges clusters into local track fragments in each TPC, taking into account their spatial proximity and the presence of the magnetic field. Finally, the global tracking is performed and the local track fragments are merged into global tracks which are recorded.

3) Vertices reconstruction
   The goal of the vertices reconstruction is to determine the position of the Primary Vertex (vertex of the beam-target interaction) and the secondary vertices usually resulting from weak decays of hadrons. During the Primary Vertex fitting procedure, the beam trajectory is extrapolated to the target plane, providing *x* and *y* coordinates of the Primary Vertex. Then, the global tracks are extrapolated to the target plane. The quality of the Primary Vertex fitting procedure and the type of vertex is stored in the flags.
4) PSD reconstruction
   The signals recorded by the PSD are reconstructed into energy deposits in single modules, sections, and finally in the whole PSD.

Such processed data are stored in the format of events with all information necessary for the data analysis, such as trigger configuration, beam position, PSD energy deposit, and the list of tracks. Each track entry contains information about momentum, charge, energy loss, and the number of clusters in each TPC.

3.2.7 Monte Carlo simulations

The Monte Carlo (MC) simulation is necessary for the correction of the analysis results. The corrections (for details see Sec. 4.3) include various effects such as the detector and the reconstruction efficiency. Different models are available, however, EPOS1.99 [72, 73] offers the best agreement with the NA61/SHINE experimental data [74]. Thus it was chosen for the correction procedure in this study. The Monte Carlo production chain in NA61/SHINE consists of three parts.

1) Simulation of the collisions with the chosen model and storing the output in the *.hepmc* [75] format.
2) Propagation of the simulated particles through the NA61/SHINE detector. The detailed detector description is done within GEANT4 [76] ver. 10.7.0 framework and integrated with the NA61/SHINE software so the output produced is in a format identical to the raw, measured data.
3) Reconstruction of the simulated data using exactly the same algorithms as in the recon-

struction of the data recorded by the detector.

Such constructed MC simulation chain allows obtaining two types of events essential for further correction procedure:

- pure events (sim): events originated from the MC generator, not distorted by the detector and algorithm imperfections,
- reconstructed events (rec): events processed by the GEANT4 simulation of the detector and reconstructed by the NA61/SHINE algorithms.

Chapter 4

Analysis

The goal of the analysis was to measure the fluctuations of the multiplicity and net-charge of the primary charged hadrons produced in the strong interactions and the electromagnetic decays in the 1% most central ^{40}Ar+^{45}Sc collisions within the NA61/SHINE detector acceptance defined by the $p_T - y - \phi$[(a)] region of the high-resolution of the detector.
The analysis procedure contained the following steps:

- the data selection according to event and track selection criteria (described in Sec. 4.2) to ensure the best possible quality of the data,
- evaluation of the charged hadron multiplicity and net-charge distributions,
- correction of the charged hadron multiplicity and net-charge distributions via the *Unfolding* method,
- calculation of the fluctuation measures from the corrected distributions,
- estimation of the systematic uncertainties of the results,
- estimation of the statistical uncertainties of the results.

4.1 Data and Monte Carlo

The study is based on ^{40}Ar+^{45}Sc interactions at beam momenta equal 13*A*, 19*A*, 30*A*, 40*A*, 75*A*, and 150*A* GeV/*c*, taken by the NA61/SHINE experiment in 2015. The detector setup and the beam origin were discussed in Chap. 3. The Monte Carlo simulations were produced using the same reconstruction chain as the data. The initial statistics of the data and MC at each beam momentum are summarised in Tab. 4.1.

4.2 Event and track selection criteria

To ensure the best possible quality of the data for further analysis, the event and track selection was performed using criteria that were optimized for each beam momenta separately. The quality of the data may be distorted by several phenomena like detector malfunction, off-time interactions, bad tracks or vertex reconstruction quality.

[(a)] ϕ stands for the azimuthal angle and is defined as $\phi = \arctan \frac{p_y}{p_x}$, where p_x and p_y are momenta of the particle along the *x* and *y* axis (axes perpendicular to the beam direction) respectively.

p_{beam} (GeV/c)	$\sqrt{s_{NN}}$ (GeV)	initial event statistics	
		data	MC
13A	5.1	$3.8 \cdot 10^6$	$19.2 \cdot 10^6$
19A	6.1	$3.9 \cdot 10^6$	$19.6 \cdot 10^6$
30A	7.6	$5.1 \cdot 10^6$	$19.6 \cdot 10^6$
40A	8.8	$9.7 \cdot 10^6$	$19.5 \cdot 10^6$
75A	11.9	$4.7 \cdot 10^6$	$19.5 \cdot 10^6$
150A	16.8	$3.5 \cdot 10^6$	$19.8 \cdot 10^6$

Table 4.1: Initial statistics of the data and MC in the ^{40}Ar+^{45}Sc collisions at different beam momenta.

4.2.1 Event selection

For further analysis, only events which have met the following criteria were considered:

a) absence of detector malfunctions or faulty detector parameters,

b) events were preselected by the hardware central interaction trigger T2, which was set on the sixteen small PSD modules and accepts ~ 30% of the most central interactions, i.e. with the lowest forward energy (see Tab. 3.2),

c) no off-time beam particles were detected within a time window of ±4 µs around the trigger particle (this cut is later called "WFA beam"), see example Fig. 4.1, and no interactions were detected within a time window of ±25 µs around the trigger particle,

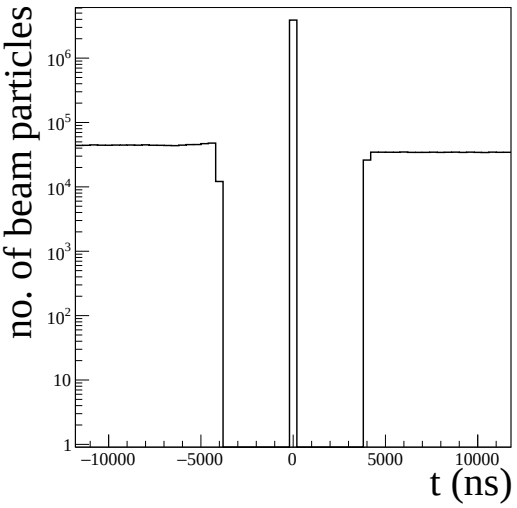

Figure 4.1: Time difference between the beam particle passing through the S1 counter and the triggering signal in ^{40}Ar+^{45}Sc interactions at 30A GeV/c.

d) the signal in BPD-1 or in BPD-2 together with the signal in BPD-3 was required to allow the precise measurement of the beam particle trajectory,

e) the z position of a well-reconstructed Primary Vertex (fitted using the beam trajectory and TPC tracks) lies not farther away than 8 cm from the center of the Sc target (see Fig. 4.2),

f) BPD-3 signal in x and y planes stays within limits to preserve the Gaussian-like shape of the signal (see Fig. 4.3),

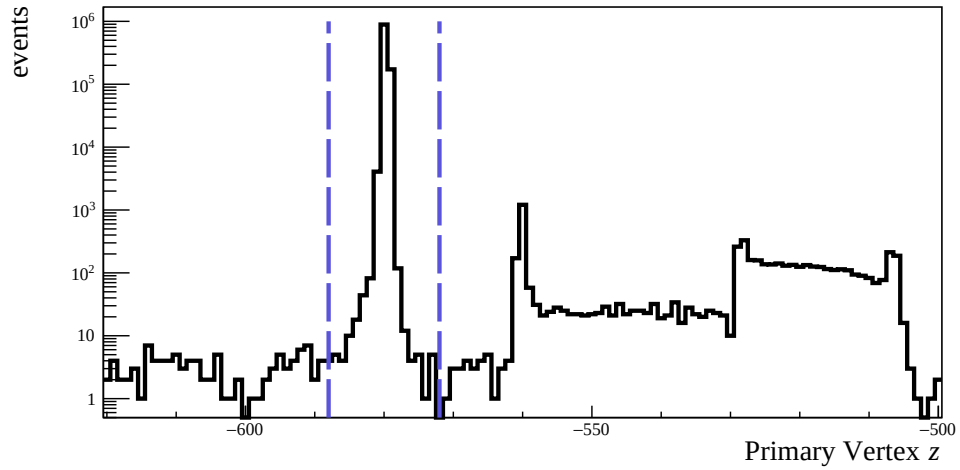

Figure 4.2: Distribution of the z coordinate of the fitted Primary Vertex for T2 triggered events of ^{40}Ar+^{45}Sc interactions at 150A GeV/c. Vertical dashed lines indicate the z region selected for the analysis. The z position of the center of the target is equal to -580 cm.

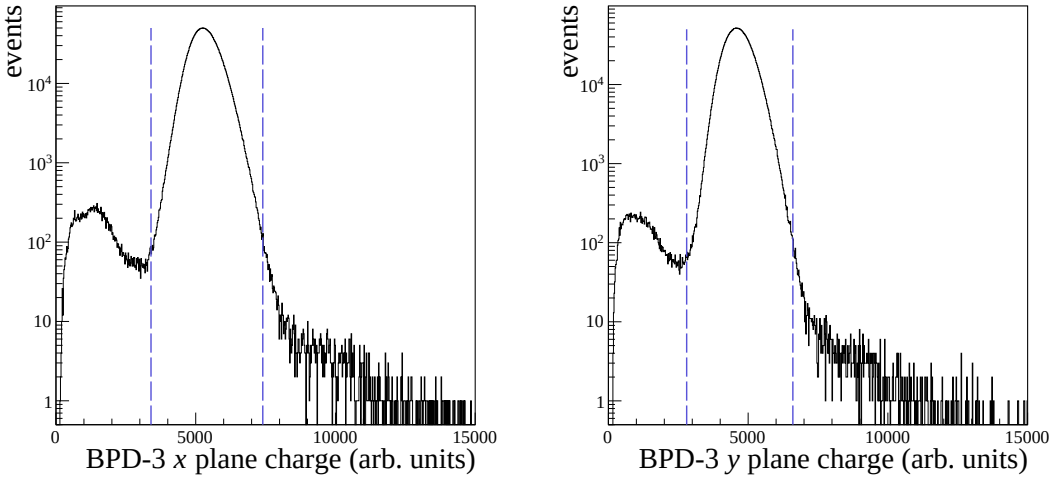

Figure 4.3: Distributions of the charge deposited in BPD-3 in x plane (left) and y plane (right) in T2 triggered events of ^{40}Ar+^{45}Sc interactions at 30A GeV/c. The area between the vertical dashed lines indicates the accepted events.

g) the sum of the energy deposited in 16 small PSD modules have to be smaller than approximately half of the beam energy $E_{PSDsmall} < 0.5 \cdot E_{beam}$ (the values of the cuts are determined for each beam momentum separately) to remove the events distorted by the PSD malfunction; see example plot in Fig. 4.4,

h) the sum of the energy deposited in 28 large PSD modules have to stay within limits (the values of the limits are determined for each beam momentum separately) to remove the events distorted by the PSD malfunction; see example plot in Fig. 4.4,

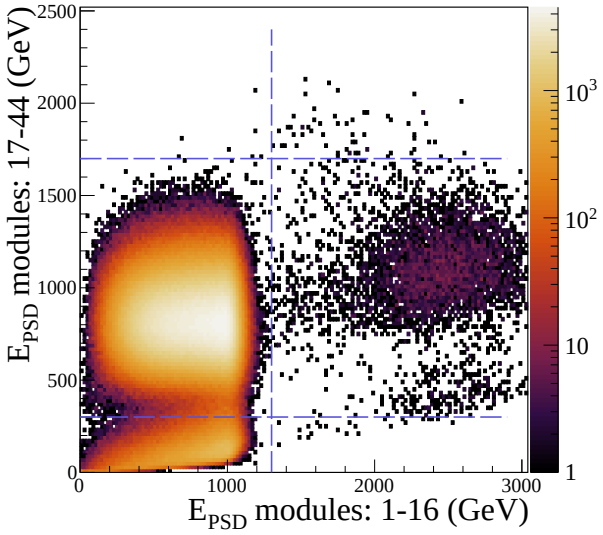

Figure 4.4: Distribution of energy deposited in 16 small modules of PSD (x axis) and energy deposited in 28 large modules of PSD (y axis) for T2 triggered events of ^{40}Ar+^{45}Sc interactions at 75A GeV/c. The area between the top and bottom horizontal dashed lines and on the left of the vertical dashed line shows the accepted events.

i) events with a small ratio of Main Vertex[(b)] tracks (tracks beginning in the Main Vertex) to all reconstructed tracks were removed (the value of the ratio is determined for each beam momentum separately); see example plot in Fig. 4.5,

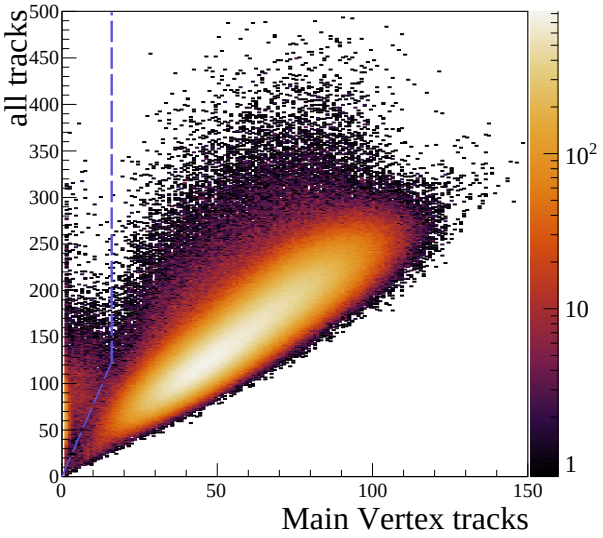

Figure 4.5: The distribution of the Main Vertex tracks (x axis) and all tracks in the event (y axis) for T2 triggered events of ^{40}Ar+^{45}Sc interactions at 40A GeV/c. The area on the right side of the dashed line shows the accepted events.

[(b)]The Primary Vertex is fitted with several algorithms and the Primary Vertex with the best fit quality is marked as the Main Vertex.

j) in less central events (ADC value of S5 > 80), the number of Main Vertex tracks should be anticorrelated with the energy deposited in PSD (the value of the limits is determined for each beam momentum separately); events removed with this procedure may be the events where the spectator interacted with S5 before they reached PSD (see Fig. 4.6),

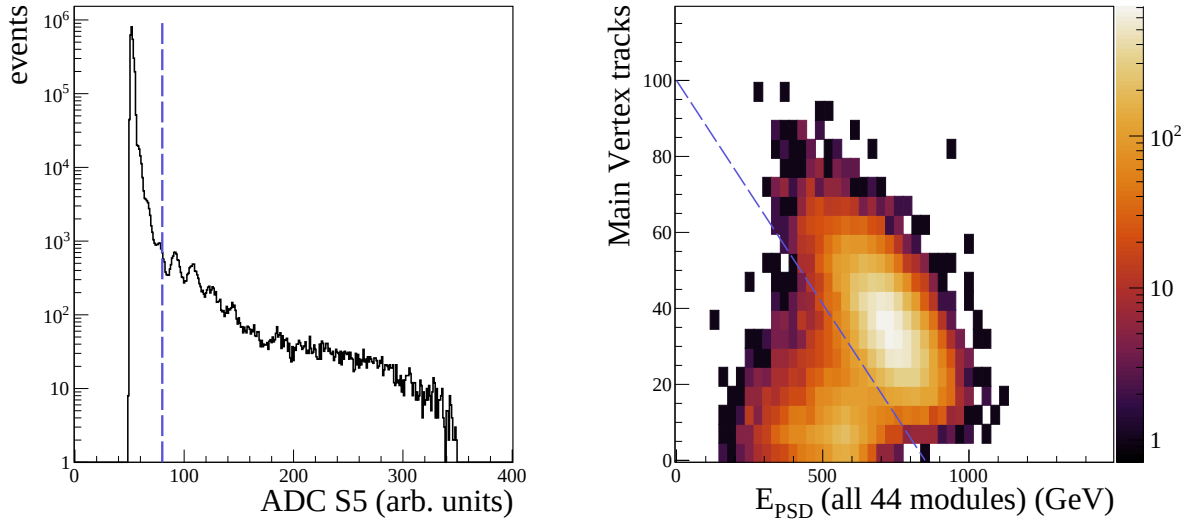

Figure 4.6: Distribution of ADC signal from S5 counter (left plot) and the Main Vertex tracks vs. energy measured in all PSD modules for $S5_{ADC} > 80$ (right plot) for T2 triggered events of ^{40}Ar+^{45}Sc interactions at 30A GeV/c. The area above the dashed line in the right plot shows the accepted events.

k) selection of the 1% most central collisions based on E_{PSD} (for detailed centrality selection procedure, see Section 4.2.3).

The numbers of events that remained for further analysis are listed in Table. 4.2.

beam momentum (A GeV/c)	13	19	30	40	75	150
no. of recorded T2 events	$2.5{\cdot}10^6$	$2.9{\cdot}10^6$	$4.1{\cdot}10^6$	$6.4{\cdot}10^6$	$3.1{\cdot}10^6$	$1.3{\cdot}10^6$
no. af accepted T2 events	$1.5{\cdot}10^6$	$1.8{\cdot}10^6$	$2.7{\cdot}10^6$	$4.5{\cdot}10^6$	$2.2{\cdot}10^6$	$1.1{\cdot}10^6$
no. of the 1% most central events	49649	52408	91360	129584	116000	46454

Table 4.2: Numbers of T2 events that passed the event selection criteria for each beam momentum.

4.2.2 Track selection

The primary charged hadron distributions are the subject of interest, so the track selection has been made to minimize the contamination of tracks from secondary and off-time interactions and from weak decays. The following criteria have been applied:

a) the track momentum fit at the Main Vertex should have converged,

b) tracks with a charge equal to zero were removed,

c) the total number of reconstructed points (later called "TPCs points") on the track should be greater than 30,

d) the sum of the number of reconstructed points in VTPC-1 and VTPC-2 (later called "VTPCs points") should be greater than 15,

e) the distance between the track extrapolated to the interaction plane and the interaction point (impact parameter) should be smaller than 4 cm in the horizontal (bending) plane (Bx) and 2 cm in the vertical (drift) plane (By); see example distributions in Fig. 4.7,

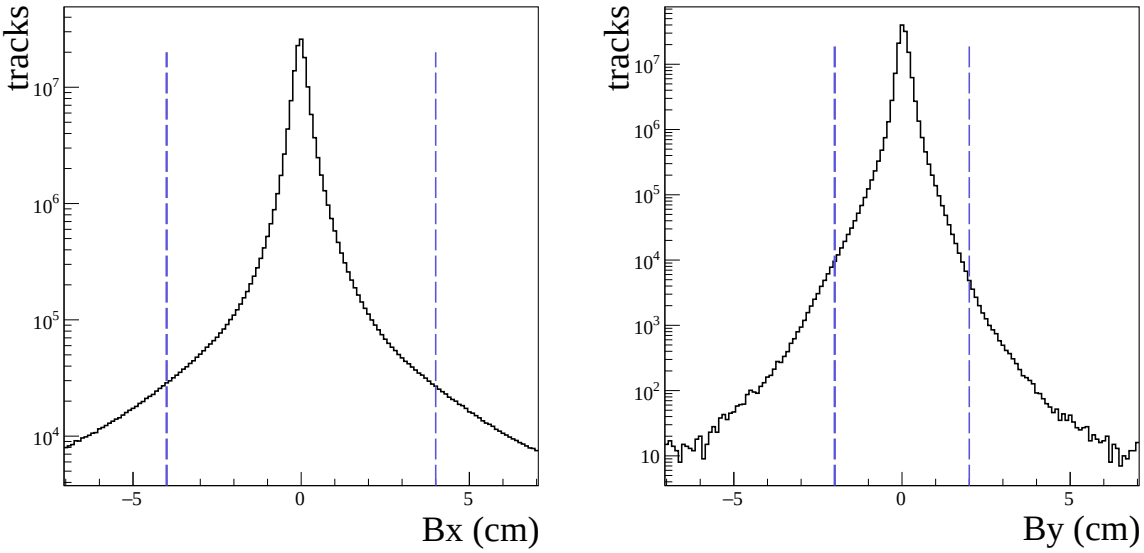

Figure 4.7: Distribution of the impact parameter in the horizontal plane (left plot) and the vertical plane (right plot) for T2 triggered events after event selection (excluding centrality selection) of ^{40}Ar+^{45}Sc interactions at 150A GeV/c. Vertical lines show the accepted track selection.

f) tracks with the particle energy loss dE/dx in the TPCs characteristic for electrons were excluded,

g) the track values of the transverse momentum (p_T), rapidity (y_π), and azimuthal angle (ϕ) should stay within the acceptance region of the detector [77], see Fig. 4.8.

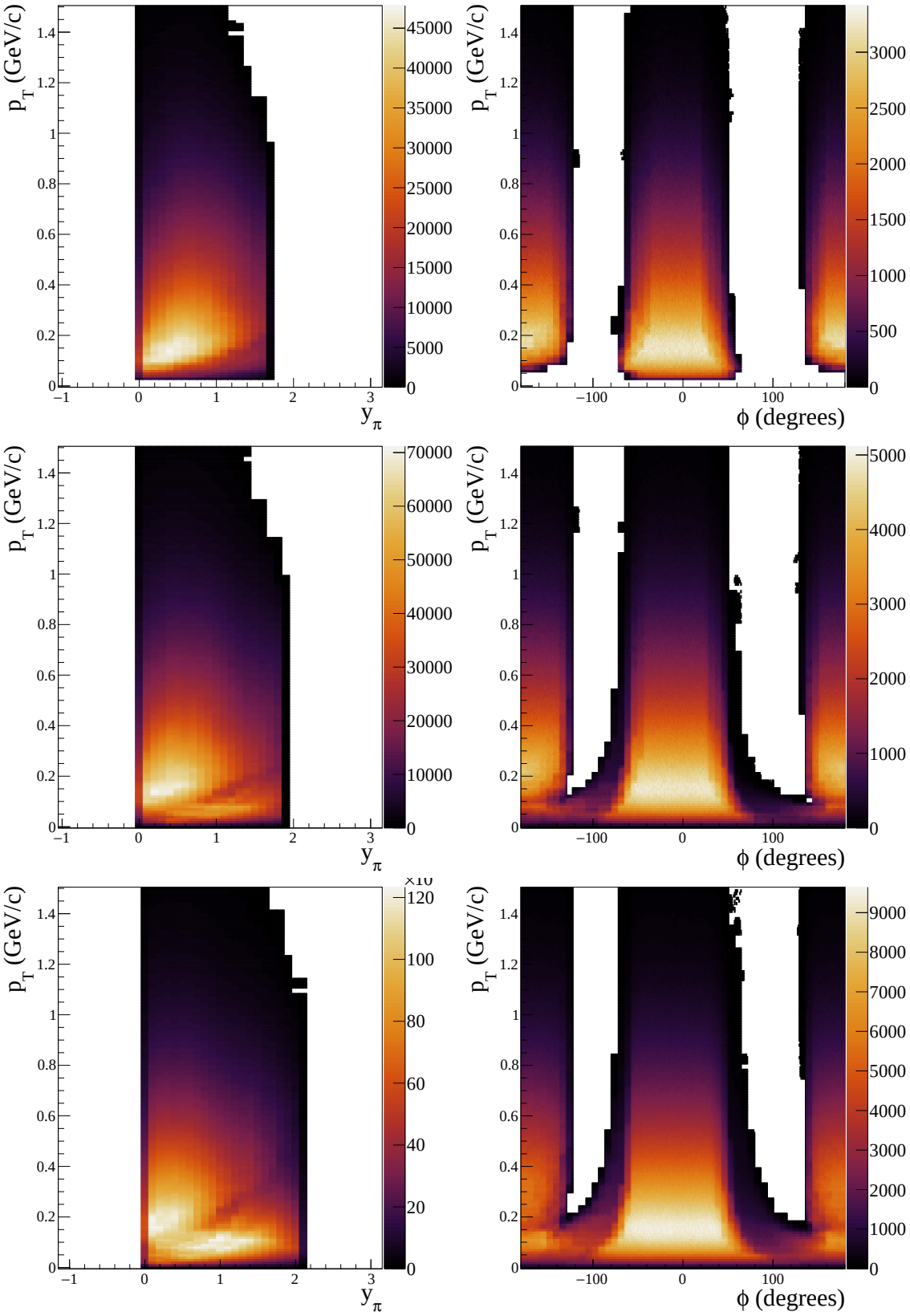

continuation on the next page →

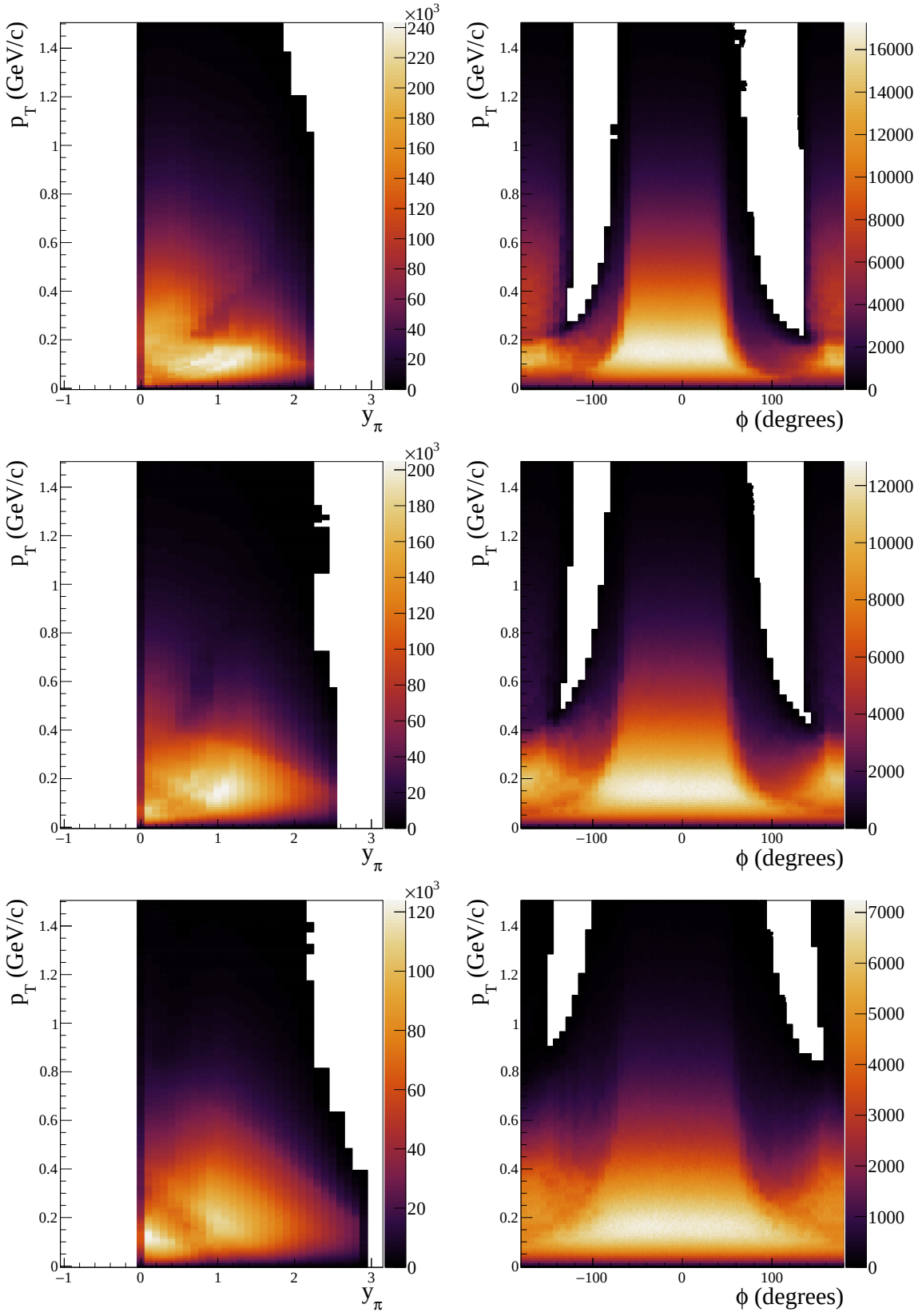

Figure 4.8: Acceptance region of the NA61/SHINE detector in the $p_T - y_\pi - \phi$ phase space in ^{40}Ar+^{45}Sc interactions at beam momenta (from top to bottom): 13*A*, 19*A*, 30*A*, 40*A*, 75*A*, 150*A* GeV/*c*

4.2.3 Centrality selection

Centrality defines the geometry of the collision, the degree of overlaping of two colliding nuclei, and is expressed in percents – the lower percent, the more central the collision. The most direct measure of the centrality of the collision is (1) the impact parameter (b), which is defined as the distance between the centers of the colliding nuclei, or (2) the number of wounded nucleons. Unfortunately, these quantities are not possible to be measured under experimental conditions. The alternative measure of the centrality is the forward energy (E_F) which is defined as the total energy of all particles produced in ^{40}Ar+^{45}Sc collision in the forward rapidity region which is defined by, so-called, PSD acceptance map in Ref. [78]. This measure can be obtained from the model, but it is still not directly available in the experimental data. The value measured by the NA61/SHINE experiment, which corresponds to E_F is the energy measured in PSD (E_{PSD}). To ensure that E_{PSD} is as close as possible to E_F, the E_{PSD} is calculated from a certain subset of PSD modules. The selection of PSD modules is optimized for every beam momenta by examining the correlation between the mean module energy and the total multiplicity of charged particles registered in TPCs. The examples of such correlations are shown in Fig. 4.9. Only those modules which show a negative correlation to the multiplicity are considered further in the E_{PSD} calculation. The PSD can measure both projectile spectators and produced particles energy and the anticorrelation means that mainly the spectators have been measured (high E_{PSD} and low particle multiplicity means non-central collision). This procedure ensures selecting only the modules where the projectile spectators were registered and rejecting modules that caught produced particles. Final module sets are shown in Fig. 4.10.

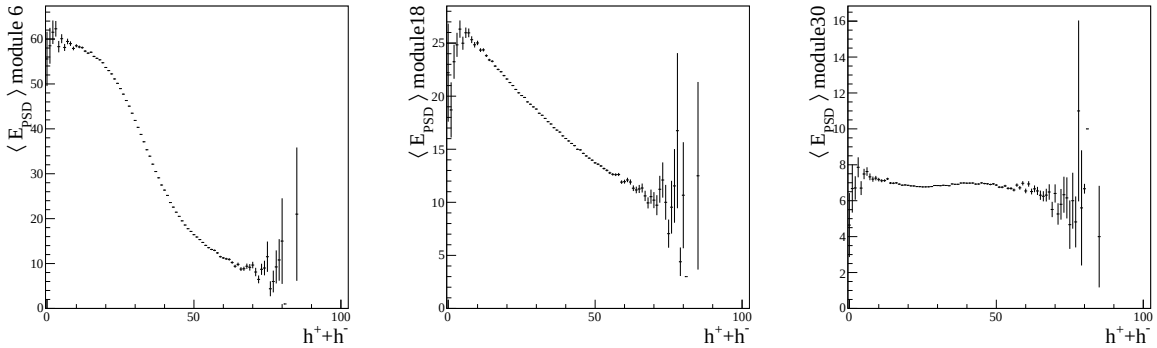

Figure 4.9: Diagrams of mean energy measured by (from the left) the 6th, 18th, and 30th PSD module as the function of total multiplicity of charged particles measured in TPCs in ^{40}Ar+^{45}Sc collisions at 30*A* GeV/*c*. The strong anticorrelation between these two variables is visible in the left and middle plots (modules 6th and 18th), which means those modules will be taken into account during the centrality determination procedure. No correlation is observed in the right plot (module 30th), so this module will be omitted during the centrality determination procedure.

The off-line centrality calculations are performed on the data preselected by the hardware central interaction trigger T2, which was set on the sixteen small PSD modules, and accepts ~30%

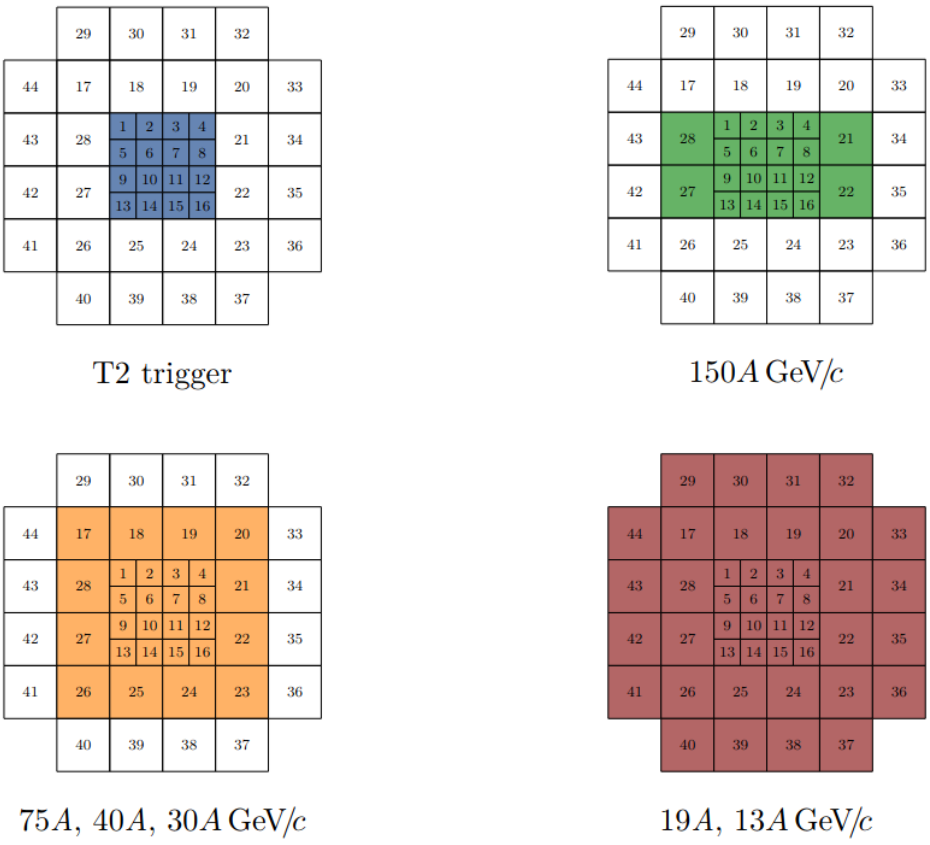

Figure 4.10: Schematic diagrams showing the modules used for the T2 trigger (blue color) and the sets of modules used for the off-line centrality determination at different beam momenta (green, yellow, red color) [45].

most central interactions (these values differ between different beam momenta and are presented in Tab. 3.2). The final module sets used for the off-line centrality determination are presented in Fig. 4.10. The measured E_{PSD} distributions for different beam momenta are shown in Fig. 4.11.

The centrality selection in Monte Carlo simulations was performed using directly E_F or $E_{PSDFast}$. The $E_{PSDFast}$ is the simulated E_F modified by the so-called *PSD Fast Simulator* – the internal, numerical code which incorporates the effects PSD has on the energy measurement: energy leakage, energy smearing, and measurement resolution. It ensures the reproduction of the effect the PSD has on the E_F. Both E_F and $E_{PSDFast}$ are used in the correction procedure to distinguish different event classes.

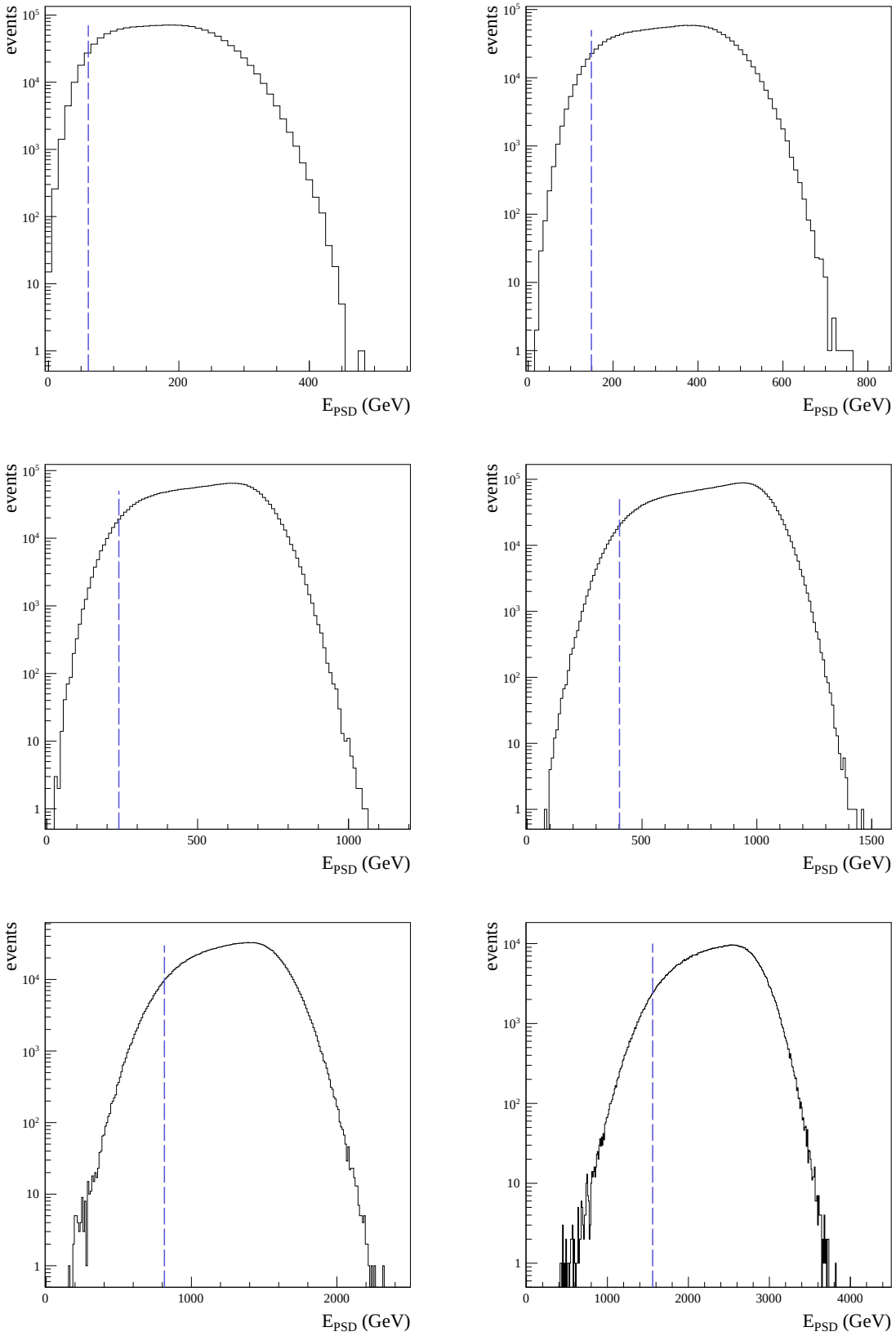

Figure 4.11: Event centrality selection using the energy E_{PSD} measured by the PSD calorimeter. Distributions show measured E_{PSD} for T2 selected events of ^{40}Ar+^{45}Sc interactions at beam momenta (from the left) top: 13*A*, 19*A*, middle: 30*A*, 40*A*, bottom: 75*A*, 150*A* GeV/*c*. The vertical line marks the region with the $0-1\%$ most central ^{40}Ar+^{45}Sc events (the lowest E_{PSD} values).

4.3 Corrections

There are four main phenomena that, if not taken into consideration, may influence the final results of the analyses:

- gain of peripheral events – wrongly reconstructed E_F (peripheral events reconstructed as central events)
- loss of events – imperfect event selection,
- gain of tracks – tracks coming from other events, V0 tracks (from weak decays) reconstructed as Main Vertex tracks,
- loss of tracks – imperfect track selection, reconstruction efficiency.

To correct the data for the above-mentioned effects, the *Unfolding* [79] method was applied. Compared to the widely used *bin-by-bin* weighting correction method [80], *Unfolding* considers the bin migration that allows addressing the phenomena important for the fluctuation analysis. In the analysis, the open access framework *RooUnfold* to apply unfolding was used [79]. There are several correcting algorithms available within the *RooUnfold* itself, and it was decided that *Unfolding* based on the Iterative Bayes' Theorem (*Bayesian Unfolding* [81]) will be most suitable for this analysis. The *Bayesian Unfolding* is the most prominent of *RooUnfold* algorithms which support also multidimensional fitting. To perform the correction procedure, the *Bayesian Unfolding* uses the so-called *Response Matrix* built from Monte Carlo simulated and reconstructed events. In this study, the procedure of corrections was applied to the positively and negatively charged particle multiplicities and net-charge distributions. The *Response Matrices* for all studied quantities are shown in Fig. 4.12.

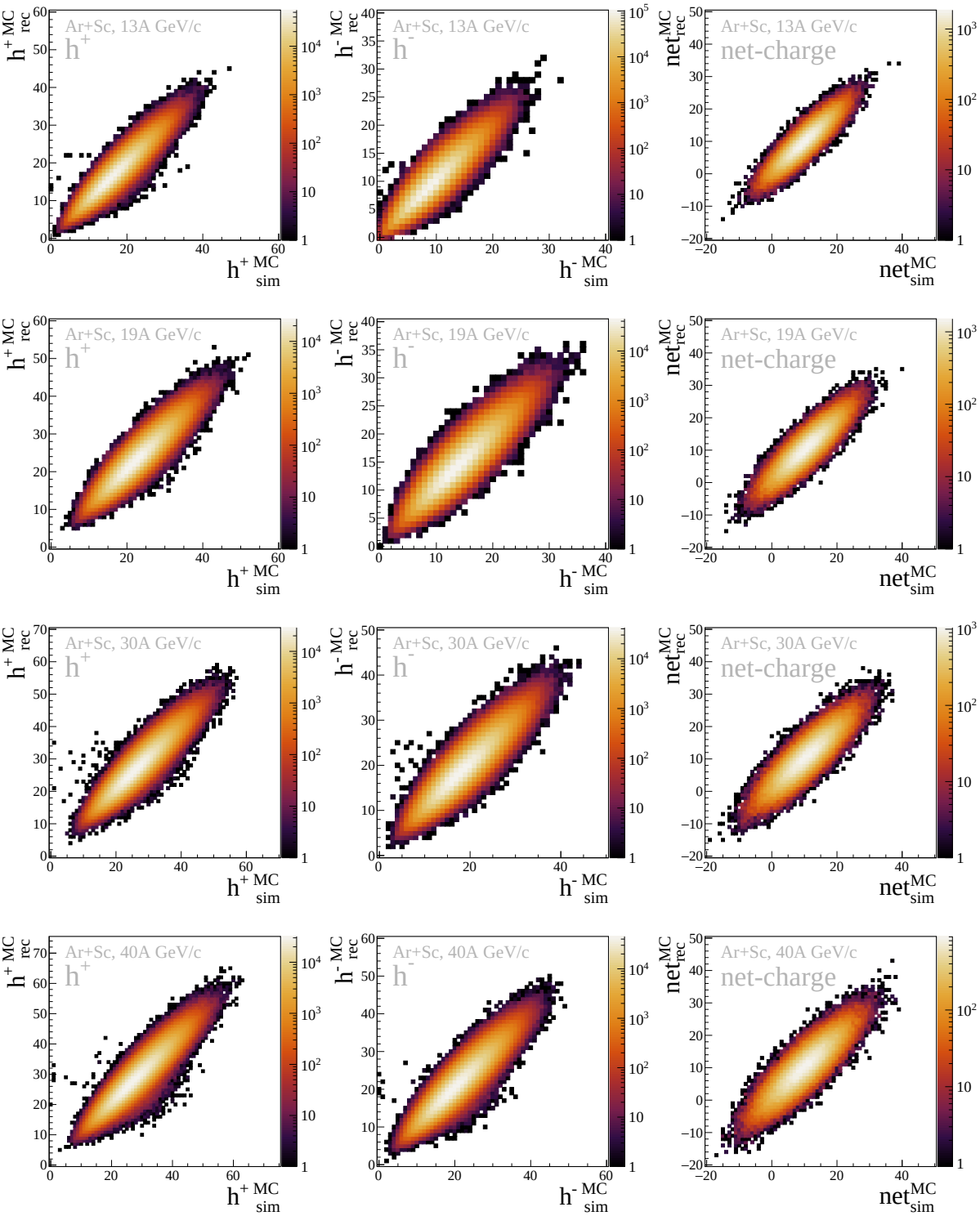

continuation on the next page →

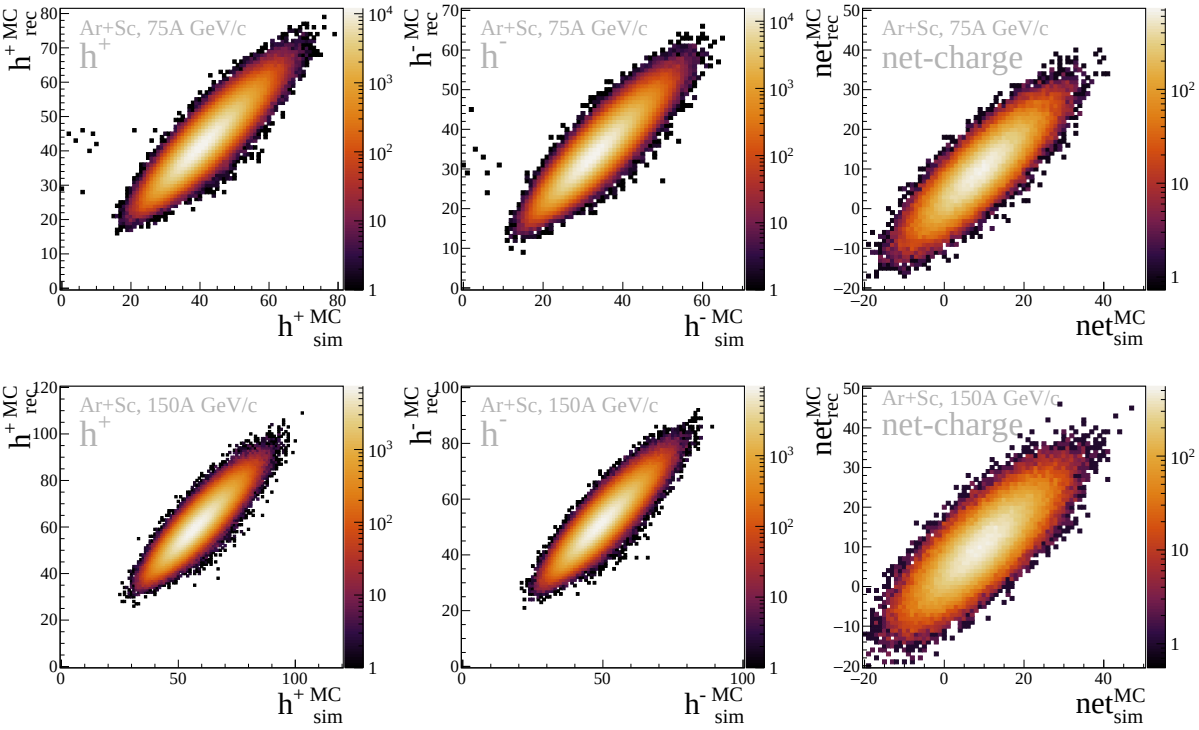

Figure 4.12: *Response Matrices* for positively and negatively charged particle multiplicity and net-charge for ^{40}Ar+^{45}Sc interactions at beam momenta (from the top): 13*A*, 19*A*, 30*A*, 40*A*, 75*A*, 150*A* GeV/*c* and different centrality selection for each beam momentum (listed in Tab. 4.3).

There are three kinds of events considered in the *Unfolding* procedure: **good**, **missed** and **fake** events. Their definition may be different for different experiments and analysis processes. In this study, they are defined as follows:

1) **good**:
   - All inelastic events which have passed event selection (they are properly reconstructed in TPCs) and stay within a predefined centrality bin according to both E_F and $E_{PSDFast}$,
2) **missed**:
   - Events simulated but not reconstructed (due to the event selection),
   - Reconstructed events which stay within predefined centrality bin in E_F but have different centrality in $E_{PSDFast}$,
3) **fake**:
   - Reconstructed events which stay within predefined centrality bin in $E_{PSDFast}$ but have different centrality in E_F.

The example plots showing how the event classes look in the $E_{PSDFast} - E_F$ space are presented in Fig. 4.13.

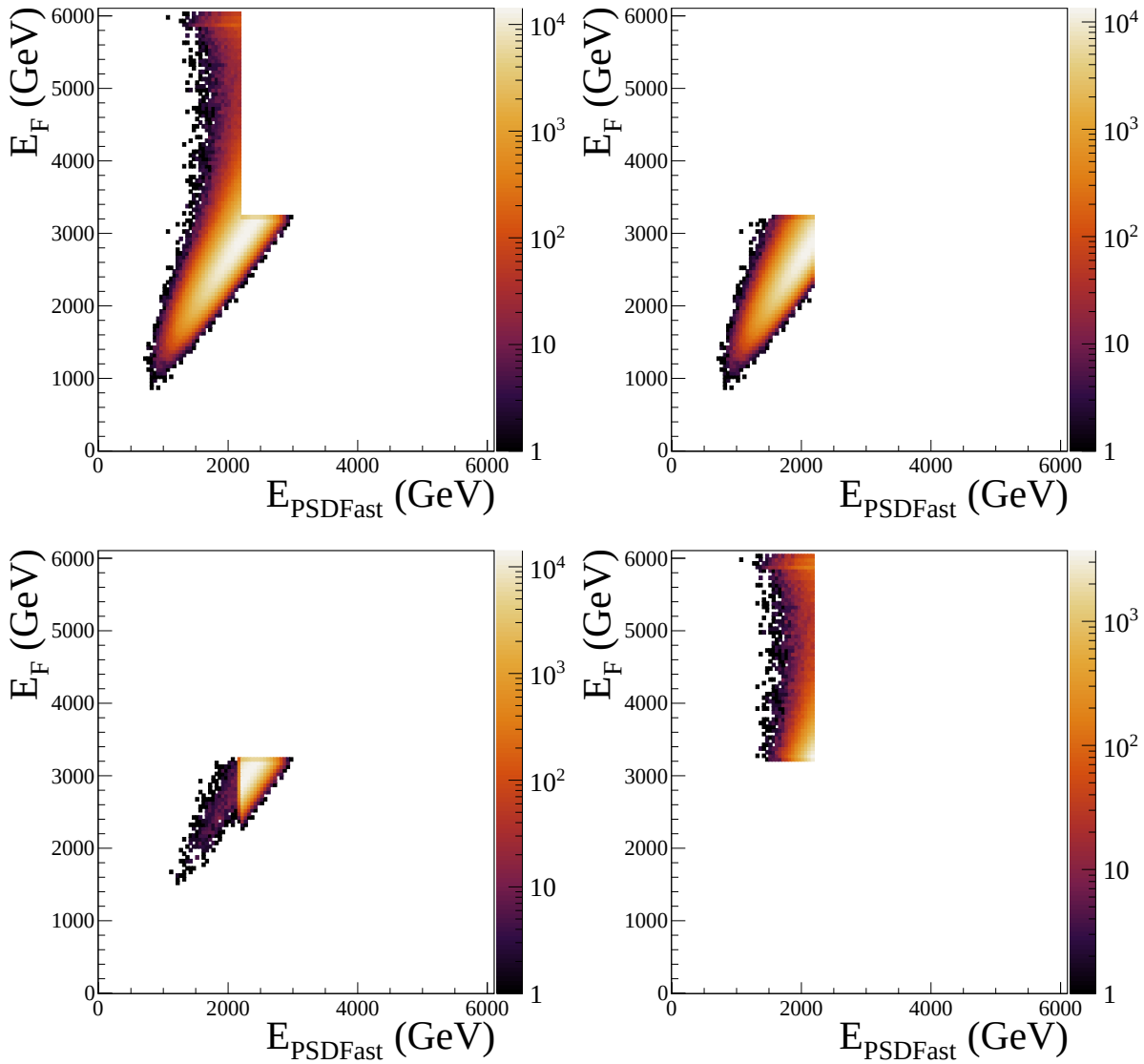

Figure 4.13: Different event classes within 0-10% centrality bin in the simulated ^{40}Ar+^{45}Sc interactions at beam momentum 150A GeV/c in the $E_{PSDFast}$ – E_F space. Top left: all event classes, top right: good events, bottom left: missed events, bottom right: fake events. The sharp cut visible in both E_F and $E_{PSDFast}$ in the top, left plot corresponds to the given centrality selection.

The *Unfolding* procedure needs sufficient statistics of the simulated events, and a Monte Carlo model should contain the data to provide useful results. In other words, the whole data distribution should be fully covered by the distribution of reconstructed Monte Carlo events. Otherwise, the uncovered part will be highly distorted due to the lack of information in the simulated data. Thus, one needs to use a model which describes all possible outcomes. This is why, a separate study at each beam momentum was done to determine the centrality of simulated events which ensures this condition as none of the considered models could cover all data values. The chosen centrality bins for each beam momentum in MC are presented in Tab. 4.3.

The centrality selection only affects the shape of multiplicity histograms, but not the shape of net-charge distribution. The net-charge requires a different approach. Since it is not correlated

beam momentum (A GeV/c)	13	19	30	40	75	150
centrality of Monte Carlo (0-X %)	15	10	10	20	10	10

Table 4.3: Chosen centrality bins of Monte Carlo data used in the *Unfolding* procedure in ^{40}Ar+^{45}Sc interactions at beam momenta: 13A, 19A, 30A, 40A, 75A, 150A GeV/c.

with the centrality of the collision, the distribution should not be unfolded directly. The net-charge corrections should be calculated by the 2D *Unfolding*, using positively and negatively charged particle multiplicities. However, the size of the ^{40}Ar+^{45}Sc system is too large and the procedure of 2D *Unfolding* is not able to converge. Thus, it was decided to use 1D *Unfolding* directly on the net-charge distribution, but with exactly the same centrality selection of the Monte Carlo data as of the measured data, which is 0-1%. Comparison of 1D to 2D *Unfolding* of net-charge was performed on a smaller system, which is p+p, concluding, that the difference between the results obtained via 2D and 1D *Unfolding* is negligible [82]. The distributions of the measured data and the reconstructed Monte Carlo are presented in Fig. 4.14.

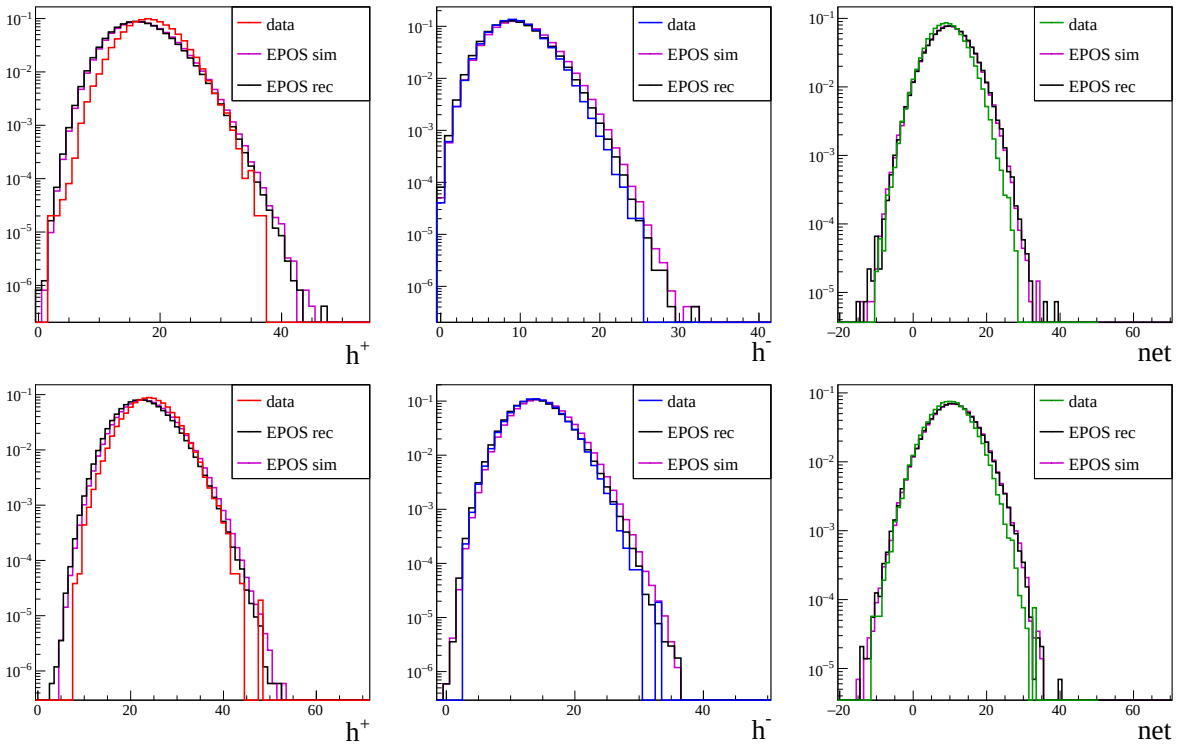

continuation on the next page →

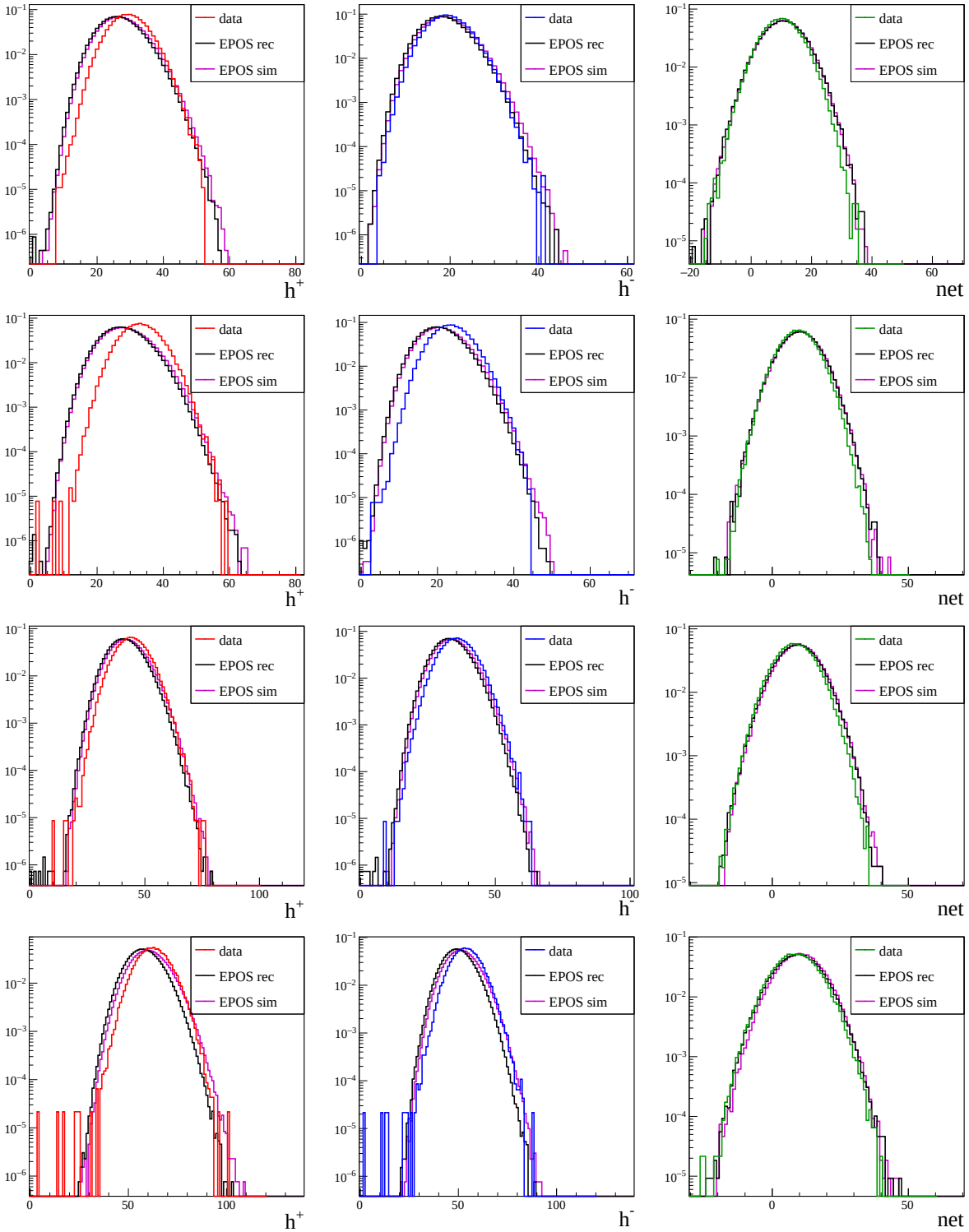

Figure 4.14: Positively (left) and negatively (middle) charged particle multiplicity as well as net-charge (right) distributions in measured data (uncorrected) and reconstructed and simulated Monte Carlo in ^{40}Ar+^{45}Sc interactions at beam momenta (from the top): 13*A*, 19*A*, 30*A*, 40*A*, 75*A*, 150*A* GeV/*c*. The data contains the 0 – 1% most central events while Monte Carlo centrality is selected according to the procedure described above (the values of the centrality cut for Monte Carlo multiplicity distributions are summarised in Tab. 4.3; the centrality selection of the Monte Carlo net-charge is equal to 0 – 1%).

The *Unfolding* procedure requires the specification of the regularisation parameter, which determines the weights put on the data and the Monte Carlo. The value of this parameter should be chosen in such a way as to minimize systematic uncertainty while preserving the small value of statistical uncertainty. In the case of *Bayesian Unfolding*, the regularisation parameter is the number of iterations. For each beam momentum, the number of iterations was studied in order to choose the most optimal one. The fluctuation measures were calculated for the distributions unfolded with a different number of iterations. The final number of iterations was chosen by examining the stability of the fluctuation measures, in other words, a further increase in the number of iterations does not significantly change the value of the quantity. The numbers of iterations for different beam momenta are presented in Tab. 4.4.

beam momentum (A GeV/c)	13	19	30	40	75	150
number of *Unfolding* iterations	80	100	80	90	130	70

Table 4.4: Chosen numbers of iterations in the *Unfolding* procedure for ^{40}Ar+^{45}Sc interactions at beam momenta: 13A, 19A, 30A, 40A, 75A, 150A GeV/c.

The final, corrected distributions of positively and negatively charged particle multiplicities are presented in Chap. 5 in Fig. 5.1. The numerical values of fluctuation quantities introduced in Sec. 2.1 are presented in Tab. 5.1.

4.4 Uncertainties

4.4.1 Statistical uncertainties (σ_{stat})

All experimental measurements, as well as simulated events, suffer from the finite statistics of the data. In this study, the *bootstrap method* [83] was used to estimate statistical uncertainties. This method allows estimating the statistical uncertainty of correlated quantities without dividing the initial data sample into smaller subsamples, which would cause a further decrease in the statistics, or requiring full uncertainty propagation for each quantity separately. The main idea behind the *bootstrap method* is to create M samples (so-called *bootstrap samples*) from the data sample using sampling with replacement: each entry from the data sample can appear in the *bootstrap sample* more than once. The size of each bootstrap sample (distribution of multiplicity or net-charge) is the same as the size of the data sample. The size of the data samples for each collision energy, used in this analysis, is presented in Tab. 4.2.

Several requirements have to be met so *bootstrap method* can be successfully used for the statistical uncertainty estimation:

- the initial data sample has to be a good representation of the whole population;
- the size of the initial data sample has to be large enough to create a significant amount of *bootstrap samples* (since the number of bootstrap samples is restricted by the size of the original sample);

- the events in the initial data sample have to be uncorrelated (this is the reason why the bootstrap samples are first created and then corrected, as the *Unfolding* correction method correlates the events in the sample).

The general algorithm used to calculate statistical uncertainties in this study consists of the following steps:

1) creating the *bootstrap sample* based on the data sample using sampling with replacement: drawing a given quantity from the original sample (e.g. multiplicity) and putting it into the new sample (but without removing the value from the original distribution) and repeating it until the new sample has the same size as the original sample,
2) repeating the first step M times,
3) correcting all M samples with the *Unfolding* method,
4) obtaining the fluctuation measures Q from every corrected distribution and storing the result in a bootstrap distribution,
5) the statistical uncertainty of the final result (e.g. the fluctuation measure Q) is the standard deviation of its bootstrapped distribution (created in the previous step) assuming the bootstrap distribution is close to the normal distribution [84].

The example distributions of κ_2/κ_1, κ_3/κ_2 and κ_4/κ_2 obtained with the bootstrap procedure performed on negatively charged particle multiplicity produced in ^{40}Ar+^{45}Sc collisions at 40*A* GeV/*c* are shown in Fig. 4.15. The standard deviations of those distributions are the final statistical uncertainties (σ_{stat}) of the corresponding quantities.

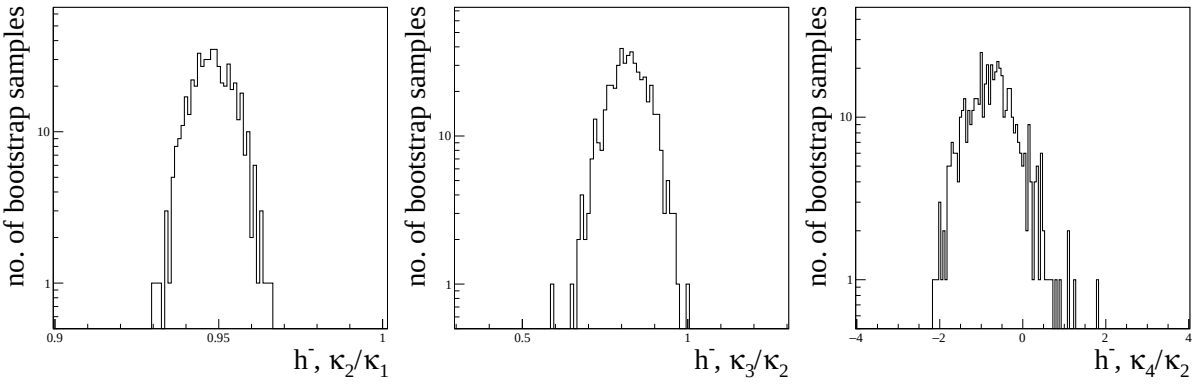

Figure 4.15: The κ_2/κ_1, κ_3/κ_2, and κ_4/κ_2 distributions obtained with the bootstrap procedure performed on negatively charged particle multiplicity produced in ^{40}Ar+^{45}Sc collisions at 40*A* GeV/*c*.

In this study, 500 bootstrap samples of each analyzed quantity (positively and negatively charged particle multiplicities as well as net-charge) at all considered energies were created. Further increase in the number of samples does not significantly change the uncertainty value, as shown in Fig. 4.16. The final values of the σ_{stat} are presented in Tab. 5.1.

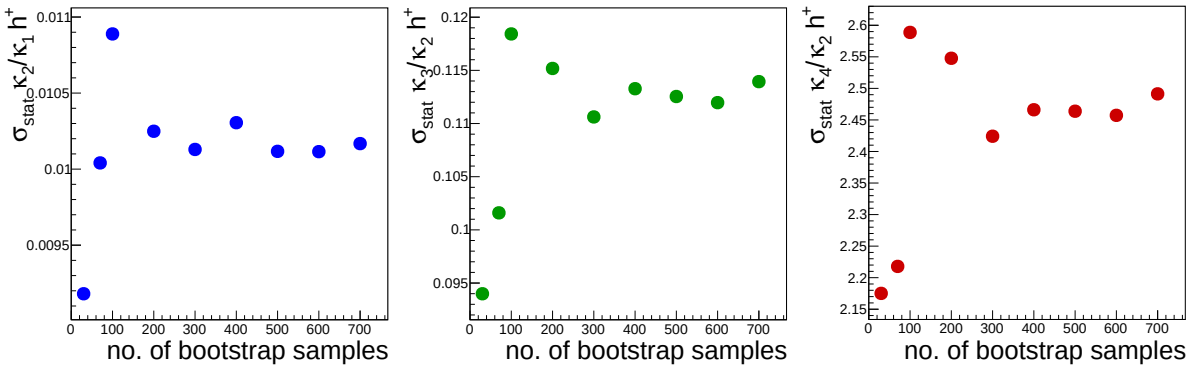

Figure 4.16: The statistical uncertainties of κ_2/κ_1, κ_3/κ_2, and κ_4/κ_2 of positively charged particle multiplicity produced in ^{40}Ar+^{45}Sc collisions at 75A GeV/c calculated for different number of bootstrap samples.

4.4.2 Systematic uncertainties (σ_{syst})

Systematic uncertainties are unavoidable in experimental physics. In such complex devices as particle detectors, many possible sources are biasing the measured signal. Many of those biases can be eliminated by the correction procedure (see Section 4.3), but there are still effects that influence the final results. The size of this influence needs to be included in the systematic uncertainty.

Two sources of systematic uncertainty were considered in this study:

1) the PSD resolution effect (σ_{PSD}) – see Section 4.4.2.1,
2) the stability of the result while varying values of the event and track selection cuts ($\sigma_{\text{tight/loose}}$) – see Section 4.4.2.2.

The final systematic uncertainty can be calculated as:

$$\sigma_{\text{syst}} = \sqrt{\sigma^2_{\text{PSD}} + \sigma^2_{\text{tight/loose}}}\ , \tag{4.1}$$

since those two sources of uncertainty are uncorrelated. The final values of systematic uncertainties for all considered fluctuation measures are presented in Tab. 5.1.

4.4.2.1 PSD resolution effect

The PSD measures the energy of the particles moving in the forward direction and thus, it is used to obtain the centrality of the collision (see Sec. 4.2.3). Based on its measurement, the event may be accepted as $0-1\%$ central or rejected, so changes in the resolution of the PSD can result in the quantity and the quality of the accepted data. To estimate the effect of the resolution on the final results, the resolution of each of the 44 PSD modules was manually modified using the so-called *PSD resolution function* (PRF):

$$\text{PRF}(\text{moduleEnergy}) = \sqrt{\frac{\text{A}^2}{\text{moduleEnergy}} + \text{B}^2 + \frac{\text{C}^2}{\text{moduleEnergy}^2}} \tag{4.2}$$

The PRF value depends on the single PSD module energy and A, B, and C coefficients which are presented in Table 4.5. The coefficients were determined empirically during the PSD cali-

bration process and are stored in the numerical codes for the PSD simulation. The algorithm to

	A ($GeV^{3/2}$)	B (GeV)	C (GeV^2)
small module	0.854	0.026	1.4
large module	0.675	0.038	0

Table 4.5: Values of A, B and C coefficients of the *PSD resolution function*. Values depend on the size of the module.

estimate the PSD resolution effect contribution to the systematic uncertainty is presented below:

1) performing the procedure of the PSD energy modification using the PRF on each PSD module,
2) correcting the modified dataset using *Unfolding* procedure,
3) calculating the fluctuation measure ($Q_{modified}$) using the modified, corrected dataset,
4) calculating the fluctuation measure (Q) using the original (not modified), corrected dataset,
5) calculating the σ_{PSD} as the difference $|Q - Q_{modified}|$.

One should perform the above algorithm for all fluctuation measures. The final values of the σ_{PSD} are presented in Table 4.7.

4.4.2.2 Event and track selection stability

The most optimal event and track selection procedure is used to obtain the final dataset. However, it is still important to estimate how varying the values of the event and track selection cuts affect the results. Two directions of the changes of the event and track selection cuts were studied: loosening (more events accepted) and tightening (fewer events accepted). Among all cuts, five were suitable for performing the tightening/loosening procedure. Different versions of the cuts have been studied and their final version is presented in Table 4.6.

cut	tight	standard	loose
WFA beam	< 5 μs	< 4 μs	< 4 μs
z position of Primary Vertex	(-585,-575) cm	(-588,-572) cm	(-589,-571) cm
TPCs points	> 30	> 30	> 10
VTPCs points	> 15	> 15	> 10
Bx (By)	< 4(2) cm	< 4(2) cm	no cut

Table 4.6: Definitions of tight, standard, and loose cuts in the systematic uncertainty estimation procedure.

To justify certain choices of the values and the applicability of the cuts, the following comments have to be made:

- WFA beam cut (the removal of the off-time beam particles) was not loosened. Studies have shown that loosening WFA cut to the value < 4 μs caused the acceptance of the low E_{PSD}, low multiplicity events which bias the studied multiplicity and net-charge distributions. Those events were produced by the particles coming before the triggering particle, and their presence may be connected with the recovery time of the PSD. See the effect in Fig. 4.17.

This effect disappears at the standard value of the WFA beam cut, so it was decided to keep the standard value while performing the loosening procedure.

- Track selection (TPCs points, VTPCs points, Bx, By) was not tightened. Fluctuation analysis is sensitive to the acceptance change, and the track selection defines the acceptance. The acceptance maps [77], which were used in this study, were prepared using the standard cuts. By using a 'standard' acceptance map in the analysis with tightened track cuts, the tracks which are, in fact, inside the detector acceptance might not be accepted. In the opposite case – loosening the track cuts – there is a possibility that some tracks may be gained due to using the 'standard' acceptance map, but there is no danger that fluctuation signal may be lost due to a change of the acceptance. It was studied that loosening track selection has a minor influence on the size of the overall systematic uncertainty, contrary to tightening the track selection. Thus, it was decided to use standard track selection while performing the tightening procedure.

The procedure was divided into four cases: tightening only event selection (tightEv), loosening only event selection (looseEv), loosening only track selection (looseTr) and loosening both event and track selection (loose). In every case, the fluctuation measure (Q) was calculated, and the next three candidates for systematic uncertainty were considered:

- $\sigma_{\text{tight/loose}} = |Q_{\text{standart}} - Q_{\text{looseTr}}|$,
- $\sigma_{\text{tight/loose}} = |Q_{\text{looseEv}} - Q_{\text{tightEv}}|$,
- $\sigma_{\text{tight/loose}} = |Q_{\text{standart}} - Q_{\text{loose}}|$.

Then, the largest of the considered differences was chosen for the final systematic uncertainty calculation. The final values of $\sigma_{\text{tight/loose}}$ are presented in Table 4.7.

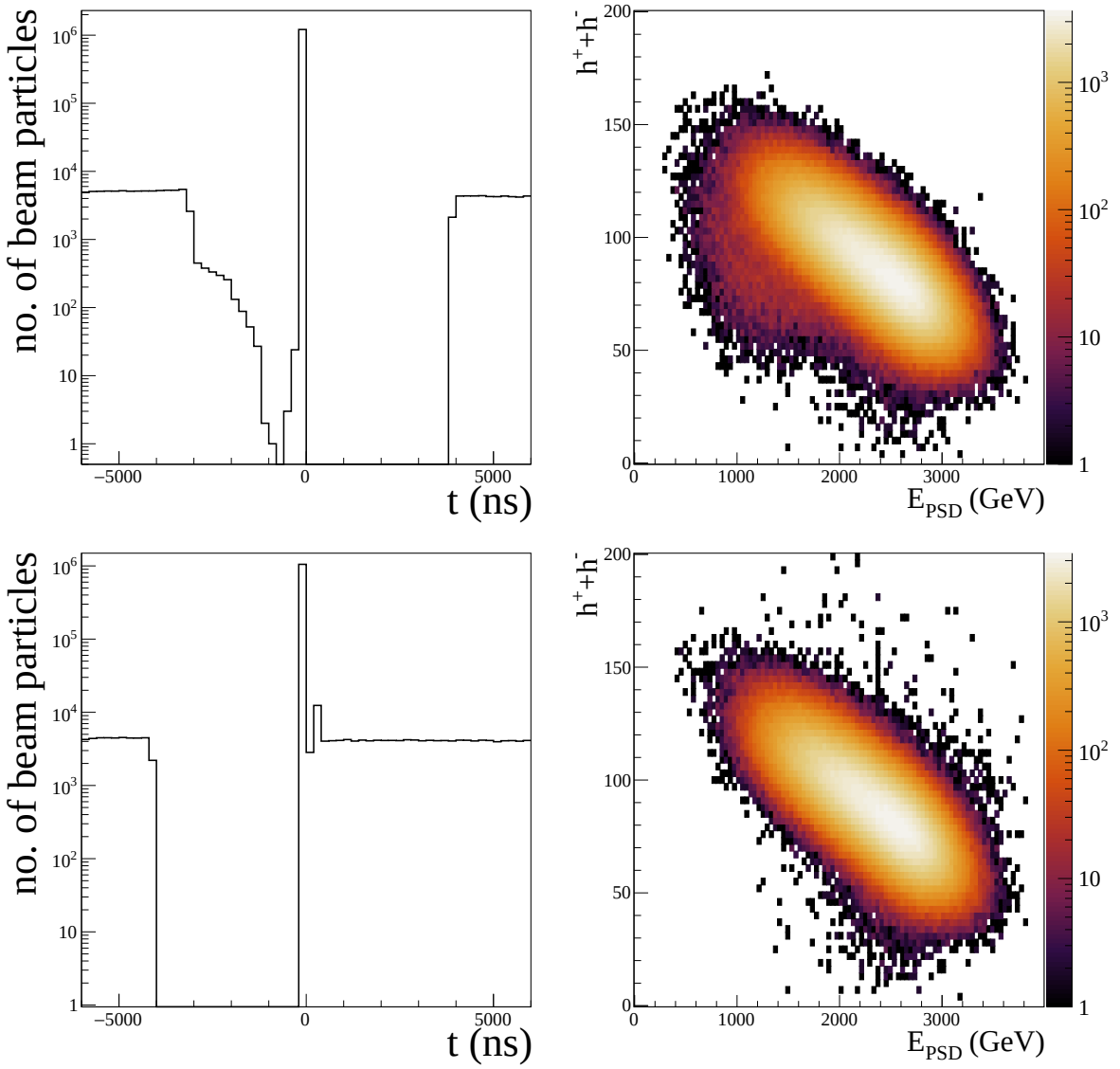

Figure 4.17: (Top, left): The WFA beam trigger times distribution, where particles coming after the triggering particle were cut out and particles coming before the triggering particle were left. (Top, right): The E_{PSD} and charged particle multiplicity distribution after no cut on particles coming before the triggering particles were made. The low multiplicity, low E_{PSD} events are visible. (Bottom, left): The WFA beam trigger times distribution, where particles coming after the triggering particle were left and particles coming before the triggering particle were cut out. (Bottom, right): The E_{PSD} and charge particle multiplicity distribution after no cut on particles coming after the triggering particles were made. No low multiplicity, low E_{PSD} events are present. Plots made for events at beam momentum 150A GeV/c.

beam momentum (A GeV/c)	13	19	30	40	75	150	
$\kappa_2[h^+]/\kappa_1[h^+]$	0.005	0.004	0.010	0.011	0.016	0.020	$\sigma_{\text{tight/loose}}$
	0.003	0.010	0.005	0.012	0.011	0.006	σ_{PSD}
$\kappa_2[h^-]/\kappa_1[h^-]$	0.008	0.005	0.009	0.013	0.013	0.030	$\sigma_{\text{tight/loose}}$
	0.003	0.003	0.008	0.007	0.010	0.006	σ_{PSD}
$\kappa_2[\text{net}]/\kappa_1[\text{net}]$	0.055	0.086	0.105	0.236	0.044	0.176	$\sigma_{\text{tight/loose}}$
	0.002	0.008	0.002	0.024	0.001	0.004	σ_{PSD}
$\kappa_3[h^+]/\kappa_2[h^+]$	0.033	0.062	0.049	0.070	0.026	0.114	$\sigma_{\text{tight/loose}}$
	0.023	0.017	0.026	0.024	0.057	0.020	σ_{PSD}
$\kappa_3[h^-]/\kappa_2[h^-]$	0.010	0.037	0.014	0.036	0.019	0.043	$\sigma_{\text{tight/loose}}$
	0.030	0.061	0.019	0.024	0.062	0.068	σ_{PSD}
$\kappa_3[\text{net}]/\kappa_2[\text{net}]$	0.008	0.067	0.061	0.109	0.051	0.119	$\sigma_{\text{tight/loose}}$
	0.050	0.061	0.007	0.006	0.011	0.012	σ_{PSD}
$\kappa_4[h^+]/\kappa_2[h^+]$	0.091	0.210	1.081	1.727	0.599	5.191	$\sigma_{\text{tight/loose}}$
	0.015	0.199	0.065	0.103	0.351	0.267	σ_{PSD}
$\kappa_4[h^-]/\kappa_2[h^-]$	0.185	0.137	0.514	0.237	0.791	4.135	$\sigma_{\text{tight/loose}}$
	0.011	0.448	0.271	0.002	0.258	0.276	σ_{PSD}
$\kappa_4[\text{net}]/\kappa_2[\text{net}]$	0.854	1.470	0.734	0.269	0.748	1.722	$\sigma_{\text{tight/loose}}$
	0.133	0.824	0.436	0.666	0.119	2.313	σ_{PSD}
$\kappa_2[\text{net}]/(\kappa_1[h^+] + \kappa_1[h^-])$	0.018	0.011	0.007	0.001	0.007	0.019	$\sigma_{\text{tight/loose}}$
	0.001	0.001	0.001	0.004	0.001	0.001	σ_{PSD}
$\kappa_3[\text{net}]/\kappa_1[\text{net}]$	0.028	0.191	0.151	0.359	0.257	0.592	$\sigma_{\text{tight/loose}}$
	0.106	0.154	0.022	0.021	0.058	0.063	σ_{PSD}

Table 4.7: Numerical values of $\sigma_{\text{tight/loose}}$ and σ_{PSD} for κ_2/κ_1, κ_3/κ_2, κ_4/κ_2 for positively and negatively charged particle multiplicity and net-charge, as well as $\kappa_2/(\kappa_1 + \kappa_1)$, κ_3/κ_1 for net-charge in ^{40}Ar+^{45}Sc interactions at 13A, 19A, 30A, 40A, 75A, 150A GeV/c.

Chapter 5

Results and discussion

In this chapter, the results of higher-order moments of the positively and negatively charged particle[(a)] multiplicity, as well as net-charge distributions measured in ^{40}Ar+^{45}Sc interactions at different beam momenta (collision energies), are presented. They are compared with the EPOS1.99 model (in Sec. 5.3) and with other experimental results (in Sec. 5.4).

5.1 Corrected multiplicity and net-charge distributions

In Fig. 5.1, the final, corrected multiplicity distributions of positively and negatively charged hadrons as well as net-charge distributions, are presented.

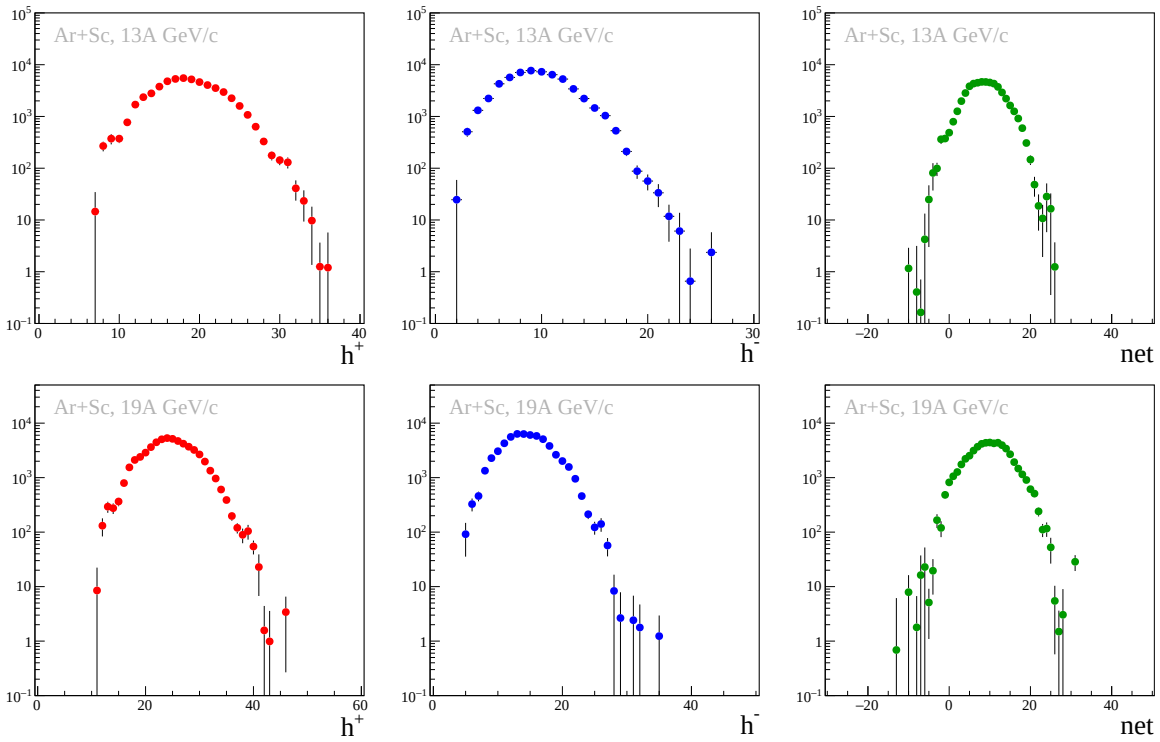

continuation on the next page →

(a) The terms "particles" and "hadrons" are used interchangeably, since all charged particles used for the analysis are hadrons (electrons, which are not hadrons, were removed during the track selection procedure).

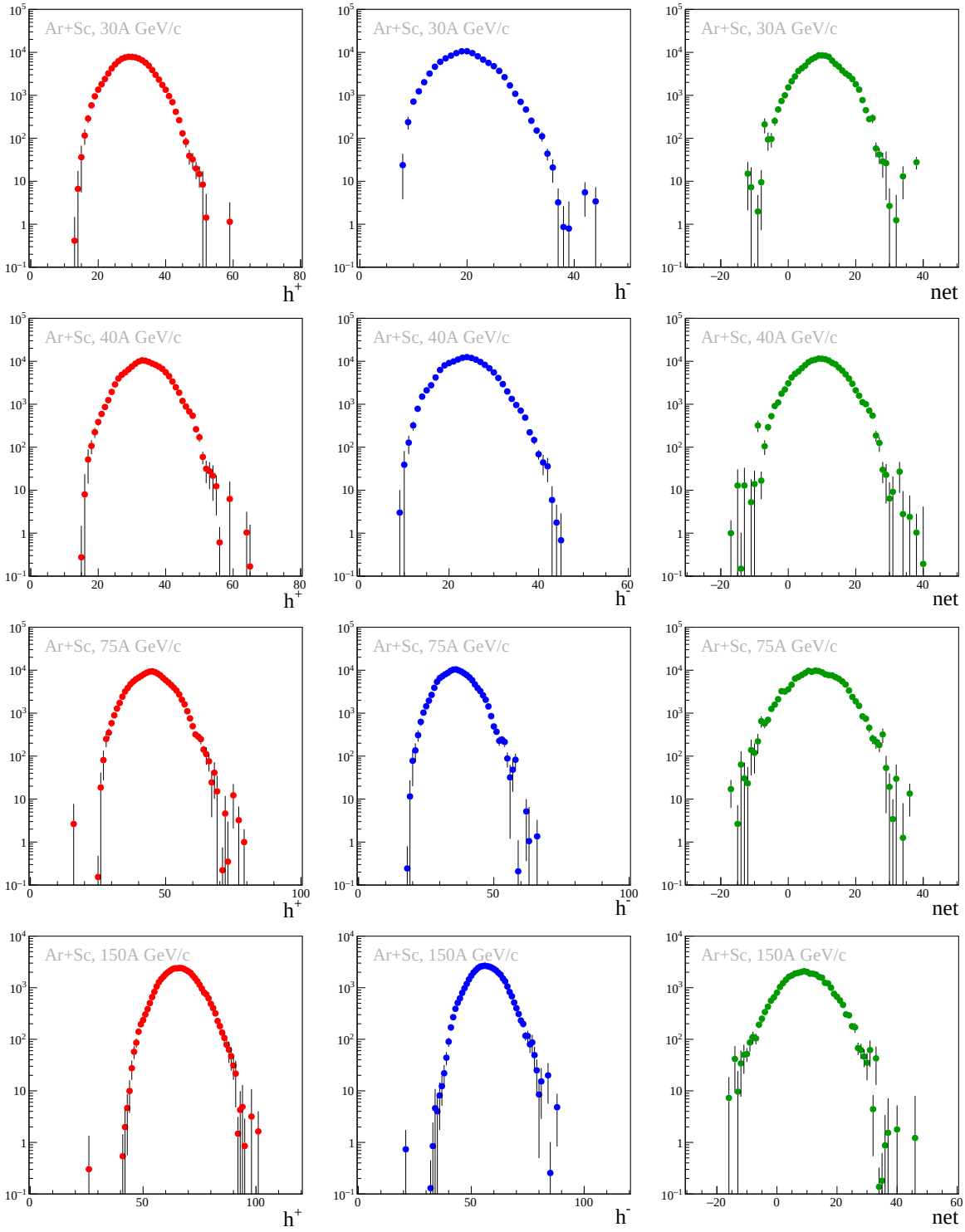

Figure 5.1: Corrected with the *Unfolding* method, positively (left) and negatively (middle) charged particle multiplicity and net-charge (right) distributions in ^{40}Ar+^{45}Sc interactions at beam momenta (from the top): 13*A*, 19*A*, 30*A*, 40*A*, 75*A*, 150*A* GeV/*c*.

5.2 Multiplicity and net-charge fluctuations

The energy dependence of κ_2/κ_1, κ_3/κ_2 and κ_4/κ_2 of multiplicity distribution of positively charged particles in ^{40}Ar+^{45}Sc interactions is shown in Fig. 5.2. The κ_2/κ_1 shows a small deviation from the reference value equal to 1 (Poisson distribution). No non-monotonic behavior within systematic uncertainty is observed. The κ_3/κ_2 increases with the collision energy but stays in the vicinity of the reference value. However, the systematic shift toward lower values is visible at the lower energies. The κ_4/κ_2 does not show non-monotonic behavior but has a negative sign at most energies. The statistical and systematic uncertainties are too large to draw unequivocal conclusions about its behavior.

The energy dependence of κ_2/κ_1, κ_3/κ_2 and κ_4/κ_2 of multiplicity distribution of negatively charged particles in ^{40}Ar+^{45}Sc interactions is shown in Fig. 5.3. Similarly to positively charged particles, the κ_2/κ_1 shows a small systematic deviation from the reference value towards lower values, with a slight decrease toward higher energies being observed. The κ_3/κ_2 oscillates around the reference value. The κ_4/κ_2 shows an indication of a non-monotonic behavior with the sign change, but the systematic and statistical uncertainties are considerable, hindering the interpretation.

The energy dependence of κ_2/κ_1, κ_3/κ_2, κ_4/κ_2, $\kappa_2/(\kappa_1^+ + \kappa_1^-)$, and κ_3/κ_1 of net-charge in ^{40}Ar+^{45}Sc interactions is shown in Fig. 5.4. It needs to be noted, that in net-charge, for the independent particle production, the cumulants of the distributions are defined as $\kappa_{2n} = \kappa_1^+ + \kappa_1^-$ and $\kappa_{2n+1} = \kappa_1^+ - \kappa_1^-$, so the κ_2/κ_1 ratio increases with energy and κ_3/κ_2 decreases with energy. For the net-charge, only the $\kappa_2/(\kappa_1^+ + \kappa_1^-)$, κ_3/κ_1, and κ_4/κ_2 measures are intensive (see Sec. 2.1). Figure 5.4 shows, that in ^{40}Ar+^{45}Sc, κ_2/κ_1 increases with the energy of the collision. The κ_3/κ_2, κ_4/κ_2 and κ_3/κ_1 indicate non-monotonic behaviors with a maximum close to the beam momentum 30A GeV/c ($\sqrt{s_{NN}}$ = 7.6 GeV). However, this effect may be, in fact, smaller taking into account the uncertainties. The κ_4/κ_2 and κ_3/κ_1 oscillate around the reference value, with the reference value staying within the systematic and/or statistical uncertainty in most collision energies. The κ_3/κ_1 and $\kappa_2/(\kappa_1^+ + \kappa_1^-)$ (the net-charge equivalent of κ_2/κ_1) monotonically decrease with the collision energy, staying below the reference value but not changing its sign.

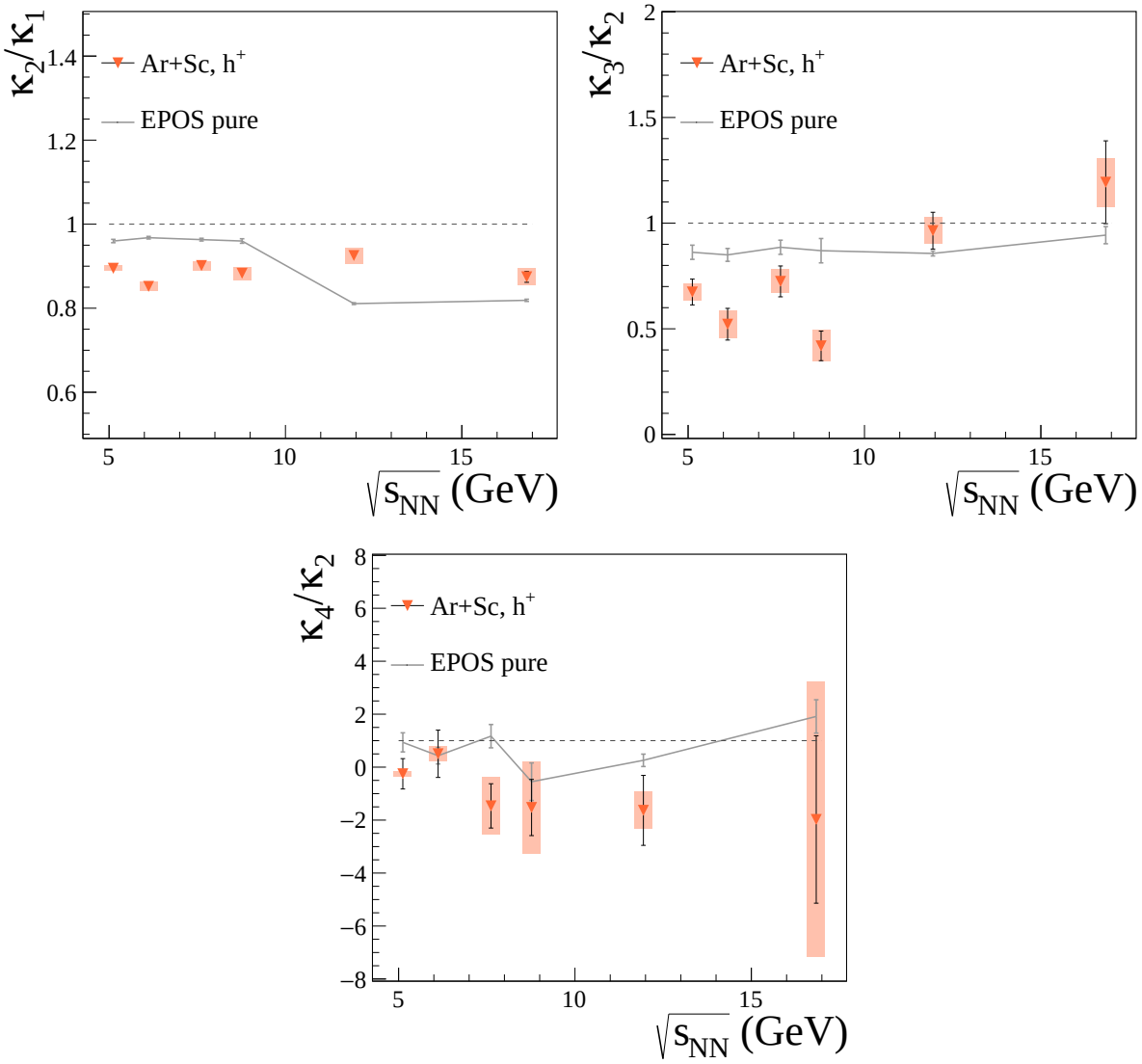

Figure 5.2: Energy dependence of κ_2/κ_1 (top, left), κ_3/κ_2 (top, right) and κ_4/κ_2 (bottom) of positively charged hadron multiplicity in ^{40}Ar+^{45}Sc interactions. The black error bars correspond to statistical uncertainties and the orange bars – systematic uncertainties. The solid lines show the EPOS1.99 model predictions. The line at unity corresponds to the reference value of the Poisson distribution.

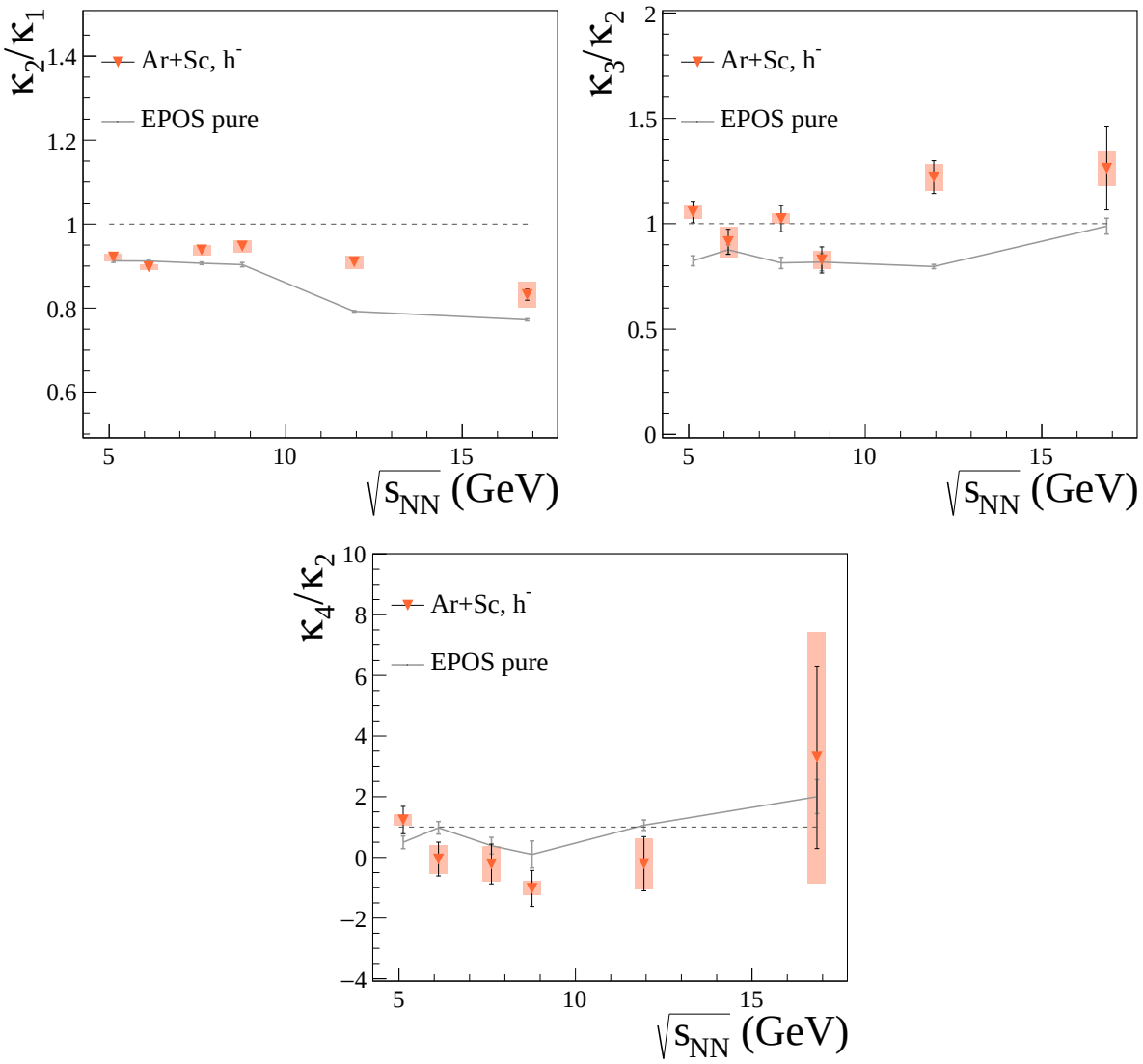

Figure 5.3: Energy dependence of κ_2/κ_1 (top, left), κ_3/κ_2 (top, right) and κ_4/κ_2 (bottom) of negatively charged hadron multiplicity in ^{40}Ar+^{45}Sc interactions. The black error bars correspond to statistical uncertainties and the orange bars – systematic uncertainties. The solid lines show the EPOS1.99 model predictions. The line at unity corresponds to the reference value of the Poisson distribution.

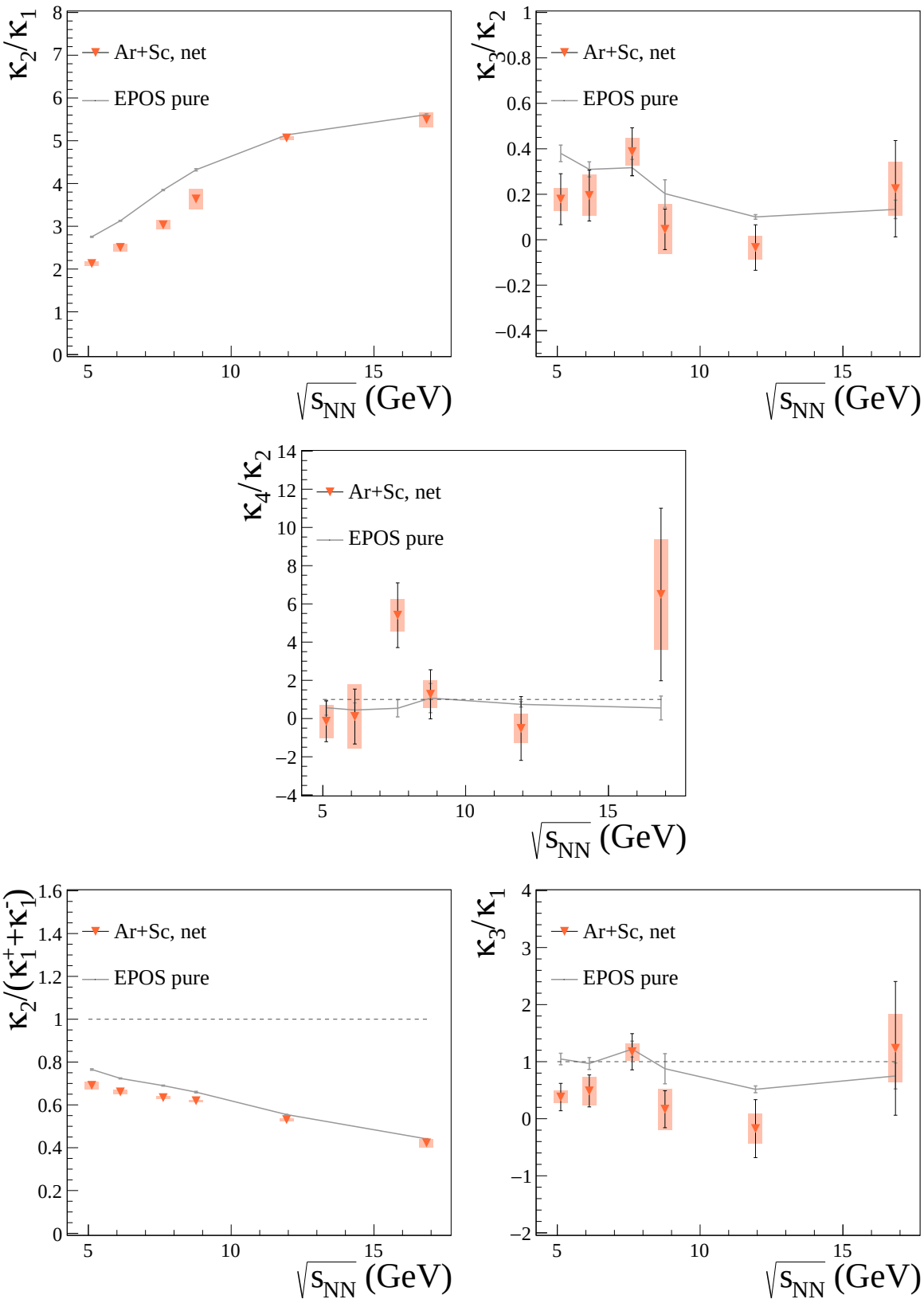

Figure 5.4: Energy dependence of κ_2/κ_1 (top, left), κ_3/κ_2 (top, right) and κ_4/κ_2 (middle) of net-charge distribution in ^{40}Ar+^{45}Sc interactions, as well as energy dependence of $\kappa_2/(\kappa_1^+ + \kappa_1^-)$ (bottom, left) and κ_3/κ_1 (bottom, right) of net-charge distribution in ^{40}Ar+^{45}Sc interactions. The black error bars correspond to statistical uncertainties and the orange bars – systematic uncertainties. The solid lines show the EPOS1.99 model predictions. The line at unity corresponds to the reference value of the Skellam distribution.

5.2.1 Numerical values

The numerical values of higher-order moments of the multiplicity of positively and negatively charged particles and net-charge in ^{40}Ar+^{45}Sc interactions at different beam momenta (collision energies) are presented in Tab. 5.1.

5.3 Comparison with EPOS model

The EPOS [72, 85] stands for:

- **E**nergy conserving quantum mechanical multiple scattering approach, based on
- **P**artons (parton ladders),
- **O**ff-shell remnants, and
- **S**plitting of parton ladders,

and it is a model for the simulation of high-energy nuclear collisions. The core of this approach is simulating individual parton-parton[(b)] interactions taking the inclusive cross section of the reaction as a convolution of two parton distribution functions with an elementary parton-parton cross section obtained from perturbative QCD (pQCD). An elementary scattering is described as a "parton ladder" containing hard (high momentum transfer) and soft (low momentum transfer) scattering processes. The unique feature of the EPOS approach is the treatment of the energy conservation law, which is applied already at the level of computing the interaction partial cross sections. In other words, the total energy has to be shared between all individual elementary interactions.

Used in this thesis EPOS version – EPOS1.99 – was released in 2009 and tuned to the data from SPS, RHIC, and Tevatron. EPOS1.99, so far, describes NA61/SHINE data reasonably well (see for example Refs. [45, 80, 86]).

The EPOS1.99 predictions of charged particle multiplicity and net-charge fluctuations are presented in Figs. 5.2, 5.3, 5.4 with the solid line. The EPOS prediction of κ_2/κ_1 and κ_3/κ_2 of positively charged particle multiplicity is overestimated at lower collision energies and underestimated at higher collision energies. A similar effect of underestimation of the quantities at higher collision energies is observed in κ_2/κ_1 and κ_3/κ_2 of negatively charged particles. However, in this case, EPOS describes them well at lower collision energies. The κ_4/κ_2 is qualitatively well described in both positive and negative charge. Unfortunately, the experimental κ_4/κ_2 results suffer from a lack of precision. For the same reason, it is difficult to say if κ_4/κ_2 of net-charge can be accurately described by EPOS. Overestimation of the quantity at lower collision energies again appears in κ_2/κ_1 of net-charge, but higher collision energies are accurately depicted. Quantitative EPOS description of the data is observed in $\kappa_2/(\kappa_1^+ + \kappa_1^-)$ in net-charge. The net-charge κ_3/κ_1 predicted by EPOS seems to fit the experimental results qualitatively, but again, the lack of experimental precision is a serious obstacle.

[(b)] Parton is any particle constituent within the hadron.

beam momentum (A GeV/c)	13	19	30	40	75	150	
$\kappa_2[h^+]/\kappa_1[h^+]$	0.006	0.011	0.011	0.016	0.019	0.020	σ_{syst}
	0.007	0.007	0.006	0.005	0.007	0.013	σ_{stat}
	0.895	0.852	0.901	0.883	0.925	0.875	result
$\kappa_2[h^-]/\kappa_1[h^-]$	0.009	0.006	0.012	0.014	0.016	0.031	σ_{syst}
	0.009	0.008	0.007	0.006	0.008	0.013	σ_{stat}
	0.921	0.898	0.938	0.947	0.910	0.832	result
$\kappa_2[net]/\kappa_1[net]$	0.055	0.086	0.105	0.237	0.044	0.176	σ_{syst}
	0.026	0.029	0.028	0.028	0.044	0.084	σ_{stat}
	2.128	2.505	3.031	3.638	5.065	5.495	result
$\kappa_3[h^+]/\kappa_2[h^+]$	0.040	0.064	0.055	0.074	0.063	0.116	σ_{syst}
	0.061	0.075	0.073	0.070	0.087	0.196	σ_{stat}
	0.674	0.522	0.724	0.419	0.964	1.194	result
$\kappa_3[h^-]/\kappa_2[h^-]$	0.032	0.071	0.024	0.043	0.064	0.081	σ_{syst}
	0.051	0.059	0.062	0.059	0.078	0.197	σ_{stat}
	1.055	0.914	1.024	0.828	1.221	1.262	result
$\kappa_3[net]/\kappa_2[net]$	0.050	0.091	0.061	0.109	0.052	0.119	σ_{syst}
	0.112	0.112	0.105	0.093	0.100	0.212	σ_{stat}
	0.178	0.195	0.387	0.046	-0.034	0.224	result
$\kappa_4[h^+]/\kappa_2[h^+]$	0.092	0.290	1.083	1.730	0.695	5.198	σ_{syst}
	0.573	0.893	0.836	1.061	1.321	3.161	σ_{stat}
	-0.251	0.504	-1.463	-1.524	-1.632	-1.976	result
$\kappa_4[h^-]/\kappa_2[h^-]$	0.185	0.468	0.581	0.237	0.832	4.145	σ_{syst}
	0.450	0.557	0.655	0.593	0.893	3.008	σ_{stat}
	1.231	-0.055	-0.217	-1.023	-0.209	3.299	result
$\kappa_4[net]/\kappa_2[net]$	0.864	1.686	0.854	0.718	0.757	2.884	σ_{syst}
	1.067	1.436	1.692	1.285	1.669	4.514	σ_{stat}
	-0.142	0.105	5.406	1.267	-0.520	6.491	result
$\kappa_2[net]/(\kappa_1[h^+] + \kappa_1[h^-])$	0.018	0.011	0.007	0.004	0.007	0.019	σ_{syst}
	0.007	0.007	0.005	0.004	0.004	0.006	σ_{stat}
	0.691	0.660	0.633	0.619	0.531	0.422	result
$\kappa_3[net]/\kappa_1[net]$	0.110	0.245	0.152	0.360	0.263	0.595	σ_{syst}
	0.240	0.280	0.317	0.339	0.508	1.172	σ_{stat}
	0.380	0.487	1.174	0.167	-0.174	1.233	result

Table 5.1: Corrected numerical values of κ_2/κ_1, κ_3/κ_2, κ_4/κ_2 for positively and negatively charged particles and net-charge as well as $\kappa_2[net]/(\kappa_1[h^+] + \kappa_1[h^-])$, $\kappa_3[net]/\kappa_1[net]$, with their systematic and statistical uncertainties, in ^{40}Ar+^{45}Sc interactions at 13A, 19A, 30A, 40A, 75A, 150A GeV/c.

5.4 Comparison with *p+p* and Be+Be collisions

The higher-order moments of positively and negatively charged particle multiplicity and net-charge in *p+p* and ^{7}Be+^{9}Be have been studied by the NA61/SHINE experiment [87]. The *p+p* results have the status "final" and they are soon to be published [82]. The ^{7}Be+^{9}Be results are released with the status of preliminary and cover only net-charge quantities (status for 30.03.2023). The energy dependence of the κ_2/κ_1, κ_3/κ_2, κ_4/κ_2 ratios of multiplicity distributions and net-charge, and $\kappa_2/(\kappa_1^+ + \kappa_1^-)$, κ_3/κ_1 of net-charge in *p+p*, ^{7}Be+^{9}Be and ^{40}Ar+^{45}Sc is shown in Fig. 5.5 (positively charged hadrons), Fig. 5.6 (negatively charged hadrons), and Fig.5.7 (net-charge). The κ_2/κ_1 in the case of both positively and negatively charged particle multiplicity, increases monotonically in *p+p* interactions but stays on the approximately same level in ^{40}Ar+^{45}Sc. Moreover, the signal of κ_2/κ_1 in *p+p* is enhanced (above 1 for higher collision energies) whereas in ^{40}Ar+^{45}Sc it is suppressed (below 1). The κ_3/κ_2 of positively and negatively charged particle multiplicity in ^{40}Ar+^{45}Sc interactions, similarly to the quantities measured in *p+p* collisions, increases with collision energy but stays in the vicinity of the reference value. A small, systematic shift toward lower values is seen in ^{40}Ar+^{45}Sc compared to *p+p* in case of positively charged particles. The κ_4/κ_2 behavior in ^{40}Ar+^{45}Sc is different comparing to *p+p*. In ^{40}Ar+^{45}Sc in positively charged particles, the κ_4/κ_2 decreases with energy, and in negatively charged particles, it indicates a non-monotonic behavior. In *p+p* interactions, the slight monotonic increase of κ_4/κ_2 is observed in both charges. However, large uncertainties in ^{40}Ar+^{45}Sc make the estimation of the real differences difficult.

The κ_2/κ_1 of net-charge in ^{40}Ar+^{45}Sc shows a very good agreement with ^{7}Be+^{9}Be and increase faster than in *p+p*. The $\kappa_2/(\kappa_1^+ + \kappa_1^-)$ of all three systems: *p+p*, ^{7}Be+^{9}Be and ^{40}Ar+^{45}Sc agree within the systematic uncertainties. The indication of a non-monotonic behavior of κ_3/κ_2, κ_4/κ_2 and κ_3/κ_1 is observed only in ^{40}Ar+^{45}Sc. Nevertheless, the scale of the fluctuations is small since, for many collision energies, the difference between ^{40}Ar+^{45}Sc quantities and *p+p* and/or ^{7}Be+^{9}Be is smaller than their statistical or systematic uncertainties. Statistical uncertainties of fluctuation measures, which hinder the comparison between systems, are expected to enlarge with the size of the system. It is caused by the uncertainties of κ_3 and κ_4 which increase with the system size [88].

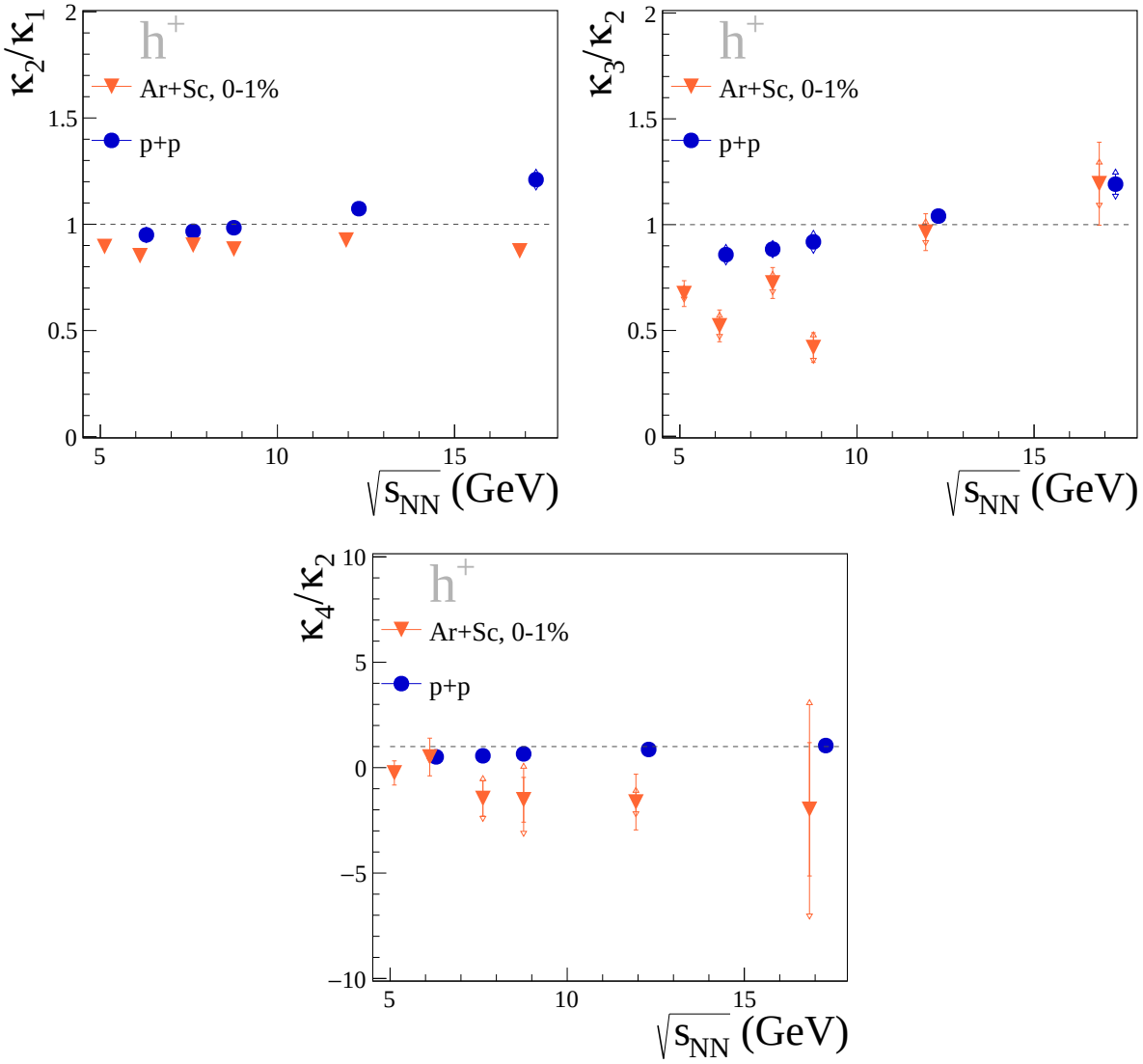

Figure 5.5: Energy dependence of κ_2/κ_1 (top, left), κ_3/κ_2 (top, right) and κ_4/κ_2 (bottom) of positively charged hadron multiplicity distributions in ^{40}Ar+^{45}Sc interactions in *p+p* [82] and ^{40}Ar+^{45}Sc interactions. The flat-ended error bars correspond to statistical uncertainties and the arrow-ended error bars – systematic uncertainties. The line at unity corresponds to the reference value of the Poisson distribution.

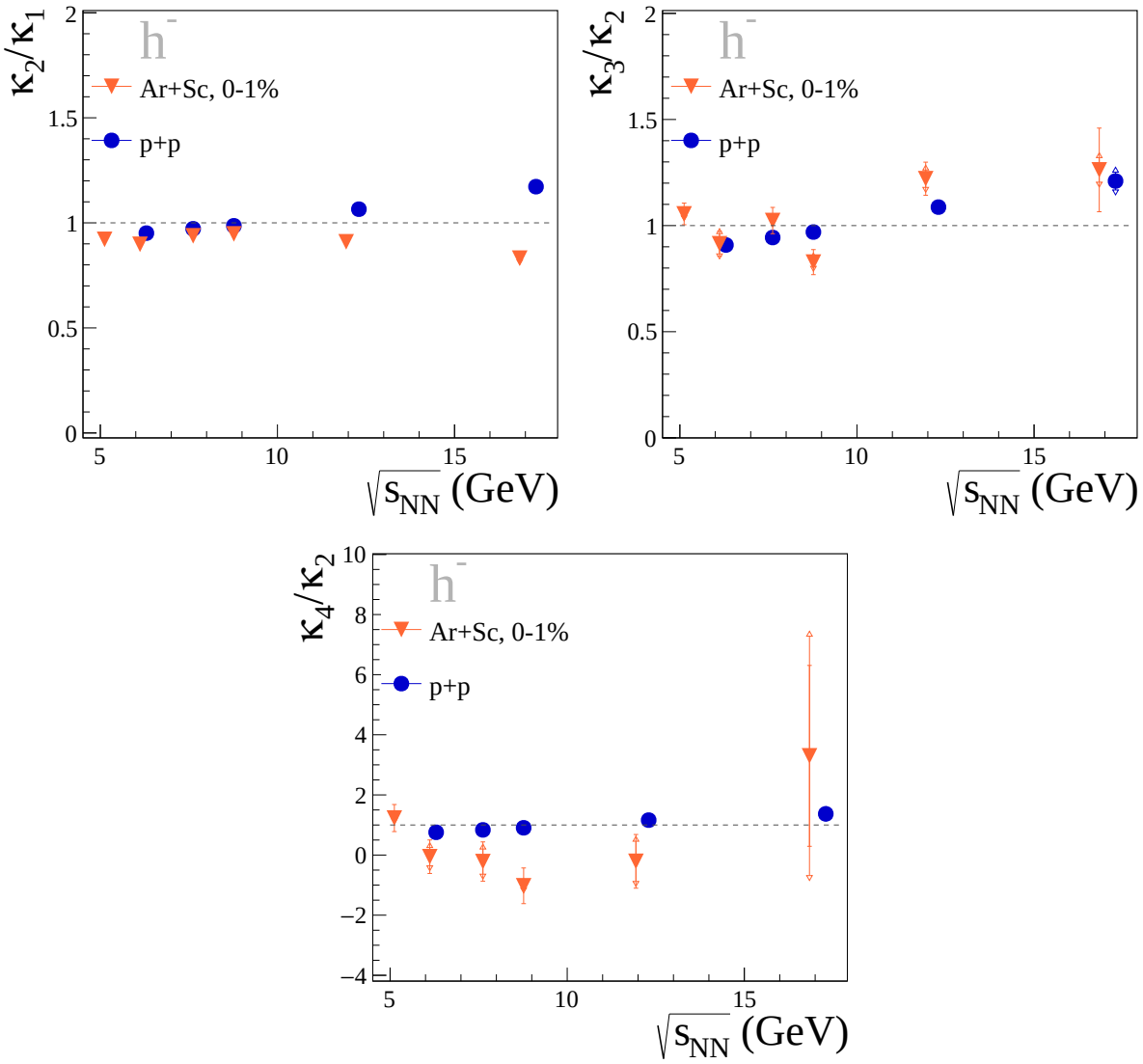

Figure 5.6: Energy dependence of κ_2/κ_1 (top, left), κ_3/κ_2 (top, right) and κ_4/κ_2 (bottom) of negatively charged hadron multiplicity distributions in *p+p* [82] and ^{40}Ar+^{45}Sc interactions. The flat-ended error bars correspond to statistical uncertainties and the arrow-ended error bars – systematic uncertainties. The line at unity corresponds to the reference value of the Poisson distribution.

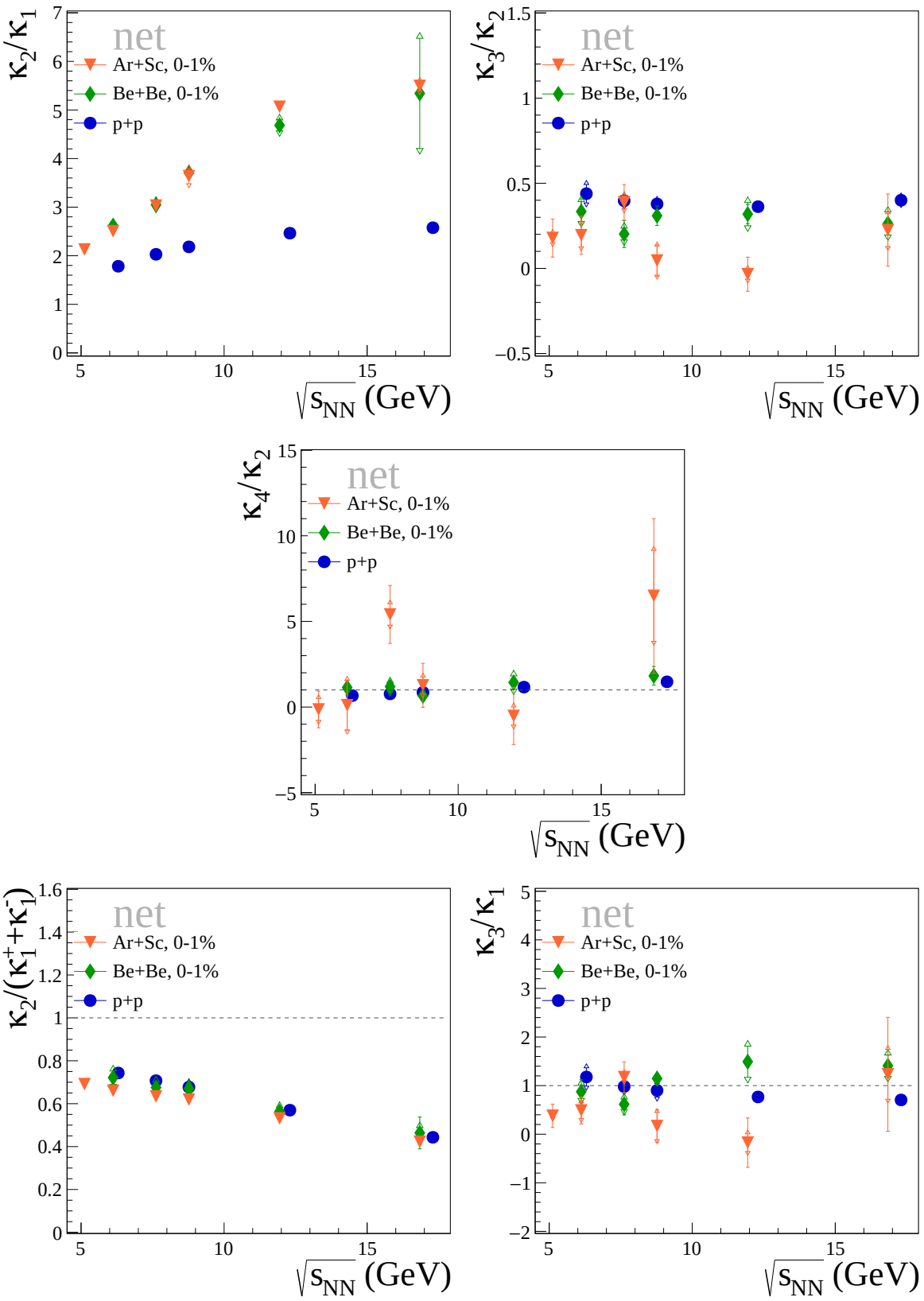

Figure 5.7: Energy dependence of κ_2/κ_1 (top, left), κ_3/κ_2 (top, right) and κ_4/κ_2 (middle) of net-charge distributions in *p+p*, ^{7}Be+^{9}Be and ^{40}Ar+^{45}Sc interactions, as well as energy dependence of $\kappa_2/(\kappa_1^+ + \kappa_1^-)$ (bottom, left) and κ_3/κ_1 (bottom, right) of net-charge distribution in *p+p* [82], ^{7}Be+^{9}Be and ^{40}Ar+^{45}Sc interactions. The flat-ended error bars correspond to statistical uncertainties and the arrow-ended error bars – systematic uncertainties. The line at unity corresponds to the reference value of the Skellam distribution.

Chapter 6

Summary

The aim of this study was the search for the critical behavior by studying the fluctuations of positively and negatively charged hadrons as well as net-charge in the 1% most central ^{40}Ar+^{45}Sc interactions at beam momenta 13*A*, 19*A*, 30*A*, 40*A*, 75*A*, and 150*A* GeV/*c*. The experimental data, recorded in 2015, were successfully analyzed and both statistical and systematic uncertainties were estimated. For the first time in NA61/SHINE, the *Unfolding* was used to correct the data for detector effects in *A*+*A* collisions including centrality selection bias.

The obtained ratios of higher-order cumulants show clear energy dependencies and the independent particle production does not describe the data correctly. In most cases, both multiplicity and net-charge distributions are narrower than corresponding Poisson or Skellam distributions.

The EPOS1.99 model was used for the comparison as, in many cases, it describes NA61/SHINE results well. Generally, the ratios of higher-order cumulants of negatively charged particle multiplicity are described by EPOS more precisely than of positively charged particle multiplicity. In many cases, EPOS seems to describe the data qualitatively well, but significant statistical and/or systematic uncertainties hinder the accurate interpretation.

Signs of non-monotonic behavior, which may be a signal of critical point, have been observed in κ_4/κ_2 of negatively charged particle multiplicity as well as κ_3/κ_2, κ_4/κ_2 and κ_3/κ_1 of net-charge distribution. Nevertheless, the uncertainties of those quantities are large, so the actual size of this effect may be, in fact, smaller.

Comparison of the results with corresponding ones in *p*+*p* and ^{7}Be+^{9}Be does not show any big discrepancies between the systems, except the effects mentioned in the previous paragraph, which is not observed in *p*+*p* or ^{7}Be+^{9}Be interactions.

The work on publishing the *p*+*p* and finalizing the ^{7}Be+^{9}Be analyses is in progress and the next datasets measured by NA61/SHINE: ^{129}Xe+^{139}La and ^{208}Pb+^{207}Pb, are currently under reconstruction and calibration. Together they will create a first-of-a-kind detailed scan of the QCD phase diagram. It would be worth studying these dependencies with improved data statistics which will be possible with the upgraded NA61/SHINE detectors.

Remarks on my contribution to the NA61/SHINE work

I started my doctoral studies in 2018 at the Department of Nuclear Physics, Faculty of Physics, Warsaw University of Technology. During this time, I was a member of the NA61/SHINE experiment group, where, in addition to research related to the presented doctoral thesis, I also performed service work for the experiment. This included participating in shifts during data collection, working on Monte Carlo simulation software, and being responsible for producing Monte Carlo simulated data used by the experiment members. I am also the author of the C++ library used by the NA61/SHINE experiment members for data selection from Ar+Sc collisions.

During my doctoral studies, I participated in several international scientific conferences, where I presented both my results and the results of other experiment members, i.e., 19th Zimanyi School Winter Workshop on Heavy Ion Physics (December 2-6, 2019), 50th International Symposium on Multiparticle Dynamics (ISMD2021, July 12-16, 2021), and 41st International Conference on High Energy Physics (ICHEP2022, July 6-13, 2022). In addition to that, I attended NA61/SHINE experiment meetings held 2 or 3 times a year, where I presented the current status of my research work and the work of the group involved in Monte Carlo simulation production for the experiment. I actively participated in weekly meetings of several working groups within the experiment.

The results presented in this thesis have been classified by the collaboration members as "preliminary" in 2022 and since then, they have been presented at several international scientific conferences:

- 41st International Conference on High Energy Physics (ICHEP2022, July 6-13, 2022),
- 14th workshop on Critical Point and Onset of Deconfinement (CPOD 2022, November 28 - December 2, 2022),
- 8th International Conference on Physics and Astrophysics of Quark Gluon Plasma (ICPAQGP-2023, February 7-10, 2023).

In 2023 the presented results obtained the status "final". A scientific publication containing the analysis results is currently in the final stage of editing.

Appendix A

Probability Distributions

A.1 Poisson distribution

The Poisson distribution is a discrete probability distribution used to model the probability of a certain number of events occurring in a fixed interval of time or space, assuming that the events are independent from each other. The Poisson distribution is characterized by a single parameter λ, which represents the average number of events that occur in a given interval and also is the variance of the distribution.

The probability mass function (the probability that a discrete random variable X is equal to some exact value) of the Poisson distribution is given by Eq. (A.1):

$$P(X = k; \lambda) = \frac{\lambda^k}{k!} \cdot e^{-\lambda} , \tag{A.1}$$

where:

- k – the number of occurrences of the event,
- λ – the expected number of events in a given time or space interval.

The example of Poisson distributions is presented in Fig. A.1. Poisson distribution is useful

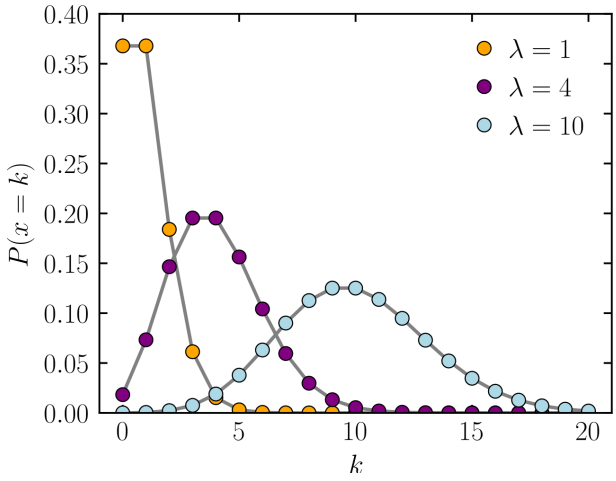

Figure A.1: Poisson probability mass function for different values of parameter λ [89].

in describing many physics phenomena, including radioactive decays or particle production in heavy-ion collisions according to the independent particle production model. In the last case, which is relevant to this thesis, the "fixed interval of time or space" mentioned in the definition of the distribution, is a single collision of the system with fixed size and energy. Then, λ denotes

the mean particle production taking into account a set of such collisions and k is the particle production in a single collision.

A.2 Gaussian distribution

The Gaussian distribution (also called Normal distribution) is a continuous probability distribution of a random variable which is a real number. The probability density function (the likelihood that a value occurs within a given range of the random variable) of the Gaussian distribution is given by Eq. (A.2):

$$\varphi(x;\mu,\sigma) = \frac{1}{\sqrt{2\pi}\sigma} e^{\frac{-(x-\mu)^2}{2\sigma^2}} , \tag{A.2}$$

where:

- μ – the mean value of the distribution,
- σ – the standard deviation of the distribution.

The examples of Gaussian distributions are presented in Fig. A.2.

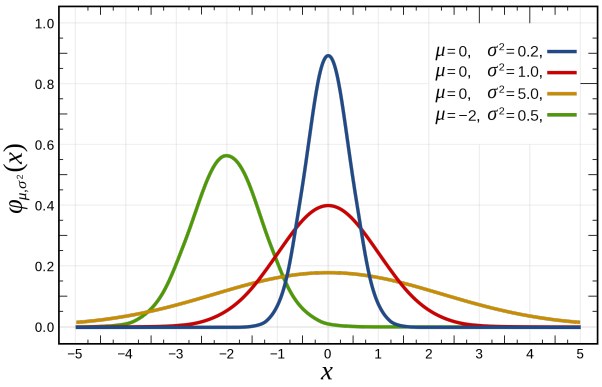

Figure A.2: Gaussian probability density function for different values of parameters μ and σ [90].

A.3 Skellam distribution

The Skellam distribution is a probability distribution that models the difference between two independent, Poisson-distributed random variables. Specifically, if X and Y are independent, Poisson-distributed random variables with parameters μ_1 and μ_2, respectively, then the difference $Z = X - Y$ follows a Skellam distribution. The probability mass function of the Skellam distribution is given by Eq. (A.3):

$$P(k;\mu_1,\mu_2) = e^{-(\mu_1+\mu_2)} \left(\frac{\mu_1}{\mu_2}\right)^{k/2} I_k(2\sqrt{\mu_1\mu_2}) , \tag{A.3}$$

where:

- k – the number of occurrences of the event,
- μ_1 and μ_2 – the expected values of the 1st and 2nd random variable,

- I_k – the modified Bessel function of the first kind (for more details see Ref. [91]).

The example of Skellam distributions is presented in Fig. A.3.

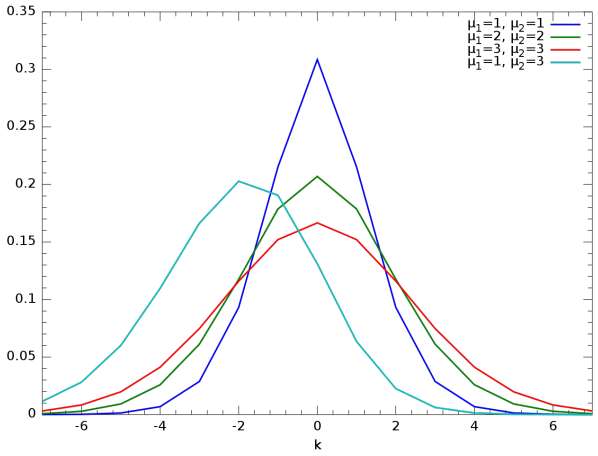

Figure A.3: Skellam probability mass function for different values of parameters μ_1 and μ_2 [92].

A.4 Moment and cumulant generating function

Moments and cumulants of a certain probability distribution are derived from its moment/cumulant generating function. General formulas of those functions are presented in Eqs. (A.4) and (A.5).

Moment generating function of the random variable X:

$$\mathrm{MGF}_X(t) = \mathrm{E}[e^{Xt}] \,, \tag{A.4}$$

where E denotes the expected value of e^{Xt} and t is a real number for which the MGF exists and it is finite for any closed interval $-h < t < h$, with $h > 0$. Cumulant generating function of the random variable X:

$$\mathrm{CGF}_X(t) = \ln(\mathrm{E}[e^{Xt}]) = \ln(\mathrm{MGF}_X(t)) \,. \tag{A.5}$$

An n-th moment or cumulant of a random variable X is calculated as an n-th derivative with respect to t of MGF or CGF respectively, evaluated at $t = 0$. Direct formulas of MGF of the most common probability distributions, including Poisson, Gaussian and Skellam distributions, are known and they are presented in Tab. A.1.

distribution	MGF
Poisson	$e^{\lambda(e^t-1)}$
Gaussian	$e^{t\mu+\frac{1}{2}\sigma^2t^2}$
Skellam	$e^{-(\mu_1+\mu_2)+\mu_1e^t+\mu_2e^{-t}}$

Table A.1: Moment Generating Functions (MGF) of Poisson, Gaussian and Skellam distributions.

Bibliography

[1] R. L. Workman *et al.* [Particle Data Group], "*Review of Particle Physics*", *PTEP*, vol. 2022, p. 083C01, 2022.

[2] R. Aaij *et al.* [LHCb], "*Observation of structure in the* J/ψ *-pair mass spectrum*", *Sci. Bull.*, vol. 65, no. 23, pp. 1983–1993, 2020. arXiv:2006.16957 [hep-ex].

[3] R. Aaij *et al.* [LHCb], "*Observation of* $J/\psi p$ *Resonances Consistent with Pentaquark States in* $\Lambda_b^0 \to J/\psi K^- p$ *Decays*", *Phys. Rev. Lett.*, vol. 115, p. 072001, 2015. arXiv:1507.03414 [hep-ex].

[4] H.-X. Chen, W. Chen, X. Liu, Y.-R. Liu, and S.-L. Zhu, "*An updated review of the new hadron states*", *Rept. Prog. Phys.*, vol. 86, no. 2, p. 026201, 2023. arXiv:2204.02649 [hep-ph].

[5] "Standard model of elementary particles". `https://en.wikipedia.org/wiki/File:Standard_Model_of_Elementary_Particles.svg`, Accessed: 2022, October 10.

[6] D. H. Perkins, "*Introduction to high energy physics*". CAMBRIDGE university press, 2000.

[7] R. Stock, "*The QCD Phase Diagram: Expectations and Challenges*", *PoS*, vol. CPOD2009, p. 001, 2009. arXiv:0909.0601 [nucl-ex].

[8] P. Braun-Munzinger, V. Koch, T. Schäfer, and J. Stachel, "*Properties of hot and dense matter from relativistic heavy ion collisions*", *Phys. Rept.*, vol. 621, pp. 76–126, 2016. arXiv:1510.00442 [nucl-th].

[9] A. Bazavov *et al.* [HotQCD], "*Chiral crossover in QCD at zero and non-zero chemical potentials*", *Phys. Lett. B*, vol. 795, pp. 15–21, 2019. arXiv:1812.08235 [hep-lat].

[10] S. Borsanyi, Z. Fodor, J. N. Guenther, R. Kara, S. D. Katz, P. Parotto, A. Pasztor, C. Ratti, and K. K. Szabo, "*QCD Crossover at Finite Chemical Potential from Lattice Simulations*", *Phys. Rev. Lett.*, vol. 125, no. 5, p. 052001, 2020. arXiv:2002.02821 [hep-lat].

[11] C. R. Allton, S. Ejiri, S. J. Hands, O. Kaczmarek, F. Karsch, E. Laermann, C. Schmidt, and L. Scorzato, "*The QCD thermal phase transition in the presence of a small chemical potential*", *Phys. Rev. D*, vol. 66, p. 074507, 2002. arXiv:hep-lat/0204010.

[12] M. D'Elia and M.-P. Lombardo, "*Finite density QCD via imaginary chemical potential*", *Phys. Rev. D*, vol. 67, p. 014505, 2003. arXiv:hep-lat/0209146.

[13] C. S. Fischer, J. Luecker, and C. A. Welzbacher, "*Phase structure of three and four flavor QCD*", *Phys. Rev. D*, vol. 90, no. 3, p. 034022, 2014. arXiv:1405.4762 [hep-ph].

[14] N. G. Antoniou and A. S. Kapoyannis, "*Bootstraping the QCD critical point*", *Phys. Lett. B*, vol. 563, pp. 165–172, 2003. arXiv:hep-ph/0211392.

[15] M. Kuich [NA61/SHINE], "*Strangeness production and onset of deconfinement study in NA61/SHINE*", *PoS*, vol. CPOD2021, p. 018, 2022.

[16] O. Philipsen, "*Exploring the QCD phase diagram*", *PoS*, vol. CPOD07, p. 028, 2007. arXiv:0710.1217 [hep-ph].

[17] H.-T. Ding, "*New developments in lattice QCD on equilibrium physics and phase diagram*", *Nucl. Phys. A*, vol. 1005, p. 121940, 2021. arXiv:2002.11957 [hep-lat].

[18] J. C. Collins and M. J. Perry, "*Superdense Matter: Neutrons Or Asymptotically Free Quarks?*", *Phys. Rev. Lett.*, vol. 34, p. 1353, 1975.

[19] E. Witten, "*Cosmic Separation of Phases*", *Phys. Rev. D*, vol. 30, pp. 272–285, 1984.

[20] J. Rafelski and J. Birrell, "*Traveling Through the Universe: Back in Time to the Quark-Gluon Plasma Era*", *J. Phys. Conf. Ser.*, vol. 509, p. 012014, 2014. arXiv:1311.0075 [nucl-th].

[21] R. Sahoo, "*Possible Formation of QGP-droplets in Proton-Proton Collisions at the CERN Large Hadron Collider*", *AAPPS Bull.*, vol. 29, no. 4, pp. 16–21, 2019. arXiv:1908.10566 [nucl-ex].

[22] J. D. Bjorken, "*Highly Relativistic Nucleus-Nucleus Collisions: The Central Rapidity Region*", *Phys. Rev. D*, vol. 27, pp. 140–151, 1983.

[23] R. Singh, L. Kumar, P. K. Netrakanti, and B. Mohanty, "*Selected Experimental Results from Heavy Ion Collisions at LHC*", *Adv. High Energy Phys.*, vol. 2013, p. 761474, 2013. arXiv:1304.2969 [nucl-ex].

[24] M. Gazdzicki, M. Gorenstein, and P. Seyboth, "*Brief history of the search for critical structures in heavy-ion collisions*", *Acta Phys. Polon. B*, vol. 51, p. 1033, 2020. arXiv:2004.02255 [hep-ph].

[25] J. Cleymans, H. Oeschler, K. Redlich, and S. Wheaton, "*Strangeness Excitation Functions and Transition from Baryonic to Mesonic Freeze-Out*", *Acta Phys. Polon. Supp.*, vol. 3, pp. 533–538, 2010. arXiv:0911.0526 [hep-ph].

[26] S. Acharya *et al.* [ALICE], "*Production of charged pions, kaons, and (anti-)protons in Pb-Pb and inelastic* pp *collisions at* $\sqrt{s_{NN}} = 5.02$ *TeV*", *Phys. Rev. C*, vol. 101, no. 4, p. 044907, 2020. arXiv:1910.07678 [nucl-ex].

[27] E. Schnedermann, J. Sollfrank, and U. W. Heinz, "*Thermal phenomenology of hadrons from 200-A/GeV S+S collisions*", *Phys. Rev. C*, vol. 48, pp. 2462–2475, 1993. arXiv:nucl-th/9307020.

[28] A. Andronic and P. Braun-Munzinger, "*Ultrarelativistic nucleus-nucleus collisions and the quark gluon plasma*", *Lect. Notes Phys.*, vol. 652, pp. 35–67, 2004. arXiv:hep-ph/0402291.

[29] F. Becattini, M. Gazdzicki, and J. Sollfrank, "*On chemical equilibrium in nuclear collisions*", *Eur. Phys. J. C*, vol. 5, pp. 143–153, 1998. arXiv:hep-ph/9710529.

[30] M. Mitrovski [NA49], "*Recent results on strangeness production from NA49*", *J. Phys. G*, vol. 37, p. 094003, 2010. arXiv:1001.1699 [nucl-ex].

[31] C. Blume, "*Open questions in the understanding of strangeness production in hic–experiment perspective*", in *EPJ Web of Conferences*, vol. 171, p. 03001, EDP Sciences, 2018.

[32] B. B. Abelev *et al.* [ALICE], "*Multi-strange baryon production at mid-rapidity in Pb-Pb collisions at* $\sqrt{s_{NN}} = 2.76$ *TeV*", *Phys. Lett. B*, vol. 728, pp. 216–227, 2014. arXiv:1307.5543 [nucl-ex].

[33] M. Gazdzicki, M. Gorenstein, and P. Seyboth, "*Onset of deconfinement in nucleus-nucleus collisions: Review for pedestrians and experts*", *Acta Phys. Polon. B*, vol. 42, pp. 307–351, 2011. arXiv:1006.1765 [hep-ph].

[34] M. C. Abreu *et al.* [NA50], "*Evidence for deconfinement of quarks and gluons from the J/*ψ *suppression pattern measured in Pb+Pb collisions at the CERN SPS*", *Phys. Lett. B*, vol. 477, pp. 28–36, 2000.

[35] D. G. d'Enterria, "*Quark-Gluon Matter*", *J. Phys. G*, vol. 34, pp. S53–S82, 2007. arXiv:nucl-ex/0611012.

[36] U. A. Acharya *et al.* [PHENIX], "*Nonprompt direct-photon production in Au+Au collisions at* $\sqrt{s_{NN}} =$ 200 *GeV*", arXiv:2203.17187 [nucl-ex].

[37] A. Marin *et al.* [CERES], "*Dilepton measurements with CERES*", *PoS*, vol. CPOD07, p. 034, 2007. arXiv:0802.2679 [nucl-ex].

[38] S. Damjanovic [NA60], "*Thermal dileptons at SPS energies*", *J. Phys. G*, vol. 35, p. 104036, 2008. arXiv:0805.4153 [nucl-ex].

[39] J. Adam *et al.* [STAR], "*Measurements of dielectron production in au + au collisions at* $\sqrt{s_{NN}} =$ 27, 39, and62.4 *gev from the star experiment*", *arXiv preprint*, 2018. arXiv:1810.10159 [nucl-ex].

[40] L. Adamczyk *et al.* [STAR], "*Energy dependence of acceptance-corrected dielectron excess mass spectrum at mid-rapidity in au+au collisions at snn=19.6 and 200 gev*", *Physics Letters B*, vol. 750, pp. 64–71, 2015. arXiv:1501.05341 [hep-ex].

[41] L. Kumar, "*Review of Recent Results from the RHIC Beam Energy Scan*", *Mod. Phys. Lett. A*, vol. 28, p. 1330033, 2013. arXiv:1311.3426 [nucl-ex].

[42] S. Chatrchyan *et al.* [CMS], "*Study of high-*p_T *charged particle suppression in PbPb compared to pp collisions at* $\sqrt{s_{NN}} = 2.76$ *TeV*", *Eur. Phys. J. C*, vol. 72, p. 1945, 2012. arXiv:1202.2554 [nucl-ex].

[43] M. Gazdzicki and M. I. Gorenstein, "*On the early stage of nucleus-nucleus collisions*", *Acta Phys. Polon.*, vol. B30, p. 2705, 1999. arXiv:hep-ph/9803462 [hep-ph].

[44] E. Andronov, M. Kuich, and M. Gaździcki, "*Diagram of High-Energy Nuclear Collisions †*", *Universe*, vol. 9, no. 2, p. 106, 2023. arXiv:2205.06726 [hep-ph].

[45] A. Acharya *et al.* [NA61/SHINE], "*Spectra and mean multiplicities of π^- in central ^{40}Ar+^{45}Sc collisions at 13A, 19A, 30A, 40A, 75A and 150A GeV/c beam momenta measured by the NA61/SHINE spectrometer at the CERN SPS*", *Eur. Phys. J. C*, vol. 81, no. 5, p. 397, 2021. arXiv:2101.08494 [hep-ex].

[46] W. Brylinski [NA61/SHINE], "*Strangeness production in NA61/SHINE*", *WWND 2023 conference,* `https://indico.cern.ch/event/1196342/`.

[47] M. Kuich [NA61/SHINE], "*Recent results on the study of the onset of deconfinement and search for critical point from NA61/SHINE experiment*", *WHBM 2023 conference,* `https://conference-indico.kek.jp/event/205/`.

[48] M. Asakawa and M. Kitazawa, "*Fluctuations of conserved charges in relativistic heavy ion collisions: An introduction*", *Prog. Part. Nucl. Phys.*, vol. 90, pp. 299–342, 2016. arXiv:1512.05038 [nucl-th].

[49] A. Bialas, M. Bleszynski, and W. Czyz, "*Multiplicity Distributions in Nucleus-Nucleus Collisions at High-Energies*", *Nucl. Phys.*, vol. B111, p. 461, 1976.

[50] V. Begun, "*Participant number fluctuations for higher moments of a multiplicity distribution*", arXiv:1606.05358 [nucl-th].

[51] V. V. Begun, M. Gazdzicki, M. I. Gorenstein, and O. S. Zozulya, "*Particle number fluctuations in canonical ensemble*", *Phys. Rev.*, vol. C70, p. 034901, 2004. arXiv:nucl-th/0404056 [nucl-th].

[52] M. A. Stephanov, K. Rajagopal, and E. V. Shuryak, "*Event-by-event fluctuations in heavy ion collisions and the QCD critical point*", *Phys. Rev.*, vol. D60, p. 114028, 1999. arXiv:hep-ph/9903292 [hep-ph].

[53] C. Athanasiou, K. Rajagopal, and M. Stephanov, "*Using Higher Moments of Fluctuations and their Ratios in the Search for the QCD critical point*", *Phys. Rev.*, vol. D82, p. 074008, 2010. arXiv:1006.4636 [hep-ph].

[54] NA61/SHINE library of images.

[55] V. Vovchenko, D. V. Anchishkin, M. I. Gorenstein, and R. V. Poberezhnyuk, "*Scaled variance, skewness, and kurtosis near the critical point of nuclear matter*", *Phys. Rev. C*, vol. 92, no. 5, p. 054901, 2015. arXiv:1506.05763 [nucl-th].

[56] K. Redlich, "*A non-critical baseline for fluctuation measurements*". CPOD 2021, https://indico.cern.ch/event/985460/contributions/4264590/, Accessed: 2023, May 30.

[57] C. Alt *et al.* [NA49], "*Energy Dependence of Multiplicity Fluctuations in Heavy Ion Collisions at the CERN SPS*", *Phys. Rev.*, vol. C78, p. 034914, 2008. arXiv:0712.3216 [nucl-ex].

[58] C. Alt *et al.* [NA49], "*Centrality and system size dependence of multiplicity fluctuations in nuclear collisions at 158A GeV/c*", *Phys. Rev. C*, vol. 75, p. 064904, 2007. arXiv:nucl-ex/0612010.

[59] B. Lungwitz, *"Energy dependence of multiplicity fluctuations in heavy ion collisions at the CERN SPS"*. PhD thesis, Frankfurt, Frankfurt University, FIAS, 2008, CERN-THESIS-2008-108, http://cds.cern.ch/record/1287912.

[60] J. Thader [STAR], "*Higher Moments of Net-Particle Multiplicity Distributions*", *Nucl. Phys.*, vol. A956, pp. 320–323, 2016. arXiv:1601.00951 [nucl-ex].

[61] L. Adamczyk *et al.* [STAR], "*Beam energy dependence of moments of the net-charge multiplicity distributions in Au+Au collisions at RHIC*", *Phys. Rev. Lett.*, vol. 113, p. 092301, 2014. arXiv:1402.1558 [nucl-ex].

[62] J. T. Mitchell [PHENIX], "*The RHIC Beam Energy Scan Program: Results from the PHENIX Experiment*", *Nucl. Phys. A*, vol. 904-905, pp. 903c–906c, 2013. arXiv:1211.6139 [nucl-ex].

[63] A. Adare *et al.* [PHENIX], "*Measurement of higher cumulants of net-charge multiplicity distributions in Au+Au collisions at* $\sqrt{s_{NN}} = 7.7 - 200$ *GeV*", *Phys. Rev.*, vol. C93, no. 1, p. 011901, 2016. arXiv:1506.07834 [nucl-ex].

[64] K. Grebieszkow [NA49], "*Search for the critical point of strongly interacting matter in NA49*", *Nucl. Phys.*, vol. A830, pp. 547C–550C, 2009. arXiv:0907.4101 [nucl-ex].

[65] N. Abgrall *et al.* [NA61/SHINE], "*NA61/SHINE facility at the CERN SPS: beams and detector system*", *J. Inst.*, vol. 9, p. P06005, 2014. arXiv:1401.4699 [physics.ins-det].

[66] M. Gazdzicki, Z. Fodor, and G. Vesztergombi [NA49-future], "*Study of Hadron Production in Hadron-Nucleus and Nucleus-Nucleus Collisions at the CERN SPS*", 2006, CERN-SPSC-2006-034, SPSC-P-330, https://cds.cern.ch/record/995681.

[67] Y. Nagai, "*Addendum to the NA61/SHINE Proposal: A Low-Energy Beamline at the SPS H2*", 2021, CERN-SPSC-2021-028, SPSC-P-330-ADD-12, https://cds.cern.ch/record/2783037.

[68] N. Amin [NA61/SHINE], "*Results from a Pilot Study on the Measurement of Nuclear Fragmentation with NA61/SHINE at the CERN SPS:* ^{11}C *Production in C+p Interactions at 13.5A GeV/c*", *PoS*, vol. ICRC2021, p. 102, 2021. arXiv:2107.12275 [nucl-ex].

[69] N. Charitonidis, "*NA61 current and future beams and operation in H2 beam line*". NA61/SHINE Collaboration Meeting, 2018.

[70] D. Banas, A. Kubala-Kukus, M. Rybczynski, I. Stabrawa, and G. Stefanek, "*Influence of target material impurities on physical results in relativistic heavy-ion collisions*", *Eur. Phys. J. Plus*, vol. 134, no. 1, p. 44, 2019. arXiv:1808.10377 [nucl-ex].

[71] E. Andronov and A. Seryakov, "Ar+Sc: centrality selection". NA61/SHINE Collaboration Meeting, 2016.

[72] K. Werner, "*The hadronic interaction model EPOS*", *Nucl. Phys. Proc. Suppl.*, vol. 175-176, pp. 81–87, 2008.

[73] R. Ulrich, T. Pierog, and C. Baus, "The Cosmic Ray Monte Carlo Package, CRMC (v1.6.0)".

[74] A. Aduszkiewicz, *"Energy dependence of negatively charged pion production in proton-proton interactions at the CERN SPS"*. PhD thesis, University of Warsaw, 2016, CERN-THESIS-2016-010, http://cds.cern.ch/record/2135329.

[75] M. Dobbs and J. B. Hansen, "*The HepMC C++ Monte Carlo event record for High Energy Physics*", *Comput. Phys. Commun.*, vol. 134, pp. 41–46, 2001.

[76] S. Agostinelli *et al.* [GEANT4], "*GEANT4 – a simulation toolkit*", *Nucl. Instrum. Meth. A*, vol. 506, pp. 250–303, 2003.

[77] J. Cybowska, "Detector acceptance maps for track selection". `https://edms.cern.ch/document/2487456/1`, 2020, CERN EDMS.

[78] A. Seryakov, "PSD acceptance maps for event selection". `https://edms.cern.ch/document/1867336/1`, 2017, CERN EDMS.

[79] L. Brenner, R. Balasubramanian, C. Burgard, W. Verkerke, G. Cowan, P. Verschuuren, and V. Croft, "*Comparison of unfolding methods using RooFitUnfold*", *Int. J. Mod. Phys. A*, vol. 35, no. 24, p. 2050145, 2020. arXiv:1910.14654 [physics.data-an].

[80] A. Aduszkiewicz *et al.* [NA61/SHINE], "*Two-particle correlations in azimuthal angle and pseudorapidity in central* ^{7}*Be* + ^{9}*Be collisions at the CERN Super Proton Synchrotron*", *Eur. Phys. J. C*, vol. 80, no. 12, p. 1151, 2020. arXiv:2006.02153 [nucl-ex].

[81] G. D'Agostini, "*A Multidimensional unfolding method based on Bayes' theorem*", *Nucl. Instrum. Meth.*, vol. A 362, pp. 487–498, 1995.

[82] A. Acharya *et al.* [NA61/SHINE], "*Measurements of higher-order moments of multiplicity and net-electric charge distributions in inelastic proton-proton interactions at the CERN Super Proton Synchrotron*", To be published soon.

[83] B. Efron, "*Computers and the theory of statistics: thinking the unthinkable*", *SIAM review*, vol. 21, no. 4, pp. 460–480, 1979.

[84] D. Moore, G. McCabe, W. Duckworth, and L. Alwan, "*The practice of business statistics*", 2008, WH Freeman, New York.

[85] K. Werner, L. Karpenko, M. Bleicher, and T. Pierog, "*The Physics of EPOS*", *EPJ Web Conf.*, vol. 52, p. 05001, 2013.

[86] A. Acharya *et al.* [NA61/SHINE], "*Measurements of multiplicity fluctuations of identified hadrons in inelastic proton–proton interactions at the CERN Super Proton Synchrotron*", *Eur. Phys. J. C*, vol. 81, no. 5, p. 384, 2021. arXiv:2009.01943 [nucl-ex].

[87] J. Cybowska, "Searching for the critical point: news from fluctuations study in the NA61/SHINE experiment". ICHEP 2022, https://agenda.infn.it/event/28874/contributions/168972/, Accessed: 2023, May 30.

[88] X. Luo, "*Error Estimation for Moments Analysis in Heavy Ion Collision Experiment*", *J. Phys. G*, vol. 39, p. 025008, 2012. arXiv:1109.0593 [physics.data-an].

[89] "Poisson distribution". In Wikipedia. https://en.wikipedia.org/wiki/Poisson_distribution, Accessed: 2023, March 23.

[90] "Normal distribution". In Wikipedia. https://en.wikipedia.org/wiki/Normal_distribution, Accessed: 2023, March 23.

[91] M. Abramowitz, I. A. Stegun, and R. Romer, "Handbook of mathematical functions with formulas, graphs, and mathematical tables". American Association of Physics Teachers, 1988.

[92] "Skellam distribution". In Wikipedia. https://en.wikipedia.org/wiki/Skellam_distribution, Accessed: 2023, March 23.